**Ph. D. Thesis on**

# Analysis of Medical Ultrasound Images for Renal Calculus and Polycystic Kidney Disease

***Submitted to***

**Visvesvaraya Technological University,**
**Belagavi – 590 018**

***For the award of the degree of***

## Doctor of Philosophy


**Submitted by**

**Mrs. Sunanda Biradar**
**USN: 2BL15PEJ02**

**Under the Guidance of**

**Dr. Prema T. Akkasaligar**
Professor


**JULY - 2020**

---


**Department of Computer Science and Engineering**

**BLDEA's V. P. Dr. P. G. Halakatti**

**College of Engineering & Technology,**

**Vijayapur-586 103**

*Dedicated to my beloved parents*

# Late Shri Dundappa C. Biradar

# and

# Late Smt. Shanta D. Biradar

VISVESVARAYA TECHNOLOGICAL UNIVERSITY, BELAGAVI-590018

B.L.D.E.A's V.P Dr. P.G. HALAKATTICOLLEGE OF ENGINEERING & TECHNOLOGY
VIIAYAPURA-586 103

DEPARTMENT OF COMPUTER SCIENCE AND ENGINEERING

# CERTIFICATE

This is to certify that the thesis entitled ***"Analysis of Medical Ultrasound Images for Renal Calculus and Polycystic Kidney Disease'*** submitted by **Sunanda Biradar,** Research Scholar **(USN:2BL15PEJ02)** to Visvesvaraya Technological University, Belagavi, for the award of Doctor of Philosophy degree in Computer Science & Engineering, is an original bonafide research work carried out by her during the period 2014-2020. The results embodied in this thesis have not been submitted fully or in part to any Degree or Diploma of this or any other University or Institute.

**Research Guide**
**(Dr. Prema T. Akkasaligar)**

**Head of the Department**
**(Dr. Pushpa B. Patil)**

**Principal**
**(Dr. Atul B. Ayare)**
Principal,
B.L.D.E.A's. V.P. Dr. P.G.H.
College of Engg. & Tech.
VIJAYAPUR-586103.

# DECLARATION

I hereby declare that the entire work embodied in this doctoral thesis entitled *'**Analysis of Medical Ultrasound Images for Renal Calculus and Polycystic Kidney Disease'*** has been carried out by me at BLDEA's V. P. Dr. P. G. Halakatti College of Engineering and Technology, Vijayapur, under the supervision of Dr. Prema T. Akkasaligar. The work presented in the dissertation does not contain the outcome of any work, previously carried out by others/ submitted by the candidate herself for the award of any degree anywhere.

**Sunanda Biradar (2BL15PEJ02)**
Research Scholar,
Department of Computer Science and Engineering,
BLDEA's V. P. Dr. P. G. Halakatti College of
Engineering and Technology, Vijayapur,
Karnataka, India.

Place: Vijayapur
Date:22-07-2020

# ACKNOWLEDGEMENT

With blessings of God, I am in a position to acknowledge the people who are with me through this journey of research. I am certainly the recipient of the dedication, devotion, insight, and hard work of the people around me. My heartfelt gratitude to all those for what I have received over this period.

First of all, I would like to express my deepest sense of gratitude and thanks to my research supervisor, Dr. (Smt.) Prema T. Akkasaligar, for her exceptional patience, tenderhearted supervision and encouragement all through.

I would like to express my sincere gratitude to the Vice-Chancellor, the Registrar, the Registrar (Evaluation), and all officials of Visvesvaraya Technological University (VTU), Belagavi, for their research related timely decisions, cooperation and encouragement during my research work.

Wholehearted thanks to Dr. P. S. Hiremath, Professor, Department of Computer Applications, KLE Technological University, BVB CET, Hubli, who is the true source of inspiration for the researchers of our generation. I took a lot from his scrupulous knowledge and meticulous experience during my entire research phase.

I sincerely thank Dr. Bhushita B. Lakhkar, Assistant Professor, Department of Radiology, BLDEDU's Shri. B. M. Patil Medical College Hospital and Research Centre, Vijayapur for providing an ultrasound image set of the kidney and Dr. Vinay Kundaragi, Nephrologist, BLDEDU's Shri. B. M. Patil Medical College Hospital and Research Centre, Vijayapur for rendering manual segmentation of images.

I extend my thanks to the management and the authorities of the BLDE Association, for providing me an opportunity to pursue Ph.D.

I sincerely thank my beloved principal, Dr. Atul Ayare, and ex-principal Dr. V.P. Huggi whose multidimensional support and unparalleled cooperation kept me active throughout.

I would like to express my sincere gratitude to my doctoral committee experts Dr. (Smt.) Bharati M. Reshmi and Dr. (Smt.) Shobha R. Patil, Basveshwar Engineering College, Bagalkot, for their valuable suggestions and guidance throughout my research phase.

Sincere thanks to the authorities, faculty, and staff of BLDEA's V.P. Dr. P. G. Halakatti College of Engineering and Technology, Vijayapur, for their untiring support and the pleasant working atmosphere. Special thanks to my fellow researcher, Mrs. Sumangala Biradar for her concern and intellectual support. It would have been impossible without the intellectual support of Dr. R. S. Malladi. The moral support of Dr. Mukta M. Bannur and Prof. Sujata Desai is always remembered with gratitude.

Special thanks to Dr. Jagadeesh Pujari, SDMCET, Dharawad, and Dr. Rohini Bhusnurmath, Akkamahadevi Women's University, Vijayapura, who shared their valuable time and knowledge with me.

Finally, I share this success with my husband, Mr. B. N. Khyadagi for his invaluable companionship, warmth support, understanding, and encouragement throughout. My son Dhruv and daughter Samruddhi deserve special thanks, who sacrificed so many things of their childhood for me and made this journey a pleasant one.

Sunanda Biradar

# CONTENTS

# LIST OF FIGURES

| Figure No. | Figure Caption |
|---|---|
| Fig. 4.3 | Different stages of detecting initial contour for polycystic renal US image : (a) Despeckled image (b) Binary image (c) Eroded image (d) Image after morphological opening (e) Final image with distinct regions |
| Fig. 4.4 | Different stages of segmentation of single-cystic renal US image : (a) Automatically generated initial contour (b) Intermediate deformation at the end of iteration number 60 (c) Finally deformed boundary at the end of iteration number 75 (d) Manually marked image by a medical expert |
| Fig. 4.5 | Segmentation of polycystic renal US image: (a) Original input image (b) Automatically generated initial contour (c) Finally deformed boundary by ACM at the end of 90 iterations (d) Manually marked image by a medical expert. |
| Fig. 4.6. | Results of cysts segmentation using proposed ACM algorithm |
| Fig. 4.7 | Performance analysis for single cyst segmentation in renal US images |
| Fig. 4.8 | Statistical parameters for single cyst segmentation in renal US images |
| Fig. 4.9 | Performance analysis for polycysts segmentation in renal US images |
| Fig. 4.10 | Statistical parameters for polycysts segmentation in renal US images |
| Fig. 5.1 | Generation of automatic initial contour for renal calculus US image |
| Fig. 5.2 | Sample images : (a) Single-cystic renal US image (b) Polycystic renal US image (c) Single renal calculus US image (d) Multiple-stones renal US image |
| Fig. 5.3 | Segmentation of single-cystic image : (a) Image with initial contour (b)Nature of LSF at initial stage (c) Finally deformed image at the end of 305 iterations (d) Nature of LSF at the end of deformation |
| Fig. 5.4 | Segmentation of polycystic image : (a) Image with initial contour (b)Nature of LSF at initial stage (c) Finally deformed image at the end of 322 iterations (d) Nature of LSF at the end of deformation |

| Figure No. | Figure Caption |
|---|---|
| Fig. 5.5 | Results of segmentation of cysts in kidney US images using level set |
| Fig. 5.6 | Segmentation of single-stone image : (a) Automatic initial contour at the first time application of level set (b) Final segmented contour at the end of the first time application after 300 iterations (c) Refined initial contour for the second time application of level set (d) Final segmented contour at the end of the second time application after 165 iterations |
| Fig. 5.7 | Segmentation of multiple-stone image : (a) Initial contour at first time application of level set (b) Final segmented contour at the end of the first time application after 224 iterations (c) Refined initial contour for the second time application of level set (d) Final segmented contour at the end of the second time application after 162 iterations |
| Fig. 5.8 | Results of kidney stones segmentation using level set method |
| Fig. 5.9 | Performance parameters for single cyst segmentation in renal US images |
| Fig. 5.10 | Statistical parameters for single cyst segmentation in renal US images |
| Fig. 5.11 | Performance parameters for polycysts segmentation in renal US images |
| Fig. 5.12 | Statistical parameters for polycysts segmentation in renal US images |
| Fig. 5.13 | Performance analysis for segmentation of single stone kidney images |
| Fig. 5.14 | Performance analysis for segmentation of multiple-stones kidney images |
| Fig. 6.1 | Proposed method for feature extraction and classification of kidney US images |
| Fig. 6.2 | Sample input images : (a) Normal US image of kidney (b) Single cystic US kidney image (c) Polycystic kidney image (d) Single stone kidney image (e) Multiple-stones kidney image |
| Fig. 6.3 | Average accuracy for k-NN, fuzzy k-NN and SVM using individual feature sets |

**Figure No.** **Figure Caption**

# LIST OF TABLES

# LIST OF SYMBOLS

| Symbol | Meaning |
|---|---|
| $\circ$ | Morphological open operator |
| $\bullet$ | Morphological close operator |
| $\nabla^2$ | Laplacian operator |
| $m_j(T)$ | Member of a sample T |
| $\chi 2$ | Chi- square |
| $\oplus$ | Morphological dilation operator |
| $\ominus$ | Morphological erosion operator |
| $\mu$ | Mean |
| $\xi(x.y)$ | Speckle noise |
| $\Sigma$ | Variance |
| $\Omega$ | Image domain |
| A | Initial contour |
| $A(\Theta)$ | Weighted area |
| $A_1$ | Average intensity in the interior of contour |
| $A_2$ | Average intensity in the exterior of contour |
| Acc | Accuracy |
| $C_i$ | $i^{th}$ class in k-NN and fuzzy k-NN |
| del | Dirac Delta function |
| Di(T) | Decision function on sample T for k-NN |
| dist(T,Ci) | Distance between sample T and class Ci |
| E | Energy |
| $E_{ext}$ | External force |
| f(x,y) | Edge map |
| $false_n$ | False negative |
| $false_p$ | False positive |
| H | Homogeneity |
| $H_0$ | Null hypothesis |

| Symbol | Meaning |
|---|---|
| $H_k$ | Histogram equalized image |
| Hs | Heaviside function |
| I(x,y) | Acquired image |
| I1 | Segmented region of image |
| I2 | Manually annotated region of image |
| L | Number of gray level |
| L(ɵ) | Line integral |
| $M_1$ | Size of structuring element used for opening |
| $M_2$ | Size of structuring element used for erosion |
| $(m_1,n_1)$ | Left end point of the axis enclosing the segmented region |
| $(m_2,n_2)$ | Right end point of the axis enclosing the segmented Region |
| Maj_axis | Major axis |
| Min_axis | Minor axis |
| O | Segmented renal cystic/stone image |
| P | Number of pixels covering the cyst region |
| Pi $(r)$ | Probability density function at gray level i |
| Pr | Maximum probability |
| Q | Structuring element |
| Rx(Θ) | Distance regulization term |
| S(m,n) | Despeckled image |
| S1 | Clinical image dataset |
| S2 | Public image dataset |
| sim(T,Ci) | Similarity between sample T and class Ci |
| Sn | Sensitivity |
| Sp | Specificity |
| T | Image sample to be classified |
| $true_n$ | True negative |
| $true_p$ | True positive |
| U(x,y) | Actual ultrasound image |
| $(x_1,y_1)$ | Top corner of the initial contour rectangle |
| $(x_2,y_2)$ | Bottom corner of the initial contour rectangle |

# LIST OF ABBREVIATIONS

| Acronym | Expansion |
|---|---|
| ACM | Active Contour Model |
| ADPKD | Autosomal Dominant Polycystic Kidney Disease |
| ANFIS | Adaptive Neuro Fuzzy Inference System |
| ARPKD | Autosomal Recessive Polycystic Kidney Disease |
| CC | Correlation Coefficient |
| CKD | Chronic Kidney Disease |
| CPU | Central Processing Unit |
| CT | Computed Tomography |
| C-V | Chan-Vase |
| DRT | Distance Regularization Term |
| DC | Dice Similarity Coefficient |
| DWT | Discrete Wavelet Transform |
| GA | Genetic Algorithm |
| GLCM | Gray Level Co-Occurrence Matrix |
| GVF | Gradient Vector Force |
| HOG | Histogram of Oriented Gradient |
| IDM | Inverse Difference Moment |
| ISN | International Society of Nephrology |
| JC | Jaccard Coefficient |
| k-NN | K-Nearest Neighbors |
| LP | Laplacian Pyramid |
| LSF | Level Set Function |
| MAP | Maximum A Posteriori |
| MRI | Magnetic Resonance Imaging |
| MSE | Mean Square Error |
| PCKD | Polycystic Kidney Disease |
| PSNR | Peak Signal to Noise Ratio |
| ROI | Region of Interest |

| Acronym | Expansion |
|---|---|
| SNR | Signal to Noise Ratio |
| SVM | Support Vector Machine |
| US | Ultrasound |
| UTI | Urinary Tract Infections |

# ABSTRACT

Kidney disease is recognized as a worldwide public health problem. The growth of kidney disease has gradually increased in recent years. Kidney disease is usually a progressive disease, which means that the damage in the kidney tends to be permanent and cannot be undone. So it is important to identify kidney disease early before the damage is done. Kidney disease can be treated very effectively if it is identified in the early stages. This is very important since kidney diseases also increase the risks of heart disease and stroke.

Modern engineering and technical tools can be applied for fostering proper diagnostics to get the best results. Digital image processing becomes more and more important in health care because of the increasing use of direct digital imaging systems for medical diagnostics. The most important tool in medical application is medical imaging. Proper medical treatment begins with a correct diagnosis. Medical imaging provides a wealth of information and challenges to the physicians. Medical image processing deals with the development of problem-specific approaches to the enhancement of raw medical image data for selective visualization as well as further analysis. It aims at assisting medical experts in their decisions by providing quantitative measures inferred from various imaging modalities like ultrasound (US), Computed Tomography (CT), and Magnetic Resonance Imaging (MRI), etc. Medical imaging, particularly ultrasound imaging is the most commonly used primary diagnostic tool by the medical experts. It provides the internal structure of the body to detect eventually diseases or abnormal tissues non-invasively.

The main aim of the research study is to develop an efficient and effective system to detect, analyze the cysts and stones in ultrasound images of the kidney. The system can assist the physicians to identify the disease, by means of providing a clearer view of the affected regions. Adverse outcomes of kidney diseases can be prevented through early detection and treatment.

The work carried out is divided into speckle noise removal, automatic initial contour detection, applying segmentation on these images to get the ROI of the kidney (in case of the normal kidney) or diseased portion of the kidney (in case of cystic and kidney stones), extracting optimal features from these segmented ROIs to classify them into a suitable class.

The work starts with the collection of input ultrasound images of the kidney for experimentation. Ultrasound images of normal kidney, cystic, and kidney stone are considered for the research work. Removal of speckle noise is one of the essential primary stages of research work. Experimentation is carried out using various filters like Gaussian, median, and Weiner. The transforms like wavelet and contourlet transform are also used effectively for the despeckling of ultrasound images of the kidney. Contourlet transform performs comparatively better than the other methods in case of ultrasound images of the kidney. The performance parameters like mean square error (MSE), peak signal noise to ratio (PSNR), and correlation coefficient (CC) are used for evaluation. Hence denoised US images of the kidney using contourlet transform followed by contrast enhancement are used for the segmentation process.

Segmentation plays an essential role in all kinds of image analysis. In medical image analysis, segmentation has a great clinical value. To deal with boundary insufficiencies, missing edges, and lack of texture contrast between ROIs and background, segmentation is used. It identifies the boundaries of the objects. Segmentation of the required region in the ultrasound image is one of the challenging tasks. The segmentation and analysis of the region of interest in the ultrasound image is a difficult task due to the shape variant objects, orientation, and poor image quality. The proposed method focuses on the segmentation of cyst and stone in an image.

A semiautomatic method of segmentation is performed using GVF effectively to segment kidney, single-cystic and single-stone images. But it needs an initial contour to be specified as user input. To resolve the drawbacks of GVF based segmentation an automatic segmentation method for cystic images is proposed using ACM. Initial contour for segmentation, closer to the actual cysts boundaries is obtained automatically using morphological operations. It can effectively segment the single cystic images automatically. But, it segments a single larger contour enclosing all the cysts in polycystic kidney US image. An automatic novel approach for automatic kidney cysts and stone segmentation using level set method is proposed to overcome the drawbacks of GVF and ACM based segmentation methods. Completely automated segmentation of cysts and stones is mainly addressed in the work proposed. The level set algorithm effectively segments normal kidney, cysts, and stones in ultrasound images of the kidney. The level set is fully automated and

demonstrates better performance in segmentation. Further, the diagnostic parameters essentially needed by medical experts, namely, the number of cysts/stones including the size are calculated. The developed method is evaluated using performance parameters such as Jaccard coefficient, Dice coefficient, sensitivity, specificity, accuracy, and amount of execution time. The efficacy of the developed approach is proved by the results of the experiment. It takes less computational time comparatively. The method is tested using Chi-square to analyze how significantly the obtained values vary from the expert-determined values. The acceptable range of the test shows the efficacy of the method. Hence, the level set segmented US images of the kidney are used for feature extraction and classification process.

A texture can be informally defined as a perceptually homogeneous irradiance pattern. Using five different feature extraction techniques, the texture pattern of the kidney region is diagnosed and classified automatically. The five feature sets namely Haralick features, shape features, wavelet features, Tamura features, and HOG features are applied individually and in combination for renal US image. Extracted feature vectors are used as inputs for three different classifiers namely k-NN, fuzzy k-NN, and SVM. The performance of the decision support systems is analyzed using accuracy and time taken for execution. The better accuracy rate is found using fuzzy k-NN with combined features set to classify the kidney US images into normal kidney, single-cystic, polycystic, single-stone, and multiple-stones classes. The performance of the classifiers is measured using sensitivity, specificity, accuracy, precision, recall, and F1 score.

To provide an easy to use interface to the radiologists, medical professionals, and patients an Android application is developed. It facilitates the real-time viewing of segmented and classified results of US images of kidney on smartphones. The work carried out has interesting applications in the field of medical image analysis in particular for the analysis of ultrasound images of the kidney. The analytical information obtained from segmented kidney medical ultrasound images such as the number of cysts and stones along with the size can be used by the medical experts for precise treatment. The work has a scope of extension in real-time for mass screening to obtain the results in lesser time.

# Chapter 1

# INTRODUCTION

## 1.1 Medical imaging

Data representation in an image format has its own importance and effect, rather than textual representation. The data with good visual appearance is quickly perceived by human beings. It is quickly analyzed and understood by human beings. Digital image processing is a computer-based technology, carries out manipulation, automatic processing, and performed interpretation of such visual information. It plays a highly significant role in many aspects of our daily life. It can be applied to a wider variety of disciplines and fields. Image processing is an evolving field with enormous applications in science and technology. It is mainly concerned with the use of computerized algorithms on images. It tries to develop the ultimate machine with the possibility of performing the visual functions of living beings.

Digital image processing covers a wide range of applications, such as remote sensing through satellites, image transfer, storage for business applications, medical image processing, radar, sonar, acoustic image processing, robotics, automated inspection of industrial parts and many more. Image processing is basically developed for two-dimensional images. But, now it can be modeled for three and multidimensional images. Automation has major benefits in many fields including agricultural, marketing, medical fields and many other fields as well.

In the recent eras, there has been a significant increase in the level of interest in image morphology, artificial intelligence, machine learning, color image processing, image recognition, and knowledge-based image analysis system. The principal goal of image analysis by computer is to endow a machine with the capability to approximate, in some sense, a similar capability exhibited by human beings. Thus, an automated image analysis system should be capable of performing the aforementioned tasks with varying degrees of intelligence.

In medical applications, processing of chest X-rays, cine angiograms, projection images of transactional tomography, other medical images that occur in radiology, nuclear magnetic

resonance, and ultrasonic scanning are being carried out. These images may be used for patient screening and monitoring or detection of tumors or other diseases in patients.

Medical imaging is one of the most important tools in medical applications. Medical imaging provides a wealth of information and challenges to the physicians. Digital image processing plays a vital role in health care because of the increasing use of direct digital imaging systems for medical diagnostics. It refers to different techniques that are helpful to assess the human body to diagnose and treatment of diseases. This technology provides important information regarding the organ under study or treatment. Medical image processing deals with the development of problem-specific approaches to the enhancement of raw medical image data. Medical imaging creates a visual representation of the internal view of an organ for clinical analysis. This assists to observe the functionalities of organs or tissues (physiology). It reveals the internal structures under the skin and bones. Medical imaging helps to establish a database of normal anatomy/physiology to make it possible to identify abnormalities. Although imaging of removed organs and tissues can be performed for medical reasons, such procedures are usually considered part of pathology instead of medical imaging. The main purpose of medical image processing is selective visualization and image analysis. It aims at assisting medical experts in their decisions by providing quantitative measures inferred from various imaging modalities like Ultrasound (US), Computed Tomography (CT), Magnetic Resonance Imaging (MRI), X-rays and many more.

Ultrasonic imaging has been used in medical diagnosis for more than half a century (Paul Suetens, 2002). Ultrasound contributes to faster, better, safer and in-time diagnostics. It is used for diagnosis of the abdominal area, including liver, gall -bladder, kidneys, spleen, pancreas, uterus, ovaries, aorta space, periaortic space, prostate gland, and adrenal gland. The ultrasound imaging allows faster and more accurate procedures due to its real-time capabilities. The noninvasive, non-radioactive and inexpensive properties of US images lead to widespread application in diagnosing soft tissue organs (Hagen-Ansert S,1995 ; H. M. Pollack and B. L. McClennan, 2000).

## 1.2 Ultrasound imaging

Ultrasound imaging works on high-frequency sound waves. Ultrasound images have the advantage of capturing the images in real-time. Therefore, they are capable to show the

movements of the internal organs. They can visualize the blood flow in the vessels. Ultrasound images are captured without exposing to harmful radiation. Ultrasound imaging has many advantages in the evaluation, diagnosis, and treatment of medical disorders. Some of the commonly used procedures are:

a. Abdominal ultrasound to observe abdominal tissues/and organs

b. Bone sonometry to evaluate frangibleness of bones

c. Sonomammography to observe breast tissue

d. Doppler ultrasound to monitor blood flow through blood vessels

e. Echocardiography to view the heart functioning

f. Fetal ultrasound to monitor the fetus in pregnant women

g. Ultrasound-guided biopsy for collecting a tissue sample

h. Ocular echography to test eye structures

### 1.2.1 Ultrasound machine

Medical ultrasound scanning is performed by the ultrasound machine. A basic ultrasound machine is shown Fig.1.1.

A typical ultrasound machine has components such as transducer probe, processor, transmitter or pulser, display, keyboard, printer, and storage device. A transducer converts energy in one form to another form. In this case, electrical energy is converted to mechanical energy. It serves the purpose of a receiver of reflected acoustic waves as well. It works on the principle of piezoelectricity. The processor is required to identify, manipulate and process the reflected pulse in creating the image for display and storage. The transmitter controls the amplitude, frequency, and duration of the pulses produced by the transducer. It controls the time interval between ultrasound pulses as well. The ultrasound waves must have enough intervals between the waves in order to reach the desired depth. Further, the wave should be reflected back before the next wave is sent (Cobbold and Richard S. C., 2007). The display

unit displays the ultrasound image. It is the ultrasound data processed by the CPU. The ultrasound machine has a very lesser built-in memory. So, it needs an external storage device to store the captured images.

Fig.1.1. Ultrasound machine

*Image Credit:*wikimedia.org/wikipedia/commons/AlokaPhoto2006a.jpg/

Ultrasound scanning is carried out by a skilled technician, called a sonographer. A special lubricating gel is applied on the skin of a patient to be scanned. The sound is focused through the shape of the transducer. A typical transducer is shown in Fig. 1.2. The gel prevents friction while rubbing the transducer on the skin and facilitates the efficient transfer of energy from the transducer to the body.

The electrical pulses generated by the ultrasound machine drives the transducer for the emission of high-frequency waves. Wave is reflected whenever there is a change in acoustic impedance like hitting an opaque element, such as an organ or bone. These echoes are partially reflected back to a computer. Some of them are reflected back to the transducer. These sound waves are having a high-frequency range of 1MHz to 18MHz. This range is above the audible frequency range of human beings. The returned sound waves cause the vibration of the transducer which is turned into electrical pulses by the transducer.

These pulses are processed and converted to a digital image called ultrasound image.

Fig. 1.2 Transducer

*Image Credit:*wikipedia.org/wiki/File:UltrasoundProbe2006a

### 1.2.2 Ultrasound image formation

The image forming process by an ultrasound scanner is dependent on two main factors:

- The duration taken to receive the reflections back after sending the initial sound wave
- Strength of echo

The duration determines the pixel location. Longer duration results into more depth of the pixel location. The intensity of the pixel is decided by the strength. A strong echo is represented by white pixel and the weakest echo is by black pixel. Intermediate values form the various gray intensities forming a gray scale image.

A two-dimensional image is obtained by swiping a transducer mechanically against the skin. As an alternative, 1-D phased array transducer can be used to sweep the beam electronically. The reflected wave is processed to construct the 2-D image, representing a slice of the human body. Three-dimensional images are framed by capturing a series of adjacent two-dimensional images. A specialized probe is used. It is hard to acquire 3-D images of moving tissue because of the slow process of mechanical scanning. Hence, the 2-D phased array transducer is under use for 3-D image acquisition. It captures the images quickly and facilitates 3-D live images.

### 1.2.3 Modes of ultrasound imaging

Ultrasound images can be displayed in various modes from simple A- mode to high-resolution images (Carol M. Rumack and Deborah Levine, 2018 ; N. R. Dunnick, Carl M. Sandler and Jefry H.N, 2013).

- *A – (Amplitude) mode:* It is the earliest and simplest mode of imaging where the devices used position and strength of echoes to frame the image. The voltage generated by the reflected wave through the transducer on the surface of an oscilloscope is processed and displayed. A single transducer is used for scanning. Fig. 1.3 shows a sample A-mode ultrasound image. It displays the amplitude spikes. As shown in Fig 1.3, it has X and Y axis, where X denotes the depth and Y shows amplitude.

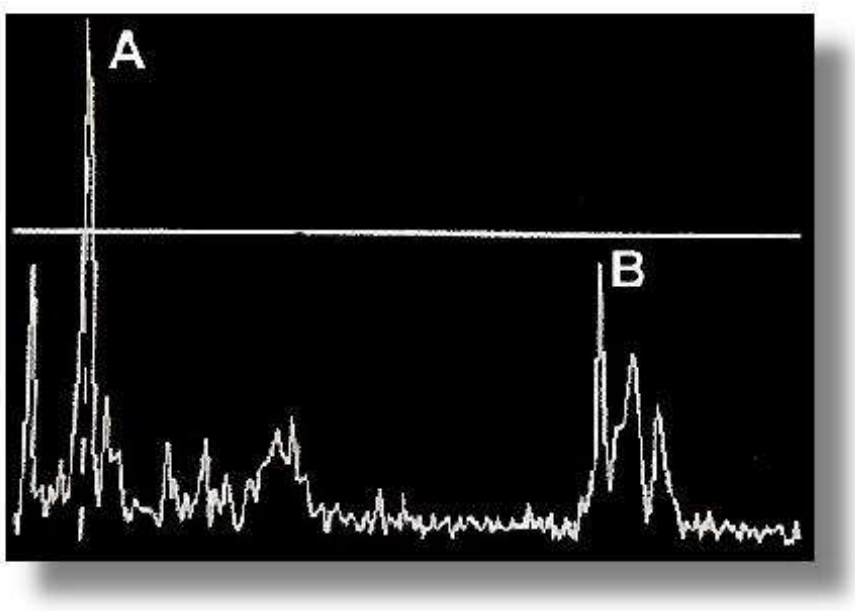


Fig. 1.3. A sample A-mode ultrasound image
*Image Credit:* sonodriftzone.blogspot.com

- *M – (Motion) mode:* It is another simple mode of imaging. It displays the reflected wave amplitudes. Mainly it shows the position of moving structures. The brightness of the display is used to specify the intensity of the echoed pulse. M-mode image has an important application such as assessment of fetal heart rates. A sample M-mode image is shown in Fig. 1.4.

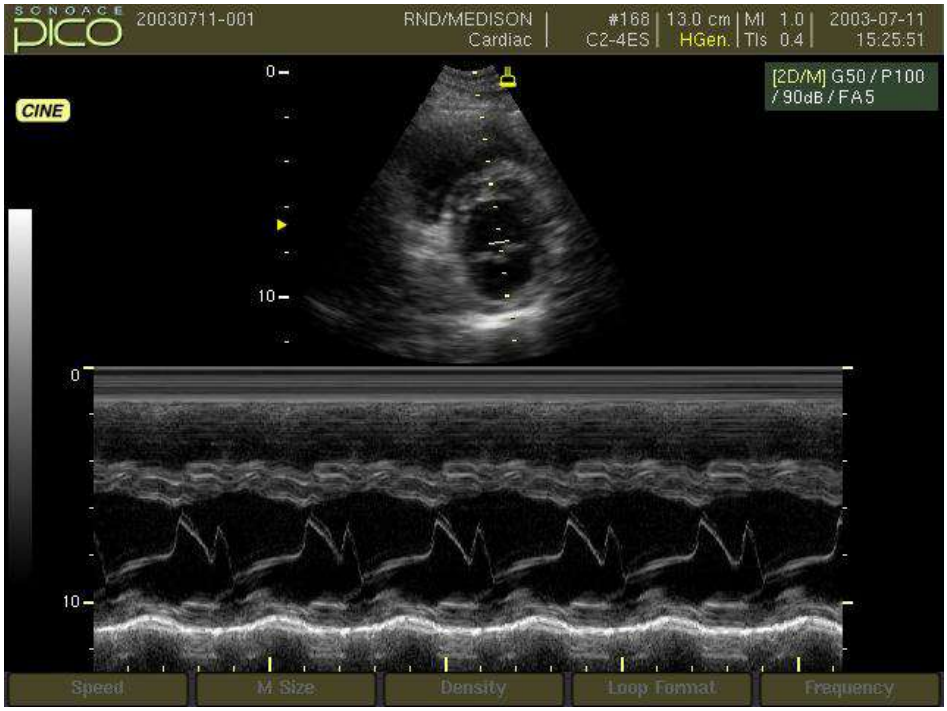


Fig. 1.4. A sample M-mode ultrasound image

*Image Credit:* medison.ru/ultrasound/

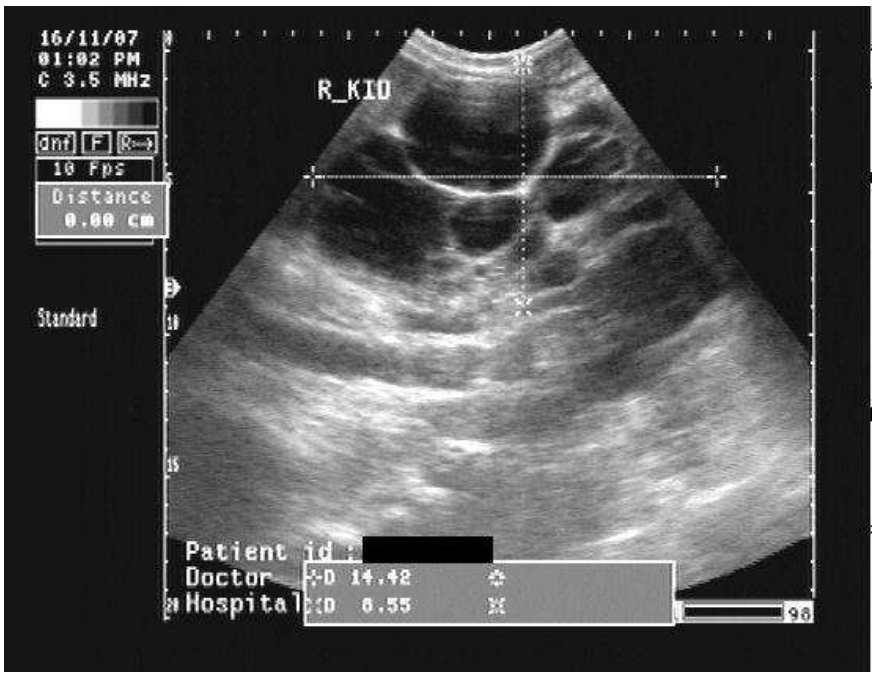


Fig. 1.5. A sample B-mode ultrasound image

*Image Credit:* medison.ru/ultrasound/

- *B – (Brightness) mode:* It is the major and important imaging mode. It provides real-time, gray scale images. It uses a linear array of transducers simultaneously. It creates the two-dimensional view of a body organ. Hence, it is known as a 2-D mode. B-mode display uses the strength of reflected wave to a particular brightness level in the display device. A sample B-mode image is shown in Fig. 1.5.

- *Doppler mode:* It uses the Doppler effect for measurement and visualization of blood flow. A sample Doppler image is shown in Fig. 1.6. Doppler sonography is meant for studying the blood flow and muscle movements. Different speeds of motions are represented in different colors for easy interpretation. Colors are used to show the varying amplitudes of the reflected waves.

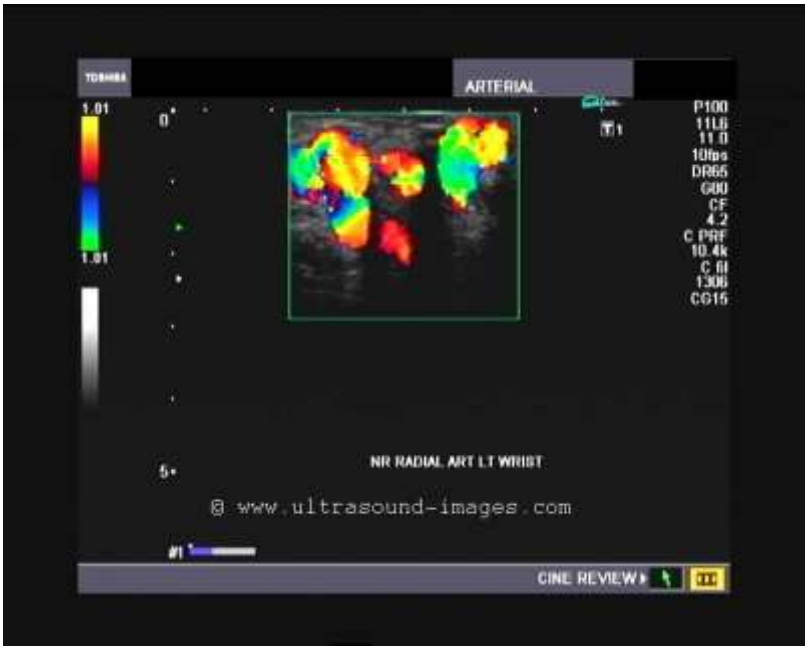


Fig. 1.6. A sample Doppler mode ultrasound image
*Image Credit:* medison.ru/ultrasound/

## 1.3 Kidney anatomy

The major function of the kidney is to filter blood. The kidneys filter about 180 liters of blood every day. The filtering process regulates water-salt and acid-base balance for water homeostasis. The kidney has a length of approximately 15cm, width of 5cm and thickness of 2.5cm. It has a weight of 120g – 170g. The volume of the left kidney is larger than that of the

right kidney. Length of kidney is correlated with body height. The kidney size goes on decreasing with aging (N. R. Dunnick, Carl M. Sandler and Jefry H.N, 2013). The kidneys have a mobility nature, they move as per body position. Fig. 1.7 shows the anatomy of kidney.

The kidneys are protected by perirenal fat, from external damage. The concave surface of the kidney is known as renal hilum. The surface is continuous connecting the structures such as nerves, ureters, vessels, and lymphatics.

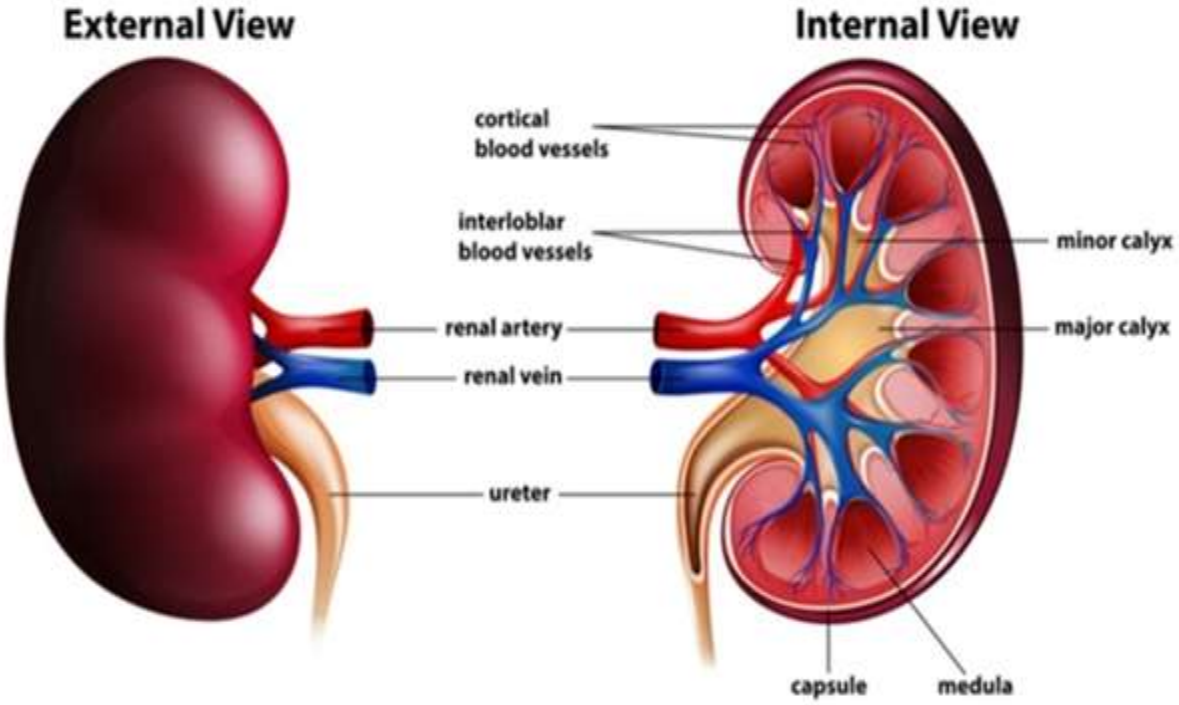


Fig. 1.7. Anatomy of kidney
*Image Credit:* BlueRingMedia/Shutterstock

Renal arteries supply the blood to the kidneys. The renal artery is a main branch of the abdominal aorta. These arteries are divided into multiple levels, forming a specialized network. These form the special capillary beds known as glomeruli. Every glomerulus formulates one component of a nephron. The filtered blood moves within the left and right renal veins. These veins are vacated in the inferior vena cava and in turn to the heart.

Nephrons are the structural units of the kidney. There are about 1.3 million nephrons in each kidney. Fig. 1.8 describes the nephron structure. Two major parts of nephrons are tubules and corpuscles. The corpuscles comprise of glomeruli. The tubules are small tubes traveling through the interior of the kidney. These are responsible for regulating the chemicals in the blood.

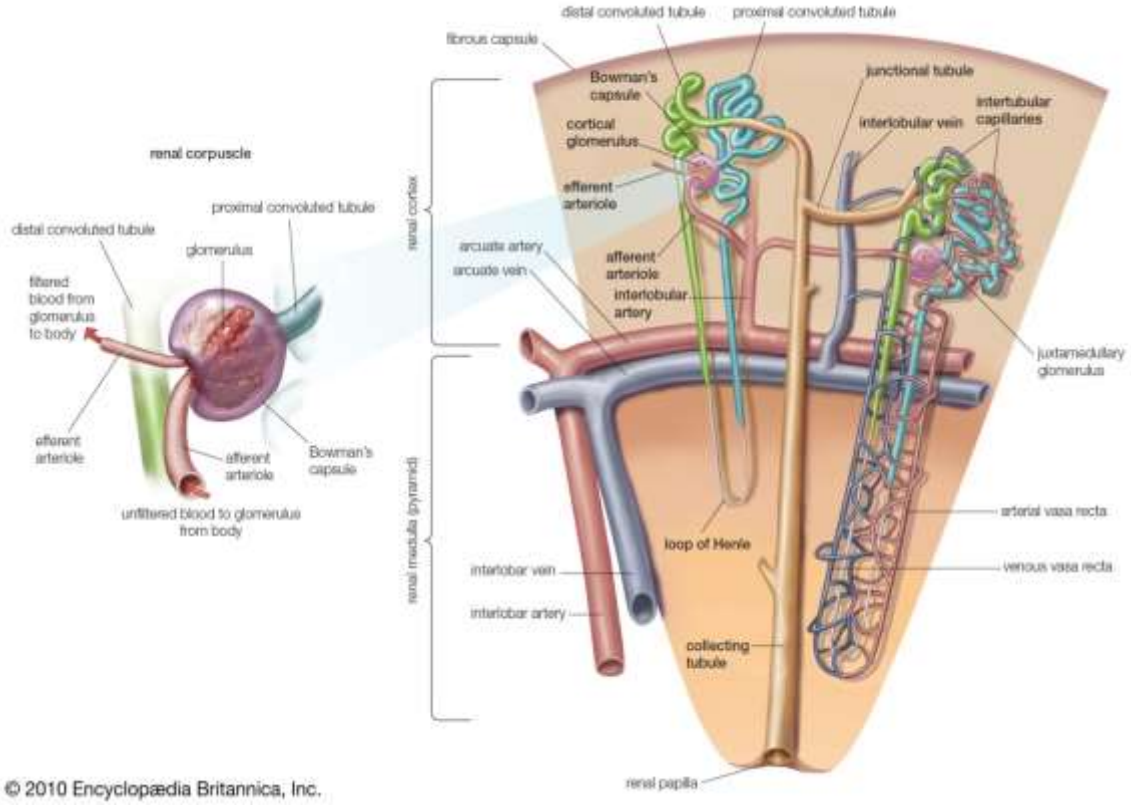


Fig. 1.8. Anatomy of nephron
*Image Credit:* Encyclopaedia Britannica, Inc.

The cortex is the outer tissue present beneath the renal capsule. It reaches the inner renal tissue and splits triangular structures called pyramids. The urine formed inside the pyramids is stored in a structure known as the minor calyx. Different minor calices combine forming a major calyx. Urine flows from the major calices to the renal pelvis. The pelvis is a structure formed by the fusion of all major calices. It transmits urine from the kidney to the ureter.

## 1.4 Kidney diseases

Kidney diseases are one of the world-wide financial burdens. Most of the people do not know about their impaired kidney functions. Most of the time, kidney diseases do not show symptoms at the early stages. Many patients are not aware even at the highly risky conditions like kidney failure that may need dialysis or transplantation. The abnormalities of kidneys can lead to cardiovascular diseases, infections, and hospitalizations. It is estimated that globally more than 850 million people have one or the other kind of kidney disorders. This count is roughly double the number of diabetic patients (422 million, (http://www.who.int/news-room/fact-sheets/detail/diabetes)) and over 20 times than that of cancer (42 million (https://ourworldindata.org/cancer)) or more than AIDS/HIV (36.7 million (http://www.who.int/gho/hiv/en/)) patients. Thus, kidney disorders are one of the common diseases all over the world. David Harris and Adeera Levin of the International Society of Nephrology (ISN) explain as “It is high time to put the global spread of kidney diseases into focus”. It is found that kidney disorders enforce heavy expenditure. Table 1.1 shows the annual expense incurred on dialysis by various countries. The annual expense per patient for dialysis ranges between Int.$3,424 to Int.$ 42,785 (Carovac A, Smajlovic F and Junuzovic D, 2011).

Table 1.1. Cost of dialysis in various countries

| **Country** | **Approx. cost per annum (in USD)** |
|---|---|
| United States of America | 88,000 |
| Netherlands | 84,000 |
| Belgium | 84,000 |
| France | 71,000 |
| Germany | 33,000 to 59,000 |
| United Kingdom | 39,000 |

Every day 1.5 lakhs to 2 lakhs people undergo dialysis in India (Vijayavani (kannada daily), 2019). In order to create awareness, the 2$^{nd}$ Thursday of March is celebrated as "World Kidney Day", every year. It is very essential to diagnose and treat kidney diseases in the earlier stage. More than 1.5 million people globally are currently alive on renal replacement

therapy, either by dialysis or with a functioning graft. The incidence of renal failure has increased in the last 15 years. Kidney stones (renal calculi) affect up to 5% of the population, with a lifetime risk of passing a kidney stone of about 8-10%. Increased incidence of kidney stones in the industrialized world is associated with improved standards of living. It is strongly associated with race or ethnicity and region of residence (Shah J and Whitfield H. N.,2002). Kidney disease is usually a progressive disease, which means that the damage in the kidney tends to be permanent and cannot be undone. So it is important to identify kidney disease early before the kidney gets damaged. Kidney disease can be treated very effectively if it is diagnosed in the early stages. This is very important since kidney diseases can increase the risks of heart disease and stroke.

Usually, kidney diseases cause degraded functionality over the years. This is known as "chronic kidney disease (CKD)". Different reasons for CKD are high blood pressure, glomerulonephritis, polycystic kidney disease (PCKD), reflux nephropathy and sometimes the cause is not known. There are different health issues that can harm the kidneys leading to CKD. They are PCKD, lupus nephritis, kidney cancer, and other rare diseases.

### 1.4.1 Polycystic kidney disease

Polycystic kidney disease (PKD or PCKD, also known as polycystic kidney syndrome) is a cystic genetic disorder of the kidneys. PKD is characterized by the presence of multiple cysts. Renal cysts are non-cancerous and fluid-filled. They can be numerous, leading to enlargement of the kidney. The occurrence of cysts increases with aging. 30% of people above 60 years are prone to cysts. Most of the cysts are asymptomatic. However larger cysts cause flank pain or hematuria.

The 17% of cases primarily diagnosed for PKD disease in one kidney, progressed to bilateral disease in adulthood. The disease can in turn damage the liver, pancreas and, in some rare

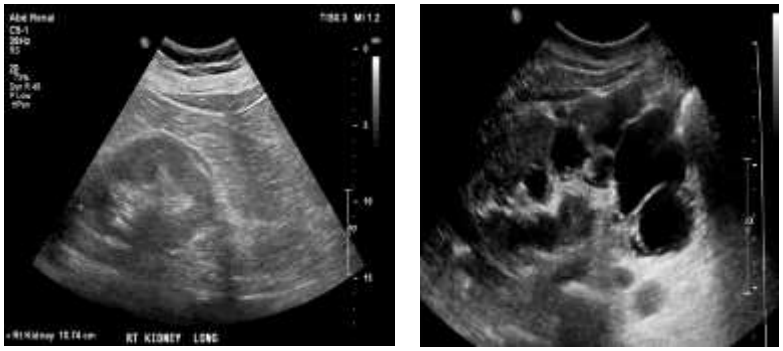

(a) (b)

Fig. 1.9. Sample images: (a) Normal kidney (b) Polycystic kidney
(*Image Credit :*radiopaedia.org) (*Image Credit:*nephsim.com)

cases, the heart, brain. Polycystic kidney disease is one of the common life-threatening genetic diseases. In recent years, the potential use of computer-aided diagnosis in the field of medical imaging in general and kidney images, in particular, has been the area for rigorous research.

PKD is a disorder in which groups of cysts develop primarily in kidneys. This leads to enlargement of kidneys, and they do not function properly over time. Cysts are nonmalignant type. The cysts differ in size. They can grow to a very large size. Presence of multiple cysts or larger cysts can destroy the kidneys. Further, PKD can lead to cysts development in the liver and other organs at the later stages of the disease. The disease can lead to many other complications in turn. PKD has different levels of severity. Some complications are preventable and controllable. Fig. 1.9 shows the normal and polycystic kidney.

The two types of polycystic kidney disease classified on genetic defects are:

- *Autosomal dominant polycystic kidney disease (ADPKD):* The symptoms of ADPKD often appear among the population in the age group of 30 to 40. Before, it was known as adult polycystic kidney disease, but kids can also face this problem. This disease is inherited only if anyone parent has the disorder. If one parent has ADPKD, there is a 50% chance of disease getting inherited to the child. This type of disease accounts for 90% of the cases of PKD.
- *Autosomal recessive polycystic kidney disease (ARPKD):* This type is very uncommon than ADPKD. The symptoms usually are seen after birth. Sometimes, symptoms do not

appear in childhood. This disease is inherited only if both the parents have the disorder. There is a 25% chance of disease getting inherited.

The other major complications with PKD are listed below:

- *Hypertension*: It is a commonly observed complication of polycystic kidney disease. If it is not treated earlier, it can lead to kidney failure and an increased risk of heart problems and stroke.
- *Impairment in kidney function*: It is one of the serious complications. Around 50% of the PCKD patients face this problem in turn leading to kidney failure.
- *Pregnancy complications*: Along with pregnancy complication, some women may be prone to a life-threatening disease called preeclampsia.
- *Development of cysts in the liver*: The chance of finding liver cysts in aged patients with PKD is more.
- *Brain aneurysm*: A bulged blood vessel (aneurysm) in the brain can also cause hemorrhage. Patients with a family background of aneurysm have a high risk.
- *Heart valve abnormality*: This leads to improper closing of the valve, which causes the blood leakage in a backward direction.
- *Colon disorders*: Weakness and sacs in the colon wall may be observed.
- *Pain*: Pain in back, side or pain due to urinary tract infection is commonly observed symptom.

### 1.4.2 Kidney stones or renal calculi

Renal stone is one of the common problem faced all over the world. These stones have afflicted the human population since the earlier civilizations. The discussion on the treatment of stones is found in the earliest Egyptian writing of 1500 BC (Shah J and Whitfield H. N.,2002 ; Michell A. R.,1989).

The earlier statements on the description of symptoms and treatment of dissolving the stones are available in the books of Asutu, Mesopotamia in the year 3200 and 1200 BC (Shah J and Whitfield H. N.,2002). The details on “cutting for the stone” is observed in Hindu and Greek literature. Sushruta (around 600 BC), an ancient Indian surgeon mentions “perineal

lithotomy" in his book "Sushruta Samhita" (Chakravorty R. C., 1969 ; Chakravorty R. C. ). The description of bladder stones is described in this text. Initial treatment recommendations to the patients like diet, consumption of water are observed. The surgical procedure is defined in detail in Sushruta's books (Chakravorty R. C.). Ancient Greeks made significant observations and documentation regarding urinary stones. Hippocrates (460–377BC) explained about kidney stones in his famous book, "Oath of Medical Ethics for physicians" (Dimopoulos C,et. al.,1980). In those days, lithotomy was under practice.

Kidney stones are the crystals made of different ion contents (Jack W. McAninch and Tom F. Lue, 2013). Based on the contents, they can be classified into various classes. The sample images of different renal stone types are shown in Fig. 1.10.

- *Calcium:* Calcium is the major and common stone type. These stones are composed of calcium oxalate or calcium phosphate. The deficiency of citrate leads to stone development. Estrogen enhances citrate excretion. Hence, calcium stone incidents are less in women, particularly during pregnancy.
- *Struvite:* This is commonly found in women with urinary tract infections (UTI). They are resultants of kidney infections. Handling the underlying infections may avoid the growth of struvite stone.
- *Uric acid:* This is commonly observed in men. Uric acid is generated during purine metabolism. These are found in patients treated for malignant conditions.
- *Cystine:* Cystine stones are rare. They are observed in people with genetic defects irrespective of the gender. The recurrence rate of these stones is very high.

The majority of renal stones induce the pain. The other symptoms include:

- blood in the urine (color change of urine)
- vomiting and nausea
- discolored or foul-smelling urine
- chills and fever
- frequent need to urinate
- urinating small amounts of urine

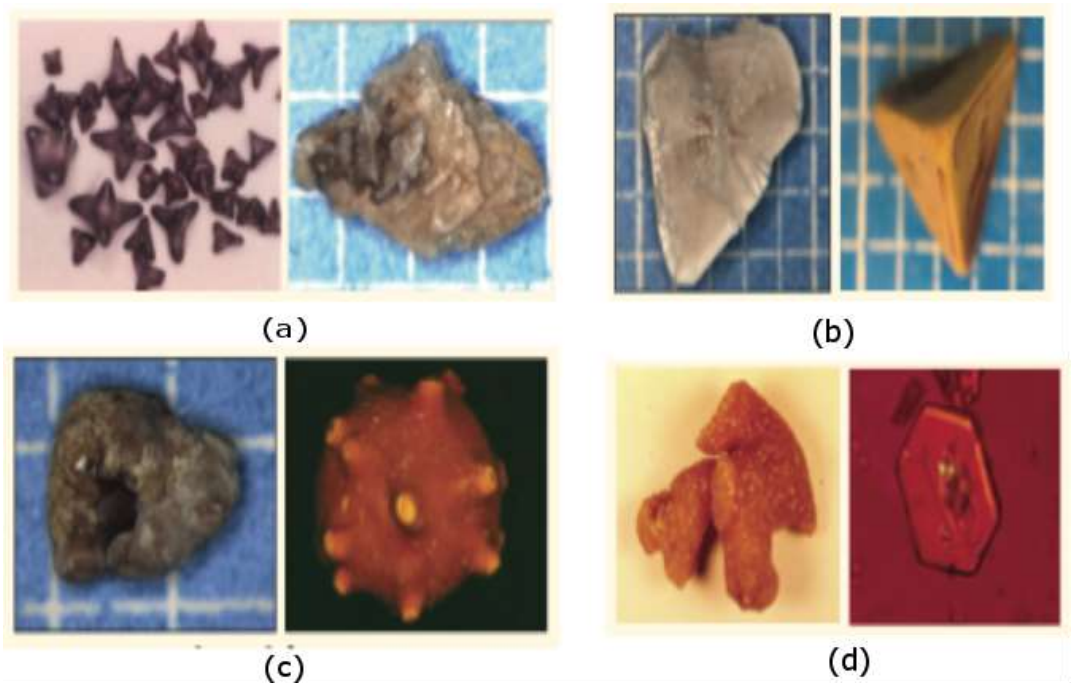


Fig. 1.10. Different types of renal stones: (a) Calcium (b) Struvite (c) Uric acid (d)Cystine

*Image Credit:* Louis C. Harring Company, Kidney Stone Analysis Laboratory www.herringlab.com

## 1.5 Image dataset

Medical renal ultrasound B-mode images having different sizes and varying orientations are used for the study. The input image dataset is categorized as S1(Clinical dataset) and S2 (Website dataset). The images in S1 are collected from BLDEDU's Shri. B.M. Patil Medical College and Research Centre, Vijayapur. These images are acquired using the GE LOGIQ 3 Expert system and Phillips HD11XE US system. Curvilinear transducer having a frequency range between 5 MHz to7MHz is used. The dataset is prepared by consulting the medical experts of the hospital. The images in S2 are downloaded from public websites (nlm.nih.gov, sonoworld.com, and ultrasoundimages.com). Totally 185 images are used for the experimentation; $S_1$ set contains 105 images and S2 contains 80 images. There are 37 normal kidney images, 39 single-cystic, 35 polycystic, 38 single-stone and 36 multiple-stones images altogether. The image datasets $S_1$and S2 are shown in the Appendix I.

## 1.6 Speckle noise removal

Speckle noise gives ultrasound images their characteristic granular appearance. It inherently exists in coherent imaging, including ultrasound imaging. The analysis of signal-dependent effect has been a major subject of investigation in the medical ultrasound imaging community as well as the optical (laser) and radar imaging communities. The texture appearance of the observed speckle-noise does not correspond to the underlying tissue structure. However, the local brightness of the speckle-noise pattern does reflect the local echogeneity of the underlying scatterers. The speckle noise with the signal carrying some information about the observed tissues can be undesirable and hence needs to be reduced, without loss of required information. To avoid the subjective diagnosis on raw US images, image processing is used to help the medical experts in better diagnosis of the images. Removal of noise is necessary for effective use of the segmentation and image analysis algorithms in producing the useful results.

Different methods and filters are available for denoising. Speckle noise is of multiplicative type. Multiplicative noise in the image has a feature of granular visibility, due to a low SNR. The multiplicative noise is converted into additive noise using logarithmic transform.

### 1.6.1 Logarithmic and inverse logarithmic transforms

The multiplicative noise has a log like term and is non-quadratic. Speckle noise has a nature of increasing with multiple factors. It is turned into additive type by applying logarithmic transform. The acquired image I(x,y) is shown (Hiremath P. S., Prema T. Akkasaligar and Sharan Badiger, 2011) as in Eq. (1.6.1).

$$I(x, y) \approx U(x, y)\, \xi(x, y) \tag{1.6.1}$$

where, U(x, y) is the actual ultrasound image and $\xi(x, y)$ is speckle noise. As shown in Eq. (1.6.1), noise is multiplied with true image. It is difficult to handle multiplicative noise. So, it is turned into additive type by applying the logarithmic transformation as in Eq. (1.6.2).

$$\log I \approx \log U + \log \xi \tag{1.6.2}$$

Thus, a multiplicative form is converted into additive term. The log transformed image undergoes despeckling process. The resultant image is applied with inverse logarithmic transform to get the denoised image.

### 1.6.2 Noise removal filters

Edges in the image are most widespread and essential features. Low pass filters are employed to eliminate high frequency noise from an image. This is because of high frequencies of noises and edge. Hence, some of the nonlinear filters like median filter and wavelet filer are most commonly used for denoising. However, the high-pass filters are used for image sharpening. These can enhance the finer details in the image.

#### *Gaussian low-pass filter*

In the Gaussian filter, frequency values to be filtered out are changing continuously throughout. The variation in filter frequencies depends on the Gaussian curve. The value is high at the center and keeps on decreasing as moved away from the center. Thus the resultant average frequency is largely biased by the central pixel frequency and its neighboring pixels. So, the Gaussian filter is better in preserving the edges compared to low-pass and average filters.

Sigma value is used to control the shape of the Gaussian curve. A large value of sigma leads to a broad and shorter peak of the kernel function. It smoothens the image with a low rate of edge preservation as it gives more weight to the pixels away from the central pixel.

#### *Median filter*

The median filter works on the principle of assigning the median of the pixels by taking into account of a specific sized window. The filter replaces each pixel by the median of the pixel values in the neighborhood of that pixel. For finding the median, input window pixels are arranged in the numerical order and central value is selected as a median. Median filter is efficient enough in the removal of random noise. It is good at the preservation of edges. But, it leads to elimination of thin lines.

### *Wiener filter*

The Wiener filter helps in inverting the blur and removal of the additive noise together. The Wiener filter is a linear filter. It supports image smoothening effectively. It is efficient comparatively and is measured with minimal mean square error.

Spatial domain-based despeckling methods directly manipulate the pixel values without any transformation.

## 1.6.3 Transform domain methods

Various transforms are applied to remove the speckle noise from ultrasound images of kidney.

### *Wavelet transform*

Wavelet represents a mathematical function. It decomposes a wave signal into different signal components. Every component has a frequency range and it is analyzed by using its matching resolution. Wavelet transforms have various applications like compression, data transfer, image smoothing, etc. Denoising of the image is on the basis of thresholding of wavelet coefficients.

The wavelet transform is applied to perform the multi-resolution analysis. The image is decomposed into four frequency "subbands" namely, horizontal, vertical, diagonal and approximate bands. Despeckling is performed by computing the local statistical features in these subbands. One of the virtues of wavelet transform in noise removal is lossless, produced during reconstruction of output image after denoising (Hiremath P. S., Prema T. Akkasaligar and Sharan Badiger, 2010). Soft thresholding is applied on coefficients obtained after the discrete wavelet transform (DWT). Soft thresholding has more benefits than hard thresholding such as: It prevents discontinuities and good at recovering the images as it prevents fast- sharper alterations, unlike hard thresholding. Soft thresholding has comparatively good stability.

*Contourlet transform*

Contourlet transforms are very effective in smoothening of the ultrasound image contours. It is performed in two stages as discussed in (Hiremath P. S., Prema T. Akkasaligar and Sharan Badiger, 2011). In the first stage, Laplacian pyramid(LP) decomposition is applied for capturing of discontinuous points. In step two, the directional filters bank is used for connecting the points of discontinuities to construct an undeviating the arrangement of points. Inverse contourlet transform is carried out to obtain the despeckled image.

The despeckled images are contrast enhanced further using histogram equalization.

## 1.6.4 Contrast enhancement

The resultant images of despeckling are enhanced using histogram equalization. Image enhancement improves the image quality, so that the image is perceivable by human. It is effectively carried out by histogram equalization. Histogram equalization is a valuable enhancement method. In ideal cases, the continuous distribution of gray levels results into uniform histograms. Histogram graphically represents the count of intensity levels in an image. An example for original image and its histogram is shown in Fig. 1.11(a) and (b) respectively. Histogram is the basis for many spatial domain methods. Histogram equalization performs better on different image types. For a discrete image, it does not generate a uniform histogram. However, for digital images, it can spread the gray levels throughout effectively. It is a suitable method to enhance the quality of images. Therefore, it can be used efficiently for enhancement which results into a dynamic range of gray levels, leading to increase in image contrast (Agarwal T., Tiwari M., and Lamba S., 2014).

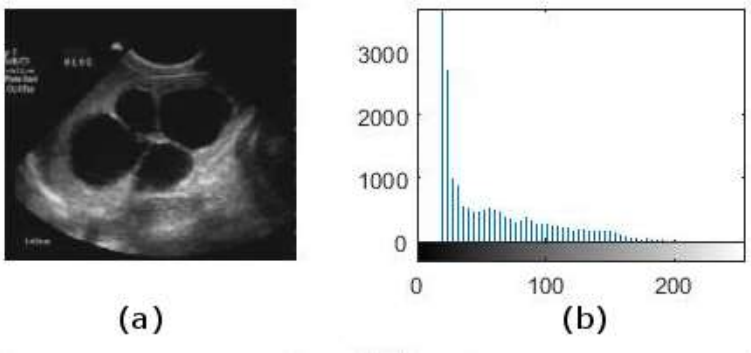


Fig. 1.11 Contrast enhancement of US image: (a) Original image (b) Histogram of original image

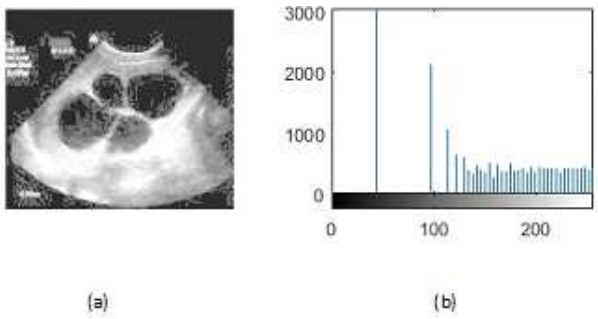


Fig.1.12 Histogram of contrast enhanced image: (a) Equalized image (b) Histogram of equalized image

Contrast enhancement is suitably used to obtain despeckled image with more image clarity. It is performed by applying histogram equalization (Agarwal T., Tiwari M., and Lamba S., 2014) on despeckled image. Contrast enhancement makes the image brighter, visualizing the edges clearly. Hence, overall image is enriched with better quality. Histogram equalized image is obtained using the Eq. (1.6.3)

$$H_k = (L-1) * P_i(r) \tag{1.6.3}$$

$N_i$ is the total number of pixels with intensity 'r' at different gray levels (0 to L-1). $P_i(r)$ is a probability density function at gray level i. It is calculated using Eq. (1.6..4)

$$P_i(r) = \sum_{j=0}^{i} N_i * \frac{1}{m*n} \tag{1.6.4}$$

The H values obtained are rounded and mapped on to despeckled image to get enhanced image with improvement in contrast. Fig. 1.12(a) shows a sample image and Fig. 1.12(b) shows histogram of equalized image.

The denoised and contrast enhanced images are used by segmentation algorithms.

## 1.6.5 Performance Evaluation

Speckle noise inhibits the major details in the ultrasound image. So, removal of speckle noise enhances the visual perception for evaluation by medical experts. It is necessary to improve the image quality for segmentation of US images further. Various evaluation parameters like Mean Square Error(MSE), Peak Signal to Noise Ratio(PSNR) and Correlation Coefficient(CC) are used (Loizou C.P. et al., 2006). These parameters are computed using the acquired input image (I) and the despeckled image (S) as follows.

*Mean Squared Error:* The MSE computes variation in quality between the acquired input image (I) and despeckled image (S) of size M×M . It is calculated as in Eq. (1.6.5).

$$\mathrm{MSE} = \frac{1}{M^2}\sum_{i,j=0}^{M-1}(I_{i,j} - S_{i,j})^2 \tag{1.6.5}$$

The MSE is used extensively to quantify the image quality. But, MSE alone is not capable to measure the perceptual. So, it is often used with other parameters.

*Peak Signal-to-Noise Ratio:* The PSNR is defined as the ratio between the highest intensity of image and the intensity of noise, which affects the images representation. It is expressed as in Eq. (1.6.6).

$$\mathrm{PSNR} = 10.\log_{10}\frac{\max_I^2}{\mathrm{MSE}} \tag{1.6.6}$$

*Correlation Coefficient:* The CC is the strength and direction of a linear relation between image samples. Pearson's CC is computed by the ratio of the product of standard deviations of two images and their covariance. The CC is expressed as in Eq. (1.6.7)

$$\mathrm{CC} = \frac{M^2\sum I_{ij}\,S_{ij} - \sum I_{ij}\sum S_{ij}}{\sqrt{M^2\sum {I_{ij}}^2 - (\sum I_{ij})^2}\sqrt{M^2\sum {S_{ij}}^2 - (\sum S_{ij})^2}} \tag{1.6.7}$$

## 1.7 Segmentation

Segmentation mainly aims at dividing an image into connected regions. The production of regions is emphasized as the pre-stage of classification. Image segmentation is a partitioning of an image into regions that are meaningful for a specific task. It is one of the initial steps leading to image analysis and interpretation. The result of segmentation is always on the regional level of abstraction. It can be used to focus on the most common application of medical imaging, namely, the discrimination between healthy anatomical structures and pathological tissues.

Image segmentation approaches can be classified according to the features and the type of techniques used. Features include pixel intensities, edge information, and texture, etc. The task of the classification step is to assign all connected regions, which are obtained from the

segmentation to a particular specified class of object. Various algorithms are implemented for segmentation of ultrasound images of kidney.

### 1.7.1 Active contour model

The active contour model is a segmentation method used to extract the region of interest (ROI) of the medical images. Based on energy gradients and forces of the medical image, ROI is segmented. The pixels of the medical image, which contain the disease, related

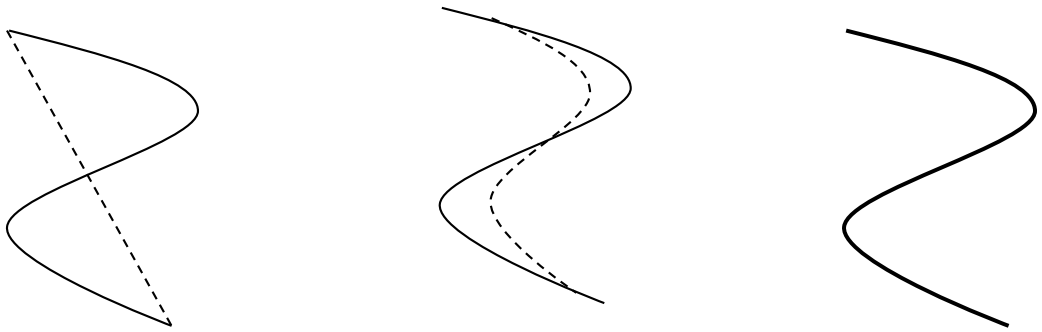


Fig. 1.13. Different stages of active contour deformation: (a) Initial contour (b) Intermediate deformation (c) Final deformation

information, is extracted to form a contour. An initial contour is specified for ACM as shown in Fig. 1.13(a). The dotted line is the initial contour for the desired curve in solid line to be segmented. The desired contour depends on the energy minimizing function. An intermediate deformation of initial contour is shown in Fig. 1.13(b). The final deformed contour is merged with actually desired contour as shown in Fig. 1.13(c). For an image I in domain Ω, the C-V model (Chan T and Vase L., 2001) is expressed by the energy minimizing function as specified in Eq. (1.7.1).

$$E^{cv} = \lambda_1 \int \text{interior}(A)|I(u) - A_1|du + \lambda_2 \int \text{exterior}(N)|I(u) - A_2|du|, u\epsilon\Omega \qquad (1.7.1)$$

The constants $A_1$ and $A_2$ are the average intensities in the interior and exterior of the contours. It is assumed as in Eq. (1.7.2), Eq. (1.7.3) and Eq. (1.7.4) respectively. The constants $A_1$ and $A_2$ are expressed as in Eq. (1.7.5) and Eq. (1.7.6).

$$A = \{u \epsilon \Omega : \Phi(u) = 0\} \tag{1.7.2}$$

$$\text{Interior}(A) = \{u \epsilon \Omega : \Phi(u) > 0\} \tag{1.7.3}$$

$$\text{Exterior}(A) = \{u \epsilon \Omega : \Phi(u) < 0\} \tag{1.7.4}$$

$$A_1(\phi) = \frac{\int_\Omega I(x,y).H(\phi(x,y))dxdy}{\int_\Omega H(\phi(x,y)dxdy} \tag{1.7.5}$$

$$A_2(\phi) = \frac{\int_\Omega I(x,y).H\left(1-(\phi(x,y))\right)dxdy}{\int_\Omega H\left(1-(\phi(x,y))\right)dxdy} \tag{1.7.6}$$

## 1.7.2 Gradient vector force method

The gradient vector force is an updated version of active contour. The gradient vector force is used for boundary extraction from the medical image by computing the diffusion of the gradient vector. It differs basically from ancient snake external forces as it cannot consider the negative gradient of a potential function, and the corresponding snake is formulated directly from a force balance condition rather than a variation in formulation. GVF has a large capture range and is able to move the snakes into boundary concavities. It does not cause blurring of the edges, unlike other methods.

GVF field can capture a snake from a long range and can force it into concave regions. Fig. 1.14(a) shows the actual ROI to be segmented. Fig. 1.14(b) and (c) show the convergence of GVF snake to the concave boundary of ROI to be segmented. The intermediate deformations are well represented in Fig. 1.14(b). We start defining an edge map f(x, y) derived from the image I(x, y) having the property that it is larger near the image edges using GVF external force $E_{GVF}$ as in Eq. (1.7.7).

$$f(x,y) = -E^{j}_{GVF}(x,y) \tag{1.7.7}$$
$$\text{for, } j = 1, 2, 3, 4$$

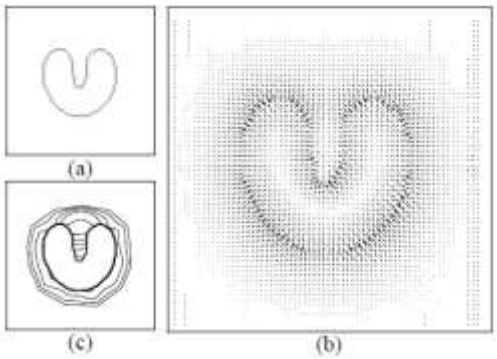


Fig. 1.14 Movement of snake into the concave boundary region using GVF external force: (a)Object to be segmented (b) Deformation of GVF snake at different iterations (c) Deformation of contour to a concave boundary

In general, the field ∇f has vectors pointing toward the edges, but it has a narrow capture range. Furthermore, in homogeneous regions, I(x, y) is constant, ∇f is zero, and therefore no information about nearby or distant edges is available. GVF is an external force vector field represented as (u(x,y), v(x, y)). The GVF is constructed by diffusing the edge force and is achieved by minimizing the energy functional which is given by Eq. (1.7.8)

$$E_{GVF} = \int\int \mu(u_x^2 + u_y^2 + v_x^2 + v_y^2) + |\nabla f|^2 |\mathbf{v} - \nabla f|^2 dxdy \tag{1.7.8}$$

where $\mu$ is a smoothing term of field (u, v). $\mu$ balances the weight of first and second terms, the subscripts indicate directional partial derivatives. This can be obtained by using Euler Eqs. (1.7.9) and (1.7.10).

$$\mu\nabla^2 u - \left(u - \frac{\partial}{\partial x}F_{ext}\right)\left(\frac{\partial}{\partial x}F_{ext}(x,y)^2 + \frac{\partial}{\partial y}F_{ext}(x,y)^2\right) = 0 \tag{1.7.9}$$

$$\mu\nabla^2 v - \left(v - \frac{\partial}{\partial y}F_{ext}\right)\left(\frac{\partial}{\partial x}F_{ext}(x,y)^2 + \frac{\partial}{\partial y}F_{ext}(x,y)^2\right) = 0 \tag{1.7.10}$$

$\nabla^2$ is the Laplacian operator. The Laplacian operator can be solved through iteration towards a steady-state value using Eqs. (1.7.11) and (1.7.12).

$$u_{i+1} = u_i + \mu\nabla^2 u_i - \left(u_i - \frac{\partial}{\partial x}F_{ext}\right)\left(\frac{\partial}{\partial x}F_{ext}(x,y)^2 + \frac{\partial}{\partial y}F_{ext}(x,y)^2\right) \tag{1.7.11}$$

$$v_{i+1} = v_i + \mu\nabla^2 v_i - \left(v_i - \frac{\partial}{\partial y}F_{ext}\right)\left(\frac{\partial}{\partial x}F_{ext}(x,y)^2 + \frac{\partial}{\partial y}F_{ext}(x,y)^2\right) \quad (1.7.12)$$

This result replaces the default external force used in active contour by GVF force. We have applied gradient vector force method for segmentation of kidney region in medical US images of kidney. It is necessary to specify initial parameter for the deforming balloon. After the deformation, initialized balloon will fit in to actual boundary of the object.

### 1.7.3 Morphological operations used for segmentation

The morphological operation is based on structuring element. The structuring element is applied throughout the image to get output image of the same size. The structuring elements of different shapes are available like diamond shaped, square shaped, etc. Various morphological operations used are erosion, dilation, opening and closing. The erosion operation shrinks the image size by removing boundary pixels. The dilation operation expands the image size by adding pixels. The adding and removing of pixels depends on the structuring element. The opening operation smoothens the outline of an object and removes thin lumps in the image. The closing smoothens the object outline but fuses narrow breaks eliminates holes and helpful in filling gaps in the contour. The morphological operations are used to segment the medical image for analysis and investigation of diseases.

Two important morphological operations that we have used are morphological opening and closing. The opening is used to smooth the contour of an object. It eliminates the thin protrusions in the image. The closing smoothens the object contour but fuses narrow breaks, eliminates holes and helpful in filling gaps in the contour (Sonka Milan, Hlavac Vaclav and Boyle Roger, 2013). The morphological opening of I by structuring element Q is given by I∘Q and is defined as in Eq. (1.7.13).

$$I \circ Q = (I \ominus Q) \oplus Q \quad (1.7.13)$$

Where, $\ominus$ indicates erosion and $\oplus$ indicates dilation. Closing of I by structuring element Q

is defined as in Eq. (1.7.14).

$$I \,.\, Q = (I \oplus Q) \ominus Q \tag{1.7.14}$$

Erosion leads to shrinking of objects. i.e., image details smaller than structuring elements are filtered out from the image (Sonka Milan, Hlavac Vaclav and Boyle Roger, 2013). Let E be a Euclidean space or an integer grid. Erosion of I by structuring element Q is the set of all points z such that Q, translated by z, is contained in I. It is given in Eq. (1.7.15).

$$I \ominus Q = \{z \epsilon E | Qz \subseteq I\} \tag{1.7.15}$$

Where Qz is the translation of Q by the vector z.

Dilation thickens the object contour. Thickening is controlled by a structuring element. Dilation is based on reflecting Q about its origin and shifting this reflection by q. It is expressed as in Eq. (1.7.16).

$$I \oplus Q = \bigcup_{q \in Q} I_q \tag{1.7.16}$$

These morphological operations are effectively used in finding the initial approximate contours for segmentation algorithms.

### 1.7.4 Level set segmentation

The level set method is used for the analysis of surfaces and shapes. The basic idea is to represent the curves or surfaces as the zero level set of a higher dimensional hyper-surface as shown in Fig. 1.15. The level set method as mentioned by Osher and Sethian takes the original front shown in Fig. 1.15 (a) and develops it into a surface shown in Fig. 1.15 (b). The cone-shaped surface intersects the X-Y plane exactly where the curve sits. The cone surface is called the level set function, as it accepts any point in the plane as input and returns back its height as output. The zero level set is so called because it is the assembly of all points at height zero. The zero level set for the boundary is set as curve. Based on the boundary curve, the remaining region of the medical image is divided into internal region and external region. The constancy and insignificance nature of level set helps to produce

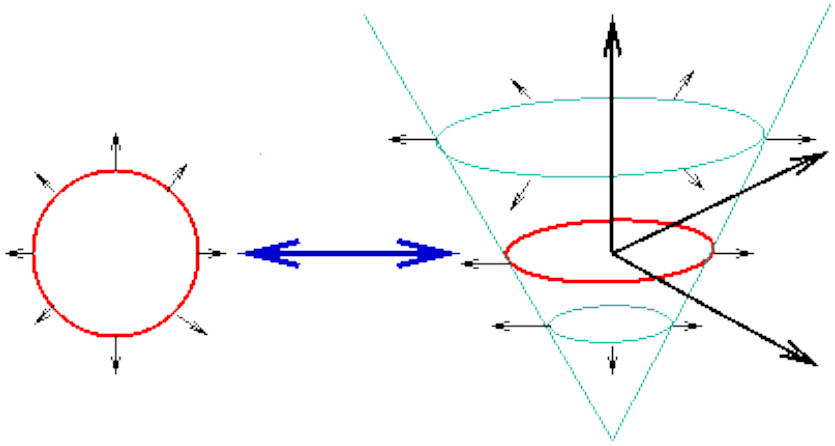

(a) (b)

Fig. 1.15. Level set working: (a) original front (b) Level set function

edge points. The edge stopping condition is dependent on the image gradient. This technique not only provides more accurate numerical implementations but handles the topological change very easily.

### 1.7.5 Performance evaluation of segmentation algorithms

Segmentation algorithms are evaluated using parameters like Dice similarity coefficient (DC) and Jaccard coefficient (JC) (J.K. Udupa and V.R. LeBlanc, 2002; Candemir S., et al.,2014). The parameters carry out a statistical evaluation by finding the overlapping accuracy of segmented image $I_1$ experimentally and manually marked image by medical expert $I_2$. DC is computed using Eq. (1.7.17) and Jaccard coefficient using Eq. (1.7.18).

$$\mathrm{DC}(I_1, I_2) = \frac{2.|I_1 \cap I_2|}{|I_1| + |I_2|} \tag{1.7.17}$$

$$\mathrm{JC} = \frac{|I_1 \cap I_2|}{|I_1 \cup I_2|} \tag{1.7.18}$$

$I_1$ is the area of the segmented region obtained by applying the segmentation algorithm and $I_2$ is an area of the region marked manually by a medical expert. The value of DC ranges from 0 to 1. For an exact match, it is 1 and 0 for no match.

Jaccard coefficient compares the similarity and dissimilarity between two images namely, $I_1$ and $I_2$. It is calculated as the intersection of the images to the union of the images. The value ranges from 0 and 1. Similar to DC, it is 1 for an exact match and 0 for the complete mismatch.

The segmentation algorithm is evaluated using the parameters such as sensitivity ($S_n$), specificity ($S_p$), and accuracy (Acc) (Mahmoud Ramze Rezaee, et al., 2000) as well. The parameters are expressed as in Eqs. (1.7.19), (1.7.20) and (1.7.21).

$$Sn = \frac{true_p}{true_p + false_n} \tag{1.7.19}$$

$$Sp = \frac{true_n}{true_n + false_p} \tag{1.7.20}$$

$$Acc = \frac{true_p + true_n}{true_p + true_n + false_p + false_n} \tag{1.7.21}$$

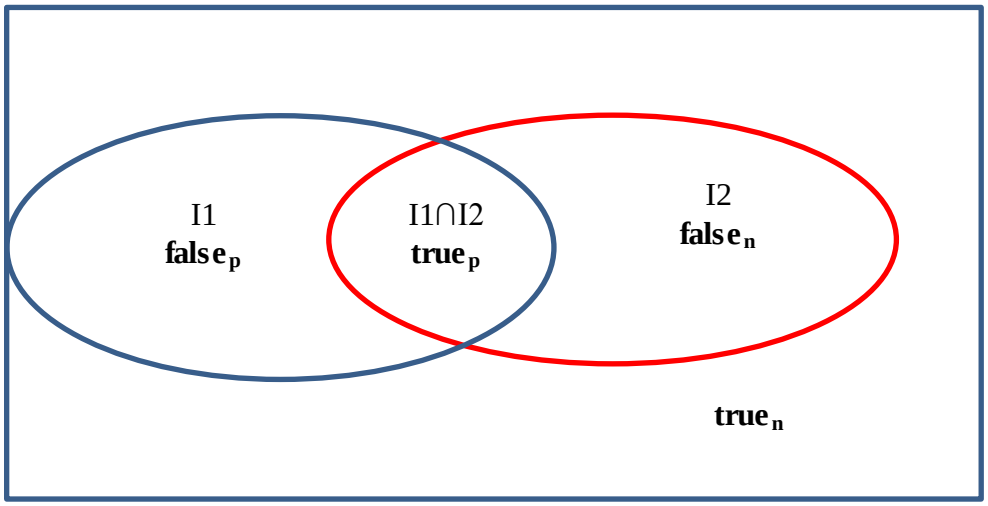


Fig. 1.16. Venn diagram for representation of $true_p$, $true_n$, $false_p$ and $false_n$

Fig. 1.16 shows the representation of $true_p$, $true_n$, $false_p$ and $false_n$ . $I_1$ is the segmented region obtained by applying the segmentation algorithm and $I_2$ is the region annotated manually by a medical expert.

$true_{p,}$ true positive is computed by finding the intersection of the segmented image and the marked image by a medical expert. The false positive, $false_p$ is the incorrectly segmented image with non-matching ROI in the ground truth image obtained by a medical expert. The false negative, $false_n$, is the missed region in the ground truth. The true negative, $true_n$ is the part of the image beyond the union of segmented image and ground truth. The values of these parameters lie within the range from 0 to 1. The value 1 shows the exact segmentation.

Mean and standard deviation of performance parameters are considered for the comparison of different segmentation methods. Mean is computed as an average value of all the values under consideration. Standard deviation is a measure of the amount of variation or dispersion around the mean. It is useful in finding the spread out over a dataset.

## 1.8 Feature extraction

After segmentation in a medical image, the required features contain information helpful to analyze and diagnose. The features are the characteristics of the medical image and are required to extract relevant maximum characteristics for analysis. Instead of taking the whole medical image, selected features that offer the information required for analysis are selected. The big challenge is detecting the features containing the needed detail information, selecting those features and extracting it for further processing. Several methods are available for feature extraction as discussed below.

### 1.8.1. Haralick features

Gray level co-occurrence matrix (GLCM) based features are also termed as Haralick features. The working of Haralick feature extraction is done in two major steps. Computation of GLCM is the initial step, followed by the extraction of texture features on the obtained GLCM. The GLCM is used to measure co-occurrence of relation between the adjacent pixels based on pixel positions. GLCM computes the probability of gray level distribution by considering a pair of adjacent pixels. The GLCM extracts the features based on pixel positions with similar gray level values. Various GLCM texture features like energy homogeneity, contrast and correlation can be calculated by using Eqs. (1.8.1), (1.8.2), (1.8.3) and (1.8.4) respectively.

$$\mu = \sum_{x,y} xI(x, y) \tag{1.8.1}$$

$$\sigma = \sum_{x, y} (x - \mu)^2 I(x, y) \tag{1.8.2}$$

$$\text{Contrast} = \sum_{xy} | x - y |^2 I(x, y) \tag{1.8.3}$$

$$\text{Correlation} = \sum_{xy} \frac{(x - \mu)(y - \mu)I(x, y)}{\sigma^2} \tag{1.8.4}$$

Where, $\mu$ = weighted avg. of pixel and $\sigma$ = weighted variance of pixel.

## 1.8.2. Shape-based features

Images are represented by different forms that explain the object shape and size. Different shape feature descriptors namely, area, perimeter, diameter, orientation, eccentricity, major and minor axis length are used effectively for image analysis and classification.

*Area*: It is the total number of pixels (P) covering the segmented kidney stone or cystic region and is calculated as in Eq. (1.8.5)

$$\text{Area} = \sum_{i=1}^{n} \sum_{j=1}^{m} P(i, j) \tag{1.8.5}$$

*Major axis length:* It is obtained by the diameter of the largest circle circumscribed by the segmented stone or cystic region and is shown as in Eq. (1.8.6).

$$\text{Maj\_axis} = \sqrt{(m_1 - m_2)^2 + (n_1 - n_2)^2} \tag{1.8.6}$$

*Minor axis length:* It is obtained by the diameter of the smallest circle circumscribed by the segmented stone or cystic region and is shown as in Eq. (1.8.7).

$$\text{Min\_axis} = \sqrt{(m_2 - m_1)^2 + (n_2 - n_1)^2} \tag{1.8.7}$$

In Eq. (1.8.6) and Eq. (1.8.7), $(m_1,n_1)$ and $(m_2,n_2)$ are the end points of the axes.

*Eccentricity:* Eccentricity is defined by the ratio between major axis length and minor axis length. It is expressed as in Eq. (1.8.8).

$$\text{Eccentricity} = \frac{\text{Maj\_axis}}{\text{Min\_axis}} \tag{1.8.8}$$

*Orientation:* It is a scalar value that represents the angle between the horizontal axis and the major axis of the diseased kidney region.

### 1.8.3 Wavelet transform based features

In wavelet transform method, the medical image is converted into new form using frequency properties of gray-level distribution. The wavelet is a function that divides the continuous waves into various scale components. The scales are processed simultaneously in time and in frequency domain. The wavelet transform is based on windowing techniques of varying sizes. The long term intervals are used to extract low frequency features and short term intervals are used to extract high frequency features.

Wavelet considers both time and frequency domain knowledge of the image. Wavelet transform can be effectively used in image processing for various applications such as compression, image analysis, speckle noise removal of medical images (Hiremath P. S., Prema T. Akkasaligar and Sharan Badiger, 2010).

In wavelet decomposition, a 2D image is decomposed into four frequency sub-bands, namely, the LL, HL, LH and HH bands as shown in Fig. 1.17 (a). H symbolizes high pass filter and L indicates low pass filter. LL is obtained by applying a low pass filter for both horizontal and vertical directions. LH is obtained by applying a low pass filter for horizontal and high pass filter for vertical directions. HL is obtained by applying a high pass filter for horizontal and low pass filter for vertical directions. HH is obtained by applying a high pass filter for both horizontal and vertical directions. In higher decomposition levels, LL subband

alone is taken for further subdivision because, it represents the approximate coefficients. The decomposition at level 3 is shown in Fig. 1.17(b). An example for level 1 wavelet decomposition of a ultrasound image of kidney is shown in Fig. 1.17(c). Energy feature obtained at horizontal, vertical, and diagonal subbands are considered as features for classification of diseased ultrasound images of kidney.

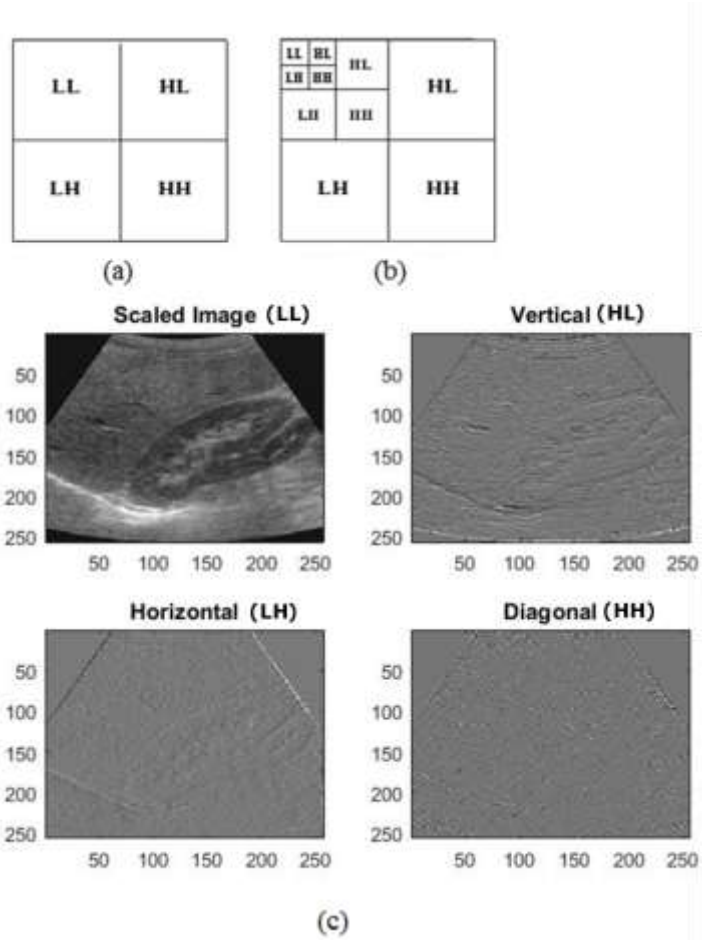


Fig. 1.17. Wavelet decomposition: (a) Level 1 decomposition (b) Level 3 decomposition (c) Level 1 decomposition of a sample US image of kidney

Various wavelet families are available like Daubechies, discrete symlets, biorthogonal, reverse biorthogonal, Meyer, and coiflets.

## 1.8.4 Tamura features

Tamura features work on the visual perception of humans. They contribute potentially for representation of image. The computed features take into account of variation between the

average signals for the non-overlapping windows of various sizes. The three common features of Tamura are coarseness, contrast and direction.

- *Coarseness:* It is the measure significant spatial variation of grey levels. In other words, it refers to the size of the significant pixels framing the texture.

- *Contrast:* It is a measure of grey level distribution in the image and the extent to which the gray levels are biased towards black or white.

- *Direction:* Direction is a measurement of the frequency distributions of oriented edges versus their directional angle.

### 1.8.5 Histogram of Oriented Gradient (HOG) features

The HOG feature set is used for object detection in image classification. It considers the number of occurrences of gradient orientation in region of interest (ROI). To find HOG features, the image is divided into small connected regions called as cells. A histogram of gradient directions is computed for all the pixels within each cell. The HOG descriptor is computed by concatenating these histograms. To improve the accuracy, the local histograms are contrast-normalized by computing a measure of the intensity across a larger region of the image called a block. Then these values are used to normalize all cells within the block. This normalization results in better invariance to the changes in illumination and shadowing.

## 1.9 Classification

The classification is the process of classifying the medical images as normal or abnormal images based on features extracted. Several classification methods are available to classify the extracted feature sets.

### 1.9.1. Support Vector Machine (SVM)

The SVM is a supervised machine learning algorithm or discriminative classifier used to separate the hyperplane. The hyperplanes are decision boundaries which help to classify the data. The data falling on either side of the hyperplane is categorized into different classes. Based on a number of input features the dimension of the hyperplane varies (M. B.

Subramanya, S.Mukherjee and M. Saini, 2015). The SVM training algorithm is used to build a model that categorizes the data set into two or more categories. The SVM creates a hyper-plane to increase the margin between different categories as shown in Fig. 1.18. The labled training data belongs to one category and remaining data in other categories.

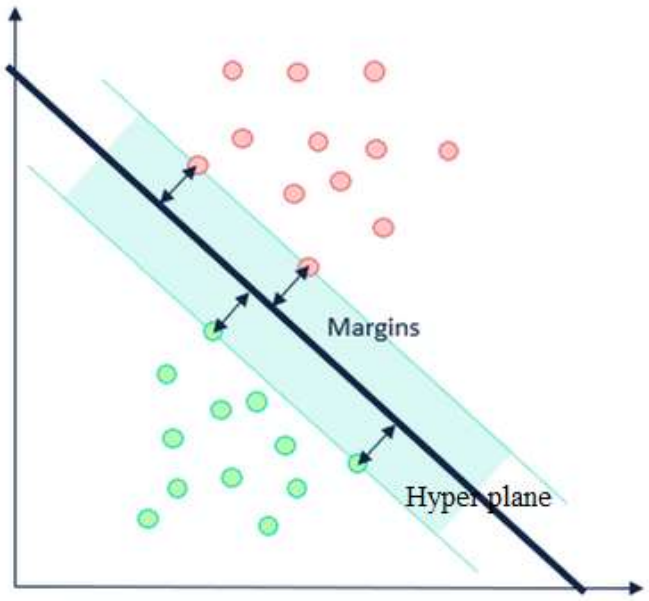


Fig. 1.18. Working of support vector machine

## 1.9.2. K-Nearest Neighbors (k-NN)

The k-NN is a simple, easy-to-implement and non-parametric supervised learning algorithm. It is used as a classifier. In a supervised learning algorithm, the labeled training sets are used during the training phase. In testing phase, non-labeled data sets are used to analyze and recognize the label for data sets based on trained labeled data sets. The k-NN classifier uses k-nearest trained data set to test non-labeled data set and recognizes the similarities based on major votes to a class label. The output of the classifier is a class member. The entire training sets are used during the testing phase.

The working of k-NN is explained in the Fig. 1.19. The example considers k=3 for finding the class of green dot. As shown, the 3 nearest objects are selected, based on majority vote the object is classified to the category of red triangle.

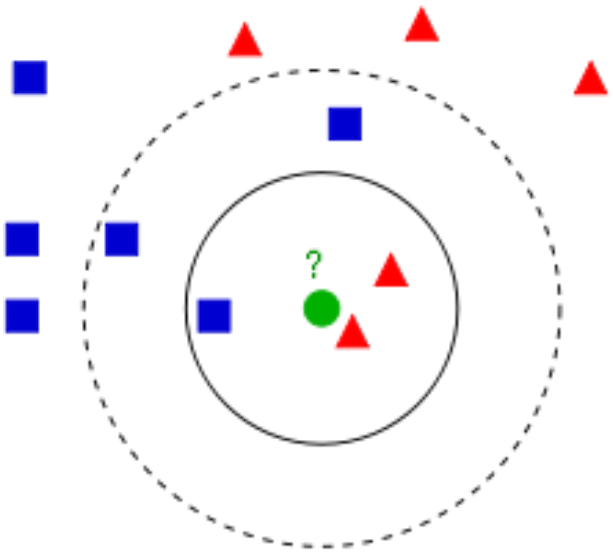


Fig. 1.19. Working of k-NN classifier

For the n classes, $c_1$, $c_2$, $c_3$, …, $c_n$, and the unknown sample T, the k-NN judge that the majority vote for k nearest neighbors belongingness to one class using the Eucledian distance. The decision function (S. Manish, 2007) is as in Eq. (1.12.1). We have used a classifier with the class labels as normal class, stone and a cystic ultrasound image of kidney.

$$Di\,(T) = \max\,(k_i) \qquad (1.12.1)$$

for i=1,2….n.

## 1.9.3. Fuzzy K-Nearest Neighbors (Fuzzy k-NN)

The fuzzy k-NN classifier is more suitable to classify explicit or undefined data sets with assumptions that, the data set belongs to all classes with different degree of membership. In fuzzy k-NN, all unlabeled test data sets are analyzed and assigned to the nearest trained class labels with full membership of degree one. If the test data set is not close to any class labels, then such data sets are assigned to all class labels with different degree of membership. The main goal of the classifier is to build the trained data set, which is used for prediction.

In case of fuzzy k-NN, the decision of class is made by using the relation between distance and similarity. The distance between T and $C_i$ can be shown as in Eq. (1.9.2).

$$\text{dist}\ (T,C_i) = 1\text{-sim}(T,\ C_i) \tag{1.9.2}$$

Where sim(T, $C_i$) denotes the similarity between training image set and testing image. K-nearest neighbors' known samples {Ti, 1, 2, k} of the classifying sample T, are computed as the members of a sample T to each class as specified (S. Manish, 2007) in Eq. (1.9.3).

$$\mu_j(T) = \frac{\sum_{i=1}^{k} \mu_j(T_i)\ \text{sim}(T,T_i)\frac{1}{\left(1-\text{sim}(T,T_i)\right)^{2/(b-1)}}}{\sum_{i=1}^{k}\frac{1}{\left(1-\text{sim}(T,T_i)\right)^{2/(b-1)}}} \tag{1.9.3}$$

## 1.10 Motivation

Ultrasound image segmentation is strongly influenced by the quality of the input images. There are characteristic artifacts which make the segmentation task complicated such as attenuation, speckle, shadows and signal dropout; due to the orientation dependence of acquisition that can result in missing boundaries. Segmentation and classification of kidney in medical ultrasound images is a challenging task.

Most of the work done so far mainly focuses on segmenting the required organ in US images. The motivation of study is to segment the diseased part of the kidney such as cyst or stone rather than an entire organ. Further, the classification of the input ultrasound image of kidney into normal and abnormal (cystic or stone) image followed by the appropriate analysis is crucial information for the medical experts. Presently, the diagnosis is subjective and time-consuming process. Hence, computerized medical applications are gaining more popularity in assisting the clinicians for diagnosis of the diseases.

## 1.11 Objectives of the study

The primary aim of the work is to detect, segment and analyze the cysts and stones in ultrasound images of kidney. Ultrasound images of normal kidney, cystic and kidney stone are considered for the research work. In the proposed work, different methods for speckle noise removal, segmentation and classification algorithms are experimented. The main aim of the research work includes the design and development of efficient methods for automatic ROI generation, analysis and recognition of kidney disease in medical US images namely, kidney stones and polycystic kidney disease. The objectives of the thesis are:

- To design efficient methods for the generation of the automatic initial contour of cysts and stones in the medical US image of the kidney.
- To design efficient methods for fully automated segmentation of cysts and stones in the medical US image of the kidney.
- To develop efficient methods for the extraction of optimal features from the ROI obtained and classification of kidney diseases using various classifiers.
- To identify the number of cysts and stones along with their size in the medical US image of the kidney having cysts and stones.

## 1.12 Organization of the thesis

The thesis is organized into seven chapters.

The literature review is presented in Chapter 2. In order to put the research into the context different issues are addressed in the literature. The brief review of existing works on importance of ultrasound images, denoising of ultrasound images, segmentation of kidney in ultrasound images, detection of renal calculus or kidney stone in medical images, detection of cysts in medical images of kidney, and diagnosis of other kidney diseases using ultrasound medical images are discussed.

Segmentation of normal kidney, cysts and stones using GVF method is discussed in Chapter 3. Experimentation carried out, performance evaluation of the proposed method are discussed in the chapter.

Automatic segmentation of kidney cysts using active contour model is proposed in Chapter 4. An automatic initial contour generation, avoiding the user intervention is proposed followed by cystic kidney image segmentation. The performance evaluation by medical experts and using various parameters is discussed in this chapter.

Automatic segmentation of cysts and stones using the level set method is discussed in Chapter 5. The improved performance of the level set method over GVF and ACM is shown in Chapter 5.

Chapter 6 describes feature extraction and classification of the diseases in US images of kidney. Different set of features like Haralick, wavelet, shape, Tamura and HOG features are extracted and classified using three classifiers namely, k-NN, SVM and fuzzy k-NN. Performance of the different feature sets and classifiers are evaluated.

Finally, Chapter 7 presents the conclusions of the research study undertaken herein. The contributions and limitations of the proposed work are discussed. In addition, recommendations and future directions of the present study are also presented.

# Chapter 2

# LITERATURE REVIEW

## 2.1 Introduction

The literature on computer-assisted approaches to the US kidney image analysis is scarce. The discussion on existing methods is divided into six main sections as denoising of ultrasound images, segmentation of kidney in ultrasound images, segmentation and classification of renal calculus or kidney stone in medical images, segmentation and classification of kidney cysts in medical images, and diagnosis of other kidney diseases using ultrasound medical images.

The kidney and its associated diseases are preferably evaluated by ultrasound imaging modality (O'Neill, 2014) because of the kidney's location, shape, and limited range of pathology. Additionally, US imaging is safe, easily accessible, and free from radiation effects. Because of all these virtues, US imaging is the ideal imaging modality. US imaging is considered as demonstrating high sensitivity in detecting kidney cysts. Hence, it is widely used in the diagnosis and progression monitoring of PKD (Gradzik M. et al., 2016). US imaging is a good diagnostic tool for CKD (Lucisano, G. et al., 2015). The measurements like pole-to-pole length, width, and thickness obtained by sonography are correlated with kidney functions and helpful for the diagnosis of CKD. The parameters like kidney size obtained by US imaging are correlated with the functionality of the organ such as the filtration rate of glomeruli (Adibi A., Adibi I. and Khosravi P., 2007). Glomerular filtration is the major functionality of the kidney. Thus the sonographic parameters obtained can be used to predict kidney functionality and abnormality.

US imaging is a vital tool for diagnosis. It provides the internal structure of the body to eventually diagnose the diseases or abnormal tissues. US images have many advantages. They are non-invasive, non-harmful, portable, accurate, and cost-effective. Because of these characteristics, US images are the most dominant diagnostic tools. However, the quality of US images is poorer. It is due to many reasons, like the noise introduced during the process of image acquisition and defectiveness in the imaging system. So, in recent years extensive

work is carried out in this direction to resolve the issues associated with speckle-noise in US images.

In Chapter 1, a general perspective of the concepts related to the research is discussed. A comprehensive literature survey related to the research work is presented in this chapter.

## 2.2 Denoising of ultrasound images

B-mode US images are characterized by the speckle artifact. It introduces tiny false structures in the images, disguising the true tissue boundaries. The speckle enforces difficulty for a human to discriminate between pathological tissue/organ in diagnostic examinations and the speckle noise. The speckle exists as a result of overlaps between the echoes. It is generated because of two signals are caught in identical environments, experiencing similar speckle artifact (C.B. Burckhardt, 1978; P.N.T Wells and M. Halliwell, 1981; Bamber J. C. and C. Daft, 1986).

Speckle noise uses a phenomenon of acquiring the images based on signal interferences that are emanated from heterogeneities of the objects under study. The superposing acoustic waves with random phases and amplitudes tend to create convoluted interference patterns, leading to speckle noise. US images are more prone to speckle noise. Speckle noise reduces image contrast. It leads to ambiguity and image blurring. Further, it decreases the quality and consistency of medical ultrasound image. Hence, various methods for suppressing the speckle noise are proven to be essential. Enhancement of image quality improves the diagnostic perspective of US images.

Speckle noise impurity is very common in US images. The noise in the ultrasound image appears because of many causes. Surrounding tissues, fatty content and respiratory moments are some reasons for noise. The noise may have a bad effect on the segmentation or classification of organs (S. D. Chen and A. Ramli, 2003). Noise in ultrasound images leads to poorer resolution and low image quality. Noise level is higher in ultrasound images than the other imaging modalities like X-ray, CT, and MRI. Apart from speckle noise in US images, several other errors are made during image acquisition. In (Andrzej Paweł Wieczorek, Magdalena Maria Woźniak, Janusz F. Tyloch, 2013), authors have illustrated about the most common errors committed during the US diagnosis of the urinary system. The common

errors appear mainly because of inappropriate techniques of US imaging or inaccurate interpretation. These errors arise due to inexperienced sonographers, inadequate scanning machine, and insufficient knowledge about operating the machine, and the lack of patient support during the scanning. These errors may lead to poor quality of the image and wrong diagnosis in turn.

The interpretation of kidney boundary is difficult for visual inspection by the experts when the speckle noise becomes apparent. In (Hiremath P. S., Prema T. Akkasaligar and Sharan Badiger, 2009; Hiremath P. S., Prema T. Akkasaligar and Sharan Badiger, 2013; T. Joel and R. Sivakumar, 2013), authors have discussed the methods for despeckling medical US images. In (Gonzalez R. C. and Woods R. E., 2002), the authors have discussed the various despeckling techniques in image processing. Spatial filtering methods like mean filter, median filter, Frost filter, Lee filter, etc. are discussed. Several multi-scale methods based on wavelet, curvelet, and contourlet have been discussed. So, the despeckling of ultrasound images is an essential preprocessing step. Noise must be carefully eliminated without affecting the major features of the input image.

(Si Wang et al., 2017) have discussed a despeckling method using total variations of first and second order. The method uses an edge-preserving feature which is very essential in further stages of segmentation and analysis. The negative effects of speckle noise in US images are eliminated by (Shan Gai et al., 2018). They have used a monogenic wavelet transform with the Bayesian framework. The monogenic coefficients are separated as noisy and noiseless signals using Laplace mixture and Rayleigh distributions respectively. In (Yingyue Zhou et al., 2019), authors have presented an iterative speckle filtering technique using Bayesian non-local means filter (BNLMF). The technique makes use of a key probability density function. The noisy image is passed through multiple iterations of the filter.

The wavelet transform is applied to perform the multi-resolution analysis. The image is decomposed into four frequency “subbands” namely, horizontal, vertical, diagonal, and approximate bands. Despeckling is performed by computing the local statistical features in these subbands. One of the virtues of wavelet transform in noise removal is a lossless resultant image, produced during the reconstruction of output image after denoising (Hiremath P. S., Prema T. Akkasaligar, and Sharan Badiger, 2010). Soft thresholding is applied to coefficients obtained after the discrete wavelet transform (DWT). Soft

thresholding has more benefits than hard thresholding such as: It prevents discontinuities and good at recovering the images as it prevents fast- sharper alterations. Soft thresholding has comparatively good stability.

Contourlet transform is very effective in smoothening of the ultrasound image contours. It is performed in two stages as discussed in (Hiremath et al., 2009; Hiremath P. S., Prema T. Akkasaligar, and Sharan Badiger, 2011). In the first stage, the Laplacian pyramid(LP) decomposition is applied for capturing of discontinuous points. In step two, the directional filters bank is used for connecting the points of discontinuities to construct an undeviating the arrangement of points. Inverse contourlet transform is carried out to obtain the despeckled image. As contourlet transform performs better in noise removal, denoising is performed in the proposed work using contourlet transform before segmentation.

## 2.3 Segmentation of kidney in ultrasound images

In (Wan M. Hafizah and Eko Supriyanto, 2012), authors have proposed an algorithm for segmentation of the region of interest (ROI) in renal ultrasound images. Firstly, the speckle noise reduction is carried out using a median filter, Wiener filter, and Gaussian low-pass filter. Then texture analysis is performed by computing the local entropy of the image. This is followed by the threshold selection, morphological operations, object windowing, determination of seed point, and the ROI generation. The initial seed point is determined with the assumption of the kidney always lies in the center of the US image. However, the location of the kidney in the US image may not lie in the center for all views of kidney US images. In (Xie J., Jiang Y. and Tsui H., 2005), authors have discussed the texture feature extraction by using a bank of Gabor filters on test image through a two-sided convolution strategy. The texture model is created by approximating the parameters of a set of half-planed Gaussians using the expectation-maximization method. Further, the texture similarities of areas around the segmenting curve are identified as the inside and outside regions. A method based on the scale-space representation of the assessment of multi-scale differential principal curvature features is proposed in (Raja, K. B., Madheswaran M. and Thyagaraja, K., 2000). It can be used to determine the extent of isolation between the features of different kidney types. In (Ashish K. Rudra, et al., 2013), authors have proposed a kidney segmentation algorithm using graph cuts and pixel connectivity. A connectivity term

is introduced in the energy function of the standard graph cut via pixel labeling. Each pixel is assigned a different label based on its probabilities to belong to two different segmentation classes. The labeling process is articulated according to Dijkstra's shortest path algorithm. In (Carlos S., et al., 2013), authors have used an active shape model, based on a covariance matrix adaptation assessment strategy. The genetic algorithm optimizes the posture and main shape variation models of the kidney shape model, resulting in the segmentation of the kidney.

In (K. Bommannna Raja, et al., 2006), authors have discussed a higher-order spline interpolated contour obtained through homogenously distributed coordinates for segmentation of the kidney region into different classes. In (Chia- Hsiang Wu and Yung-Nien Sun, 2006), authors have used the Laws' microtexture energies and maximum a posteriori (MAP) estimation to build a probabilistic deformable method for kidney segmentation. Using texture image features and MAP estimation, each image pixel is categorized as inside or outside the periphery. Texture and shape prioris based method is used for kidney segmentation in ultrasound images. In (J. Alison Noble and Djamal Boukerroui, 2006; K. M. Meiburger, U. R. Acharya and F. Molinari, 2018), authors have conferred reviews on ultrasound segmentation methods in detail. Mainly they focused on techniques developed for medical B-mode ultrasound images. Authors have discussed a review of articles by clinical application to highlight the methods that have been investigated and the process of validation that has been done in different clinical domains. They have presented different classification methodologies in terms of the use of shape prior information.

In (Wan M. Hafizah and Eko Supriyanto, 2012), authors have applied rotation to the kidney region in the US image for the images of different orientations and then texture feature analysis is done. In (Arpana M. Kop and Ravindra Hegadi,2010), authors have computed an external force called gradient vector force to avoid poor convergence to concave boundaries of the snake model. In (Huang J., Yang H. and Chen Y. , Tang L.), authors have employed a parametric super-ellipse as a global prior shape for a human kidney and the Fisher-Trippet is used to describe the gray level statistics. In (Ujjwal Maulik, 2009), genetic algorithms (GAs) have been used for segmentation. The genetic algorithmic framework used is effective in segmenting noisy US images. In (Vijay Jeyakumar and M. Kathirarasi Hasmi, 2013), authors

have described a framework for evaluating ultrasound kidney image segmentation using various algorithms like edge detection, watershed segmentation, region-based segmentation, and clustering method. It has been found that the clustering method performs well among these methods.

From the literature survey on the segmentation of kidney in US images, it is observed that there is a need for research in fully automatic segmentation of kidney from US images without user intervention. Some of the methods assume a fixed elliptical shape and pre-registration of the image. It cannot work for all the new input images to be segmented. Complete automation of segmentation can be achieved through the generation of initial seed point automatically for algorithms like region growing and automatic initial contour generation for deformable methods. Further, the algorithm must work for all the views of US images of kidney like transverse view and longitudinal view.

## 2.4 Detection of renal calculus or kidney stone in medical images

In (P. R. Tamilselvi and P. Thangaraj, 2011), the author has proposed a region indicator with contour segmentation. K-means clustering is utilized to find accurate calculi from renal images. In (P. R. Tamilselvi, 2013), authors have proposed segmentation and detection of the calculi using an effective Adaptive Neuro-Fuzzy Inference System (ANFIS) approach. In (P. R. Tamilselvi and P. Thangaraj, 2011), the study presents a scheme for ultrasound kidney image diagnosis for stone and its early detection. It is based on semiautomatic seeded region growing segmentation and classification of kidney images with stone sizes. In segmented portions of the images, the intensity threshold variation is used in identifying multiple classes to classify the images as normal, an image with stone and early stone stages. In this segmentation method, the homogeneous region depends on the image granularity features, where the interesting structures with dimensions comparable to the speckle size are extracted. In (Neil R. Owen, 2006), authors have reported the calculation and measurement of shock wave scattering by stone models in water. Calculations are based on linear elastic theory to find pressure in the fluid and stress in the stone models. Further scattering theory is used to find radiation from the stone models. Measurements are made with a spherical, broadband receiver used to distinguish between fractured and intact model stones. In (Jie Wu, 2009), authors have worked on MRI images of the kidney. They have used a template-based

technique for diagnosis of kidney diseases such as tumors, cyst, and stone. In (Ranjitha M., 2016), authors have used GLCM and second-order texture features followed by k-means clustering to analyze the required features in the kidney organ. The principal component analysis is used for feature reduction.

There is a scope to develop fully automatic segmentation algorithms for medical images, particularly for US images of kidney stone. Most of the work carried out so far is lacking in image analysis of the segmented stones, to determine the size of the stone. Analysis of the segmented results has greater importance in clinical analysis for further plan of treatment by medical experts.

## 2.5 Detection of cysts in kidney images of other imaging modalities

In (Mahmoud Ramze Rezaee, 2000), an unsupervised image segmentation technique is presented, which combines pyramidal image segmentation with the fuzzy c-means clustering algorithm. Each layer of the pyramid is split into a number of regions by a root labeling technique, and then fuzzy c-means is used to merge the regions of the layer with the highest image resolution. Cluster validity functional is used to find the optimal number of objects automatically. In (Carlos Nicalou et al., 2000), authors have described the use of sonographic features from US images of kidney in differentiating the ADPKD from ARPKD. The parameters such as the number of cysts, their sizes, cortical echogenicity, etc., can distinguish ADPKD from ARPKD easily. A statistical survey of clinical data and sonographic parameters of the kidney is used by the authors for the study. In (Kanishka Sharma, et .al, 2017), automated segmentation of ADPKD kidneys, using fully convolutional neural networks is proposed on CT images. The efficiency of the developed method is measured both by quantitative and qualitative methods. In (Kyongtae T. Bae, et .al, 2014), a semi-automated method is developed to segment individual renal cysts in MR images of patients with ADPKD using image editing software.

In (Arlene B. Chapman and Wenjing Wei, 2011), authors have explained the appropriateness of using US, CT, and MRI for the detection of kidney cysts. However, CT and MRI show higher resolution and increased sensitivity for the detection of kidney cysts of diameter less

than 1cm. But, due to low-cost, no radiation and contrast exposure, US imaging is the primary choice for diagnosis of ADPKD. Both CT and MRI modalities have greater sensitivity compared to ultrasonography in the detection of cysts of smaller sizes, particularly in children as mentioned in (Nascimento A. B., 2001). Total renal volume is used as a suitable parameter for evaluating disease progression. But, for significantly enlarged kidneys, the US does not yield an accurate valuation of their sizes (Wołyniec W. et al., 2008). Hence, CT and MRI are the preferred imaging modalities for the diagnosis of cysts, of too smaller and too larger sized cyst over the US.

Most of the standard methods proposed are using cystic MRI and CT images of the kidney. The segmentation algorithms found in the literature are semi-automatic. Hence, there is a need for fully automatic segmentation algorithms on US images of kidney cysts particularly.

## 2.6 Diagnosis of other kidney diseases using medical ultrasound images

Ultrasound imaging is used in the detection of other kidney diseases like tumors in the kidney, evaluating CKD, etc. US imaging is capable of evaluating kidney tumors before the treatment. US image also has the advantage of early diagnosis of tumors (O. Helenon et al., 2001). The histopathologic property concerning the tumor size can be obtained easily. In (Xiong X. et al., 2019), authors have proposed a method for the segmentation of renal tumors in US images using adaptive sub-regional evolution level set algorithm. Radius and curvature of the convoluting initial level set function are adaptively adjusted based on internal and external gradient forces. In (Li L., Ross P., Kruusmaa M., and Zheng X., 2011), authors have shown a comparative study of various segmentation algorithms such as region-based, edge-based and texture-based algorithms for US images of renal tumors.

In (Pujari R. M., and Hajare V. D., 2014), authors have presented a method for analysis of chronic kidney disease stages in US images. Authors have used the median filter followed by manual cropping of the image. The manually segmented image is separated into four concentric rings. Based on the black to white ratio of each ring, the stage of CKD is determined. In (Chen C. et al., 2014 and Chen C. et al., 2020), authors have proposed a method using image processing and machine learning algorithms for the diagnosis of different CKD stages. Texture features and SVM classifier are used for analysis. Features to analyze brightness, area, grayscale variations are used on a preprocessed (applying median

filter) image. In (Chin-Chi Kuo, et al., 2019), authors have presented estimation of kidney function and CKD through US images using deep neural networks. For finding the glomerular filtration rate, a deep convolution neural network is used.

US images are effectively used as an efficient diagnostic tool for many kidney diseases like kidney stones, tumors, polycystic kidney disease, chronic kidney disease, etc. Thus, there is a crucial requirement for the design and development of a fully automatic computer-assisted diagnostic system for the analysis of kidney diseases.

## 2.7 Summary

The literature review in this chapter has examined the existing work, on importance of ultrasound images, denoising of ultrasound images, segmentation of kidney in ultrasound images, segmentation and classification of renal calculus or kidney stone in medical images, segmentation and classification of cysts in medical images of the kidney, and diagnosis of other kidney diseases using ultrasound medical images.

The work in recent years on ultrasound images deals with the segmentation schemes to identify the kidney boundary using various methodologies. Not much work is cited in the literature for the segmentation of diseased portions such as stone or cyst in the kidney organ. Further analysis of the segmented region like location, number of cysts/stone and size is hardly found in the existing literature. To the best of our knowledge, classification of the segmented organ as the normal and diseased organ is rarely found in the existing works. The scope exists for the automatic region of interest (ROI) generation, analysis, and recognition of kidney disease from ultrasound images of the kidney.

The literature survey indicates the necessity of further research, to develop and evaluate new computer-assisted techniques for the detection of abnormalities in the kidney. Analysis of stone and PKD in the US image is very essential in particular. Segmentation and identification of kidney cysts and stones in US images is discussed in subsequent chapters.

# Chapter 3

# GRADIENT VECTOR FORCE BASED SEGMENTATION OF KIDNEY, CYSTS AND STONES IN ULTRASOUND IMAGES OF KIDNEY

## 3.1 Introduction

Segmentation reduces the larger available information to a more focused point. However, it is a difficult task for noisy images like B-mode US images. Segmentation of images using a deformable curve is essential in medical images. The extraction of anatomic structures/tissues by segregating the original image pixels into subsets conforming to the organ/tissue is very essential and a primary stage of the medical image analysis. It is carried out through registration, labeling, and other means of user input. The manual process of segmentation is extremely labor-intensive and time-consuming. Segmentation by traditional approaches like region growing and edge detection requires some form of expert interactive inputs. The complete automation of these techniques is hard. This is because of the complexity, variations within and across the objects to be segmented. Noisy images and poor quality images with added artifacts can lead to false region segmentation or boundary cutoffs in the objects (or ROI).

The deformable spline-based segmentation algorithms can overcome the drawbacks associated with traditional image processing algorithms. The connected and contiguous representations reflect the object borders. Prior knowledge of continuity and smoothness of the deformable methods can resolve issues such as noise, gaps, and other anomalies in object boundaries. Additionally, the parameter based model representation provides a condensed, analytical narration about ROI shape. All these characteristics are leading to a vigorous and sophisticated technique. The snake model is the first and primarily used deformable method for a medical image, to extract the ROIs in two-dimensional images.

---

[1] Akkasaligar Prema T. and Biradar Sunanda, "Analysis of polycystic kidney disease in medical ultrasound images, International Journal of Medical Engineering and Informatics, vol.10 (1), pp. 49-64, 2018.

The traditional snake model has certain shortcomings like their sensitivity to the local minimum state. The performance of segmentation is dependent on the converging policy (Cohen L.D. and Cohen I., 1990). It fails in convergence to the nearest boundary. The GVF model successfully addresses the issues of the traditional model. It expands towards the boundary of a ROI when the GVF field is nearer to it. But, it changes smoothly over the consistent regions, expanding towards the ROI boundary. The field prevents a snake from expanding to an unnecessarily larger range and forces it to a concave region.

The cysts and stones in the kidney do not have a perfect geometrical shape, but resemblance to concave-shaped objects. The GVF segmentation is more suitable for concave-shaped objects and hence suitable for the segmentation of a bean-shaped kidney. The GVF algorithm is used for the effective segmentation of normal and abnormal kidney having a stone or cyst.

In the present chapter, denoising of ultrasound images of the kidney is discussed. Further, the efficient segmentation of cysts, stones, and kidney in renal US images is carried out using GVF. The experiments are carried out to assess the suitability of using GVF deformable curves. The performance evaluation of the method is enlightened in this chapter.

In the present chapter, the objective is to propose a semiautomatic segmentation method for the segmentation of the kidney, cyst, and stone in US images.

## 3.2 Proposed method

The proposed method of segmentation of normal kidney, stone, or cysts in renal ultrasound images is shown in Fig. 3.1. The input ultrasound image of the kidney is denoised using contourlet transform. The denoised image is read as input by GVF segmentation algorithm along with an initial contour specified based on expert opinion. The GVF segmentation method mainly aims at finding the précised boundary of the region. The GVF segmented image is evaluated using the performance parameters such as Dice coefficient (DC) and Jaccard coefficient (JC), sensitivity, specificity, accuracy, and execution time. The segmented output image is compared with the manually marked image by a medical expert.

In order to apply GVF, an edge map f(x,y) is computed on the despeckled image S(m,n). It is having a larger size and is approximately nearer to the actual boundary. Further, it is deformed towards the actual edges of the ROI using GVF external force.

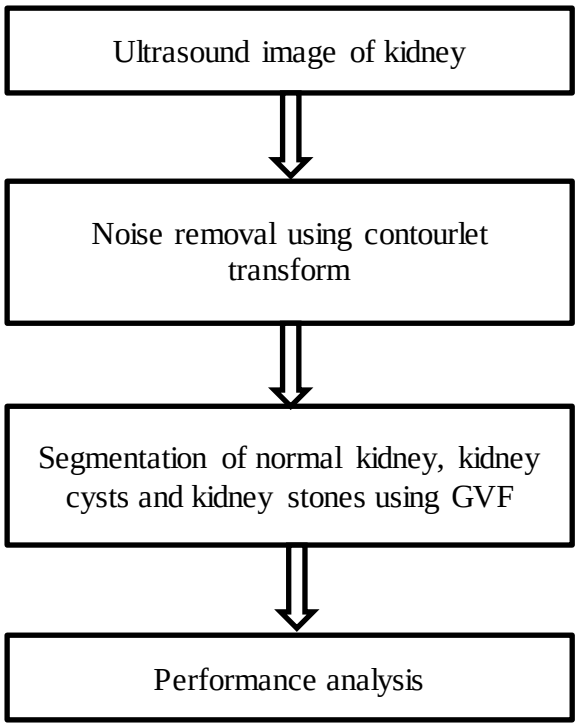


Fig. 3.1. Block diagram of the proposed methodology

It is essential to mention the initial parameter for the snake deformation. After complete evolution, the initialized balloon fits into the actual ROI boundary. The different steps of GVF segmentation are shown in Algorithm 3.1.

**Algorithm 3.1: GVF based segmentation model**

*Input:* Denoised renal US image (S) with initial contour.

*Output:* Segmented kidney/cystic/stone region.

*Begin*

*Step 1:* Read the denoised renal US image S.

*Step 2:* Set the initial parameters and boundaries of initial contour, based on expert opinion for the balloon deformation.

*Step 3:* Compute an edge map of S using Eq. (1.7.7) to obtain the GVF field.

*Step 4:* Construct the GVF by diffusing the edge force and is achieved by minimizing the energy functional which is given by Eq. (1.7.8). The value of gradient is calculated using Euler equations specified in Eq. (1.7.9) and Eq. (1.7.10).

*Step 5:* Based on the GVF external force on the edge map, interpolate the snake for segmentation of ROI.

*Step 6:* Continue deformation, until the balloon completely fits in the actual boundary.

*Step 7:* Obtain the précised boundary of the ROI.

*End*.

The basic details of the gradient vector force method are described in section 1.7.2 of the Chapter1. The GVF snake model is applied for the segmentation of renal cysts in US images. As described in Algorithm 3.1, denoised US image of the kidney is taken as input. An edge map of denoised image is computed followed by Gaussian filter to get the smoothened image. Initial parameters like coordinates for oval, angles, and the number of iterations are explicitly provided as input. The initial contour is generated based on expert advice. Further, the GVF snake is interpolated and deformation is continued until the deformed curve fits into the precise boundary of the ROI of kidney or cysts/stones.

It is suitable for segmenting the kidney, cysts, and stones found in an ultrasound image. Accurate sizes of cysts and stones obtained through the proposed GVF method can help the nephrologists to provide the appropriate medical treatments for patients.

## 3.3 Experimental Results and Discussion

The experimentation is performed on all 185 US images of the kidney, cysts, and stones. The dataset specified in section 1.5 contains the clinical (S1) and web (S2) datasets, comprising of 37 normal kidney images, 39 single-cystic, 35 polycystic, 38 single-stone, and 36 multiple-stones images altogether. The algorithm is implemented on Intel core i5 processor with 4GB RAM @ 2.5GHz, using MATLAB 7.11. The denoising of images is carried out using spatial and transform domain filters.

### 3.3.1 Speckle noise removal

The input image dataset specified in section 1.5 is considered for the study. Experimental results obtained using various speckle noise removal algorithms are described in this section. Experimentation is carried both on the spatial domain and transform domain filters. An input image is applied with logarithmic transform before filtering, through various spatial domain

Table 3.1 Performance of different filters using window sizes of 3X3, 5X5, 7x7 in terms of MSE, PSNR, and CC

| **Filter size** | **Despeckling filter** | **MSE** | **PSNR** | **CC** |
|---|---|---|---|---|
| 3X3 | Gaussian filter | **0.00476** | **27.756** | **0.981** |
| | Median filter | 0.00539 | 26.729 | 0.967 |
| | Weiner filter | 0.00512 | 25.315 | 0.956 |
| | Wavelet transform (Bior 6.8 family, level 3 decomposition) | 0.00413 | 28.143 | 0.984 |
| | Contourlet transform | **0.00348** | **29.729** | **0.997** |
| 5X5 | Gaussian filter | 0.00572 | 25.891 | 0.961 |
| | Median filter | 0.00641 | 24.312 | 0.942 |
| | Weiner filter | 0.00598 | 23.815 | 0.939 |
| | Wavelet transform (Bior 6.8 family, level 3 decomposition) | 0.00452 | 26.736 | 0.954 |
| | Contourlet transform | 0.00463 | 27.234 | 0.956 |
| 7X7 | Gaussian filter | 0.00613 | 24.106 | 0.923 |
| | Median filter | 0.00647 | 22.849 | 0.905 |
| | Weiner filter | 0.00687 | 22.153 | 0.898 |
| | Wavelet transform (Bior 6.8 family, level 3 decomposition) | 0.00549 | 24.635 | 0.943 |
| | Contourlet transform | 0.00518 | 26.729 | 0.951 |

From filters like Gaussian, median, and Weiner filters. Then, inverse log transform is applied to get a despeckled image. The performance of the spatial domain filters is evaluated using

parameters such as MSE, PSNR, and CC. Different window sizes of 3X3, 5X5, and 7X7 have experimented, results are tabulated as shown in Table 3.1.

Table 3.1, it is observed that the window size of 3X3 is optimal. The Gaussian filter performs better compared to the other two filters namely, Weiner and median filters. Fig. 3.2 shows the filtered images by using different spatial domain filters namely, Gaussian, median, and Weiner filters for each of the input image classes namely, normal kidney, cystic, polycystic, single-stone, and multiple-stones ultrasound images of kidney respectively. Further, the wavelet transform and contourlet transform are good at noise removal than the spatial domain filters.

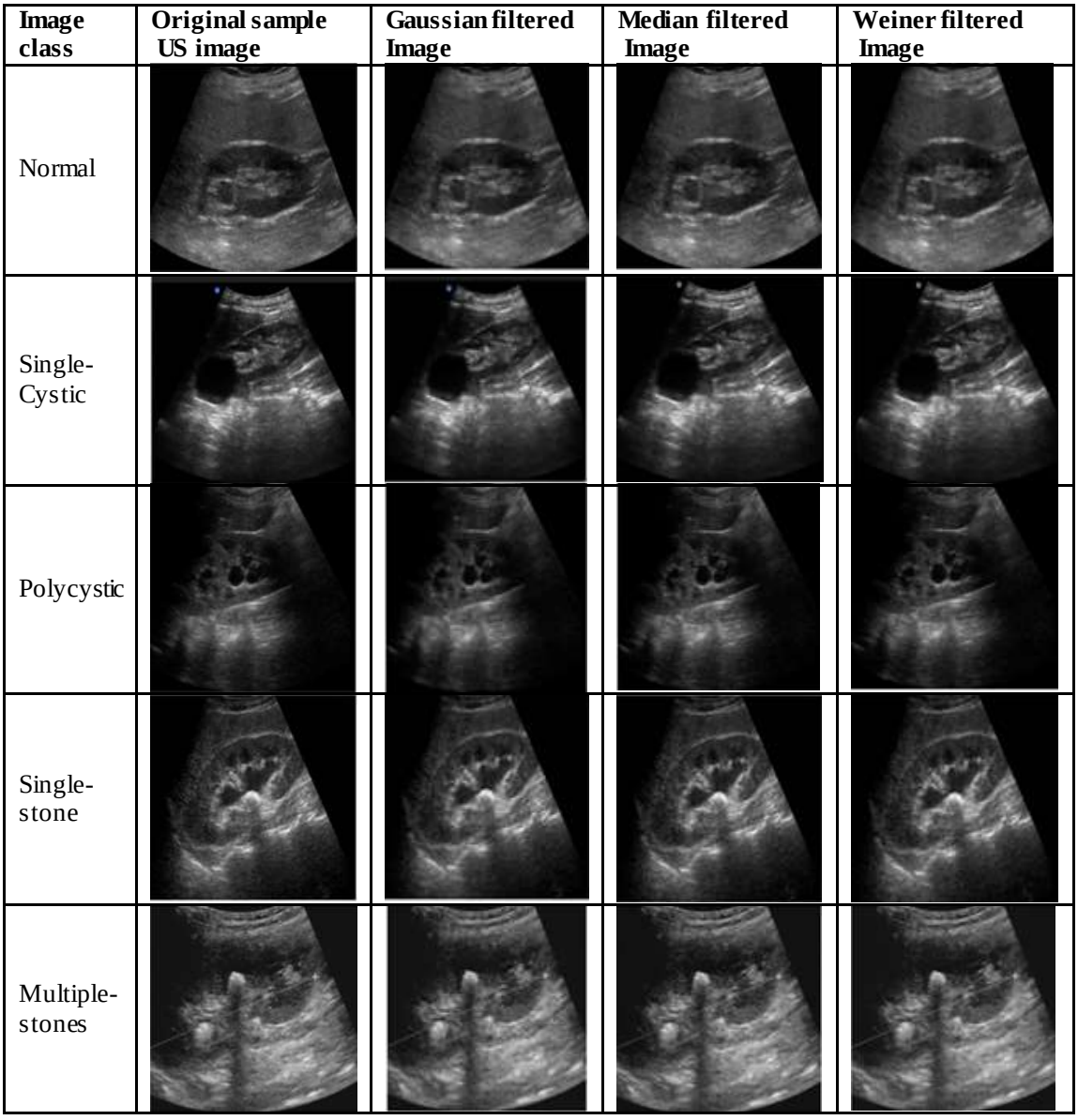


Fig. 3.2 Denoised images obtained using spatial domain filters

| Image class | Original sample US image | Wavelet filtered Image | Contourlet transformed Image | Contrast enhanced image of contourlet transformed image |
|---|---|---|---|---|
| Normal | 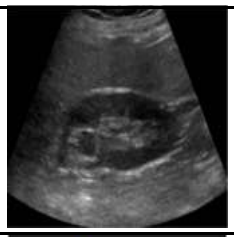 | 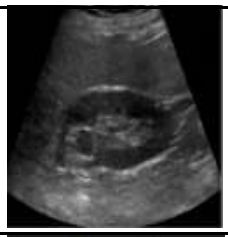 | 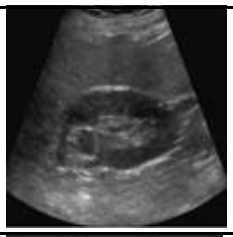 | 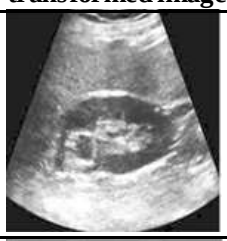 |
| Single-Cystic | 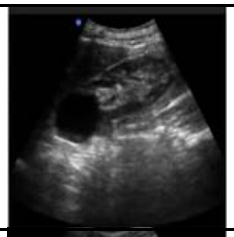 | 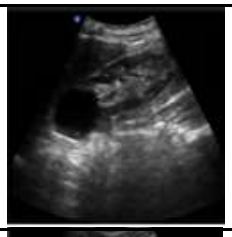 | 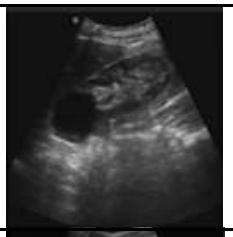 | 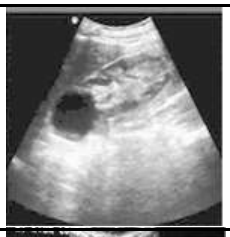 |
| Polycystic | 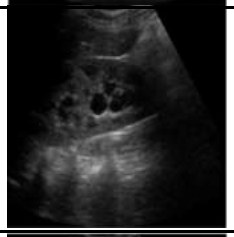 | 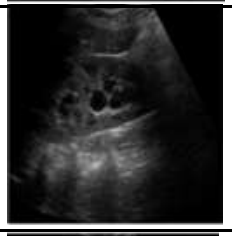 | 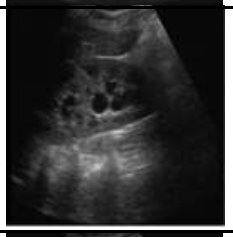 | 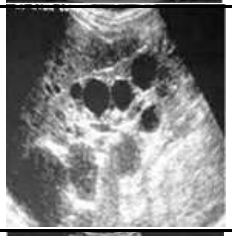 |
| Single-stone | 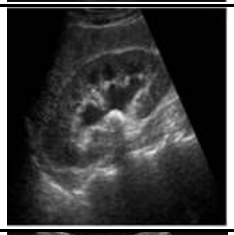 | 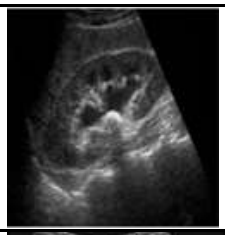 | 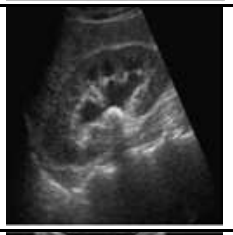 | 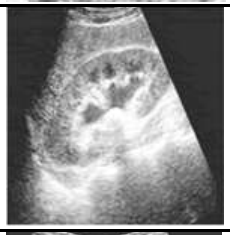 |
| Multiple-stones | 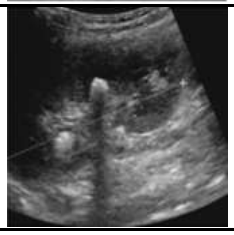 | 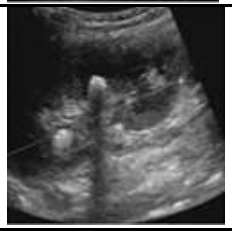 | 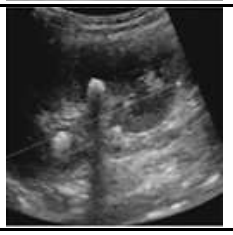 | 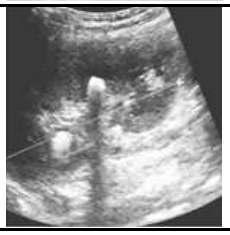 |

Fig. 3.3 Denoised images obtained using transform domain filters

Experimentation on different wavelet families and different levels of decomposition is carried out. The decomposition level of 3 with biorthogonal 6.8 is found to be more accurate, empirically. Similar to the previous filters, log and inverse log transform is applied before and after applying contourlet transform respectively. For, the input images of size 512X512, two levels of LP decomposition with six levels of directional decomposition filters are found as optimal. Hard thresholding is performed further. The final despeckled image is obtained by applying the inverse contourlet transform. Among all the five despeckling methods,

contourlet transform demonstrates better efficiency and it is justified by the obtained values for MSE, PSNR, and CC. The better performance of the contourlet transforms is evident from the performance parameter values as shown in Table 3.1. Fig. 3.3 shows the denoised images using the transform domain filters namely, wavelet biorthogonal 6.8 and contourlet transform.

The despeckled image obtained by applying a contourlet transform is passed through the contrast enhancement. The contrast-enhanced image is obtained by applying histogram equalization to get better quality image. The contrast-enhanced images of sample despeckled images using contourlet transform are shown in the last column of Fig. 3.3.

From Fig. 3.3, it is observed that the contourlet transform is more efficient than the wavelet method. Hence, contourlet transform followed by histogram equalization is used for denoising. Thus contrast enhanced, despeckled image of input US image is used for segmentation.

### 3.3.2 Segmentation of normal kidney, cyst, and stone

The denoised images are segmented by applying GVF algorithm. The GVF based segmentation requires initial parameters to be defined. Initial parameters include center of ROI to be segmented and boundary expansion limit both along X and Y axes. It is empirically found that normal images require a boundary limit varying between 50px to 180px. The single-cystic and single-stone images contain smaller ROI, the boundary limit is as small as 5px to 30px. The polycystic and multi-stone ultrasound images of the kidney, requires boundary limit ranging between 60px to 280px.

The segmentation of ultrasound image of the normal kidney using GVF based segmentation algorithm is described in Fig 3.4 (a) to (e). The sample denoised normal ultrasound image of the kidney is shown in Fig 3.4(a). Fig 3.4(b) is the initial contour defined manually. Fig 3.4 (c) shows intermediate deformation of the GVF-snake and Fig 3.4 (d) is the finally deformed image. Fig 3.4(e) is a manually segmented image by a medical expert. A good correlation is observed between GVF segmented image and manually annotated image by medical expert.

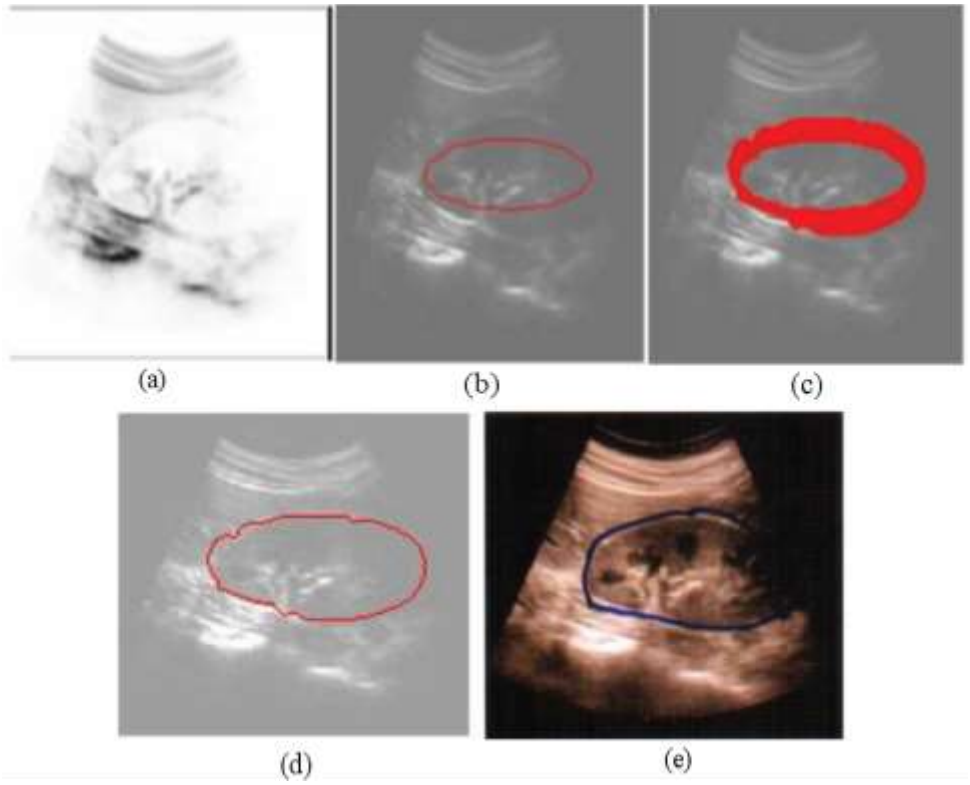


Fig. 3.4. Segmentation of normal kidney using GVF model: (a) Denoised normal kidney ultrasound image (b) User defined initial contour (c) Intermediate deformed image (d) Finally segmented image (e) Manually annotated image by medical expert

The performance of the GVF model is measured by the performance parameters namely Dice similarity coefficient and Jaccard coefficient, as mentioned in section 1.7.5. The values of Dice coefficient and Jaccard coefficient calculated for segmented ultrasound image of the normal kidney are 0.806 and 0.814 respectively for all normal kidney images in the dataset. The execution time for segmentation is 14.092 seconds.

The GVF segmentation is carried out on all 39 normal kidney images. Some of the sample outputs are shown in Fig. 3.5.

| Input US image | Segmentedimage by proposed GVF method | Manually annotated image by medical expert | Results |
|---|---|---|---|
| 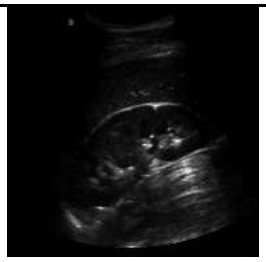 |  | 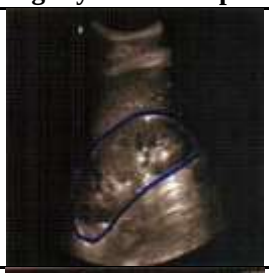 | DC=0.73<br>JC=0.718<br>Sensitivity=0.813<br>Specificity=0.857<br>Accuracy=0.876 |
| 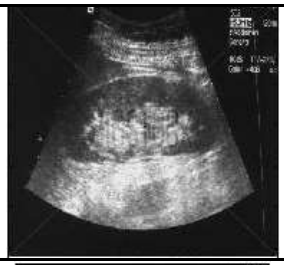 | 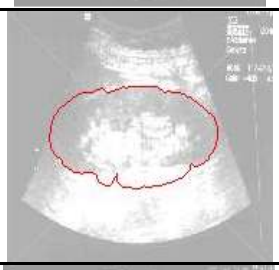 | 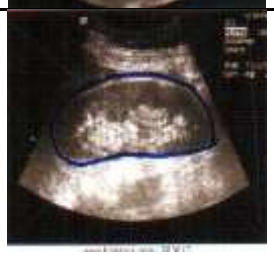 | DC=0.91<br>JC=0.904<br>Sensitivity=0.923<br>Specificity=0.935<br>Accuracy=0.931 |
| 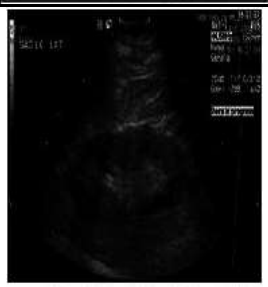 | 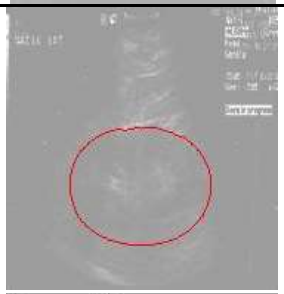 | 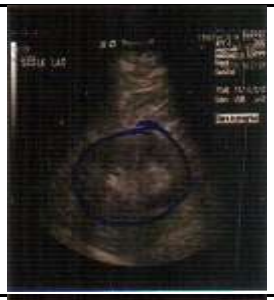 | DC=0.78<br>JC=0.774<br>Sensitivity=0.831<br>Specificity=0.837<br>Accuracy=0.846 |
| 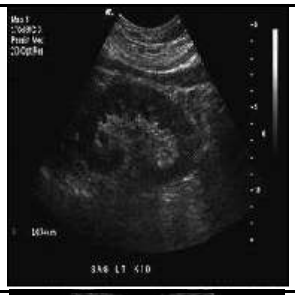 | 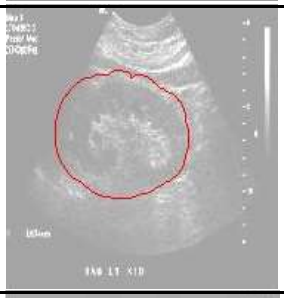 | 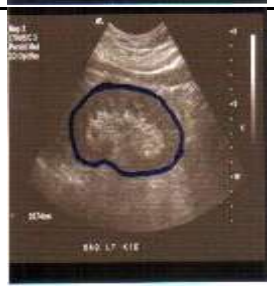 | DC=0.783<br>JC=0.764<br>Sensitivity=0.842<br>Specificity=0.851<br>Accuracy=0.84 |
| 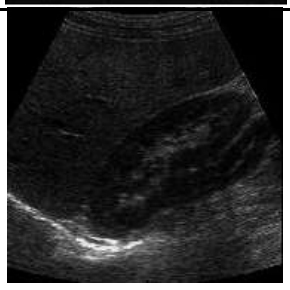 | 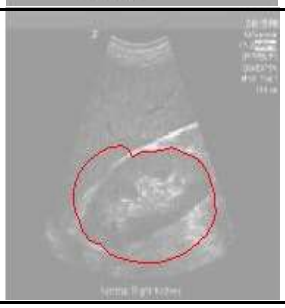 | 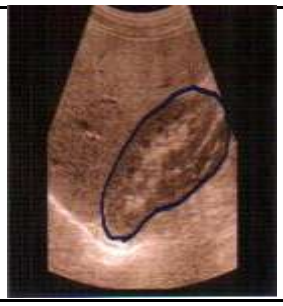 | DC=0.761<br>JC=0.758<br>Sensitivity=0.817<br>Specificity=0.823<br>Accuracy=0.838 |

Fig. 3.5. Results of normal kidney segmentation using proposed GVF method

The segmentation of single-cystic ultrasound image of the kidney is described in Fig 3.6 (a) to (e). Fig 3.6 (a) shows the sample denoised image of a single-cystic kidney. Fig 3.6 (b) is the pre-defined initial contour. The Fig 3.6 (c) is the intermediate stage of GVF deformation

and the Fig 3.6 (d) is the finally segmented image. Fig 3.6 (e) is the manually segmented image by a medical expert. Fig 3.6 (d) and Fig 3.6 (e) show a good visual resemblance. The segmented image is binarized to find the size of the cyst. The cyst size is obtained as 38.5mm$^2$. The cyst size specified by medical expert is 35.8mm$^2$. A small deviation is observed in experimentally determined size of the cyst and actual size.

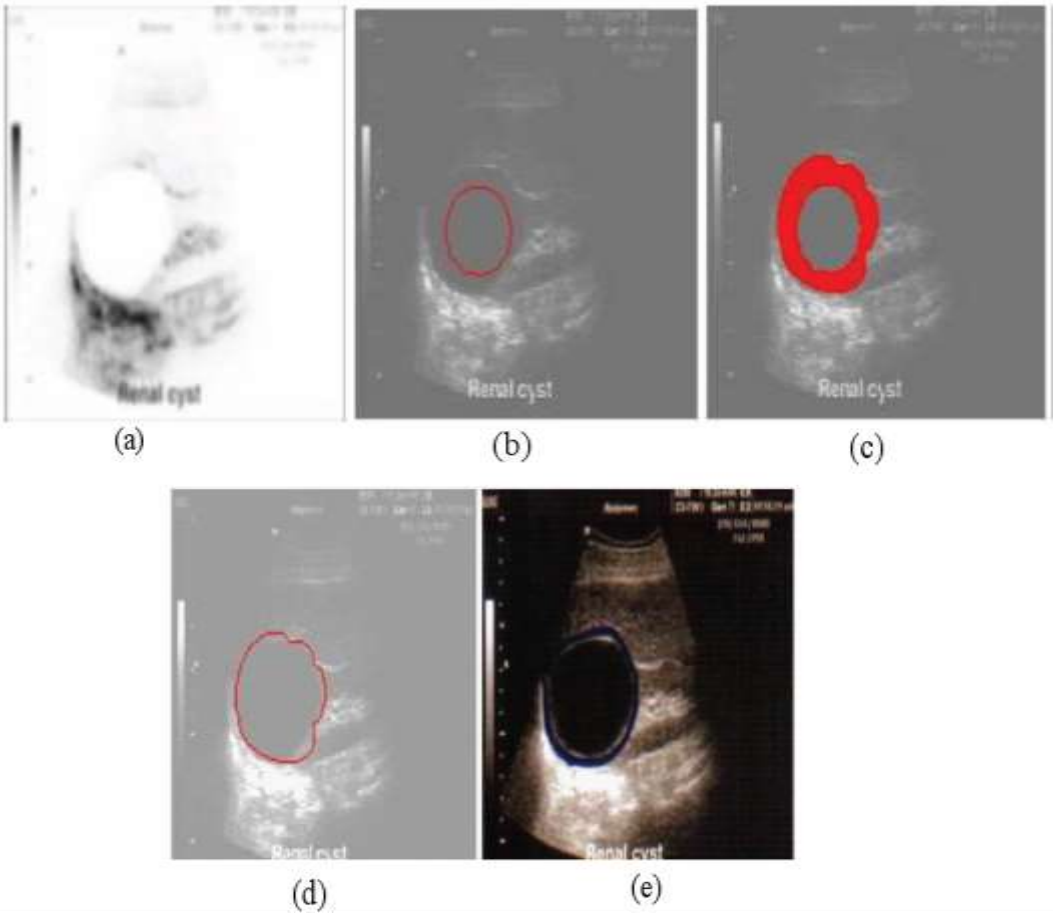


Fig. 3.6. Segmentation of single-cystic kidney using GVF model: (a) Denoised single-cystic kidney ultrasound image (b) Predefined initial contour (c) Deformed intermediate image (d)Finally segmented image (e) Segmentation by a medical expert.

The performance of segmented output image is verified by performance parameters. The values of Dice coefficient and Jaccard coefficient calculated for segmented ultrasound image of single-cystic kidney are 0.837 and 0.844 respectively. The execution time required for segmentation is 12.149 seconds. Thus, it demonstrates the effective application of GVF for the segmentation of single-cystic kidney images.

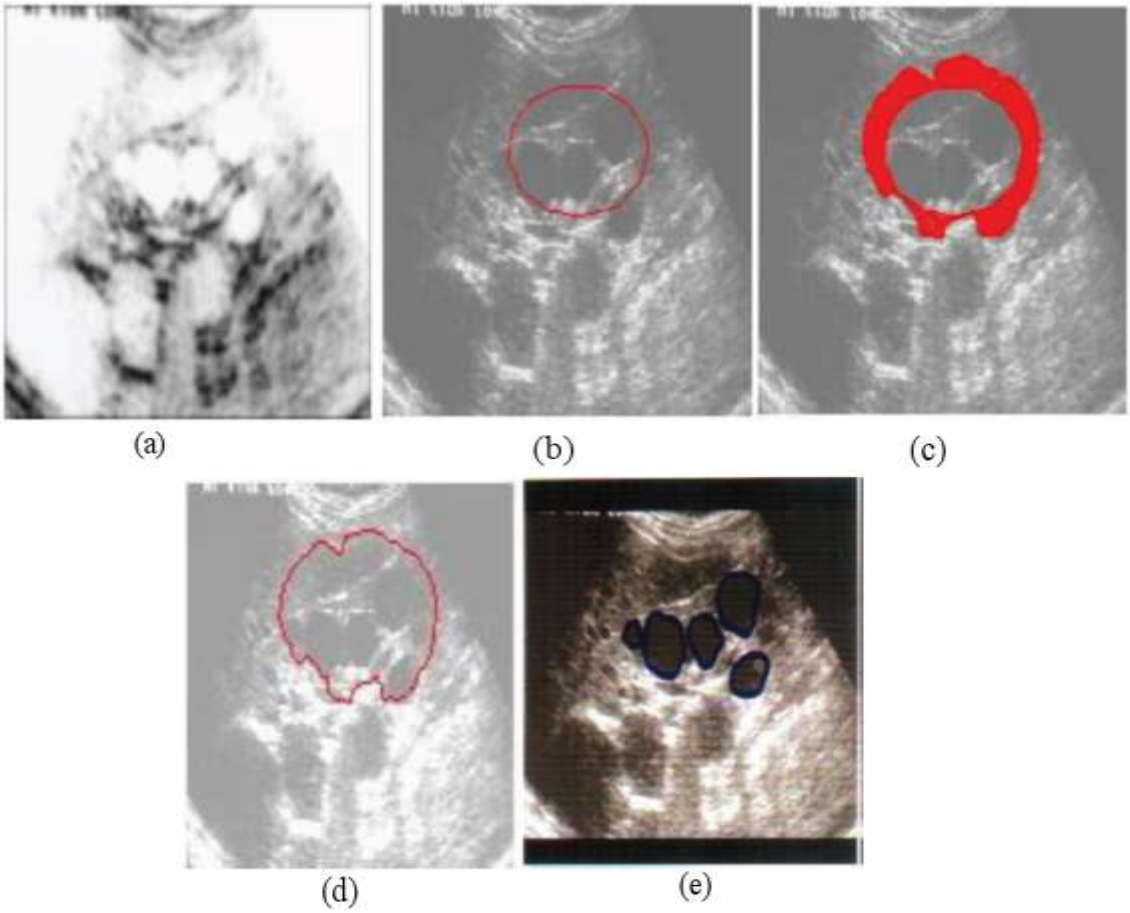


Fig. 3.7. Segmentation of polycystic kidney using GVF model: (a) Denoised polycystic ultrasound image of kidney (b) Predefined initial contour (c) Deformed intermediate image (d) Segmented image (e) Manually annotated image by medical expert

Similarly, the segmentation of polycystic ultrasound image of the kidney is described in Fig 3.7 (a) to (e). The Fig 3.7 (a) shows the sample denoised image of a polycystic kidney, Fig 3.7 (b) is the pre-defined initial contour, Fig 3.7 (c) is the intermediate stage of GVF deformation and the Fig 3.7 (d) is the finally segmented image of polycystic kidney. Fig 3.7 (e) is the manually marked image by a nephrologist. The values of Dice coefficient and Jaccard coefficient calculated for segmented ultrasound image of the polycystic kidney are 0.724 and 0.715 respectively. The execution time for the segmentation of polycystic kidney image sample is 20.651 seconds. The comparison between Fig 3.7 (d) and Fig 3.7 (e) shows that a single region enclosing all the cysts is segmented instead of segmenting the cysts individually.

| Image class | Input US image | Segmentedcystic image by proposed GVF method | Manually annotated image by medical expert | Results |
|---|---|---|---|---|
| Single cystic | 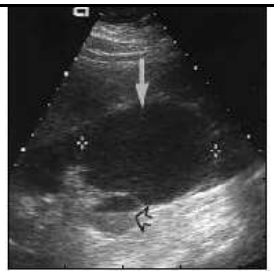 | 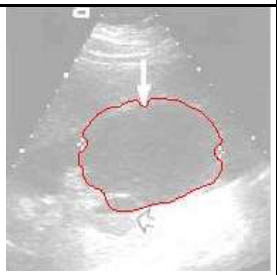 |  | DC=0.853<br>JC=0.858<br>Sensitivity=0.891<br>Specificity=0.897<br>Accuracy=0.895<br>Cyst size= 38.4mm$^2$ |
| Single cystic | 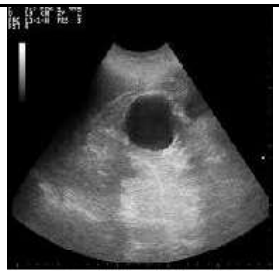 | 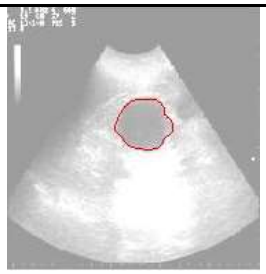 | 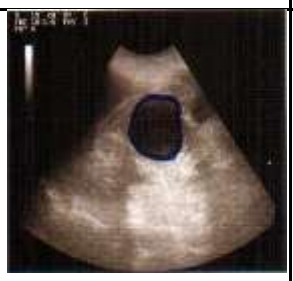 | DC=0.921<br>JC=0.914<br>Sensitivity=0.963<br>Specificity=0.956<br>Accuracy=0.961<br>Cyst size=26mm$^2$ |
| Polycystic | 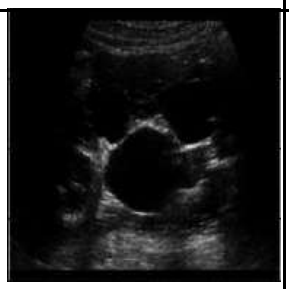 | 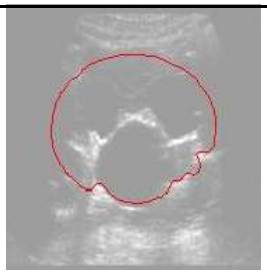 | 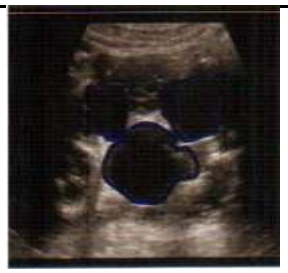 | DC=0.68<br>JC=0.676<br>Sensitivity=0.734<br>Specificity=0.774<br>Accuracy=0.765 |
| Polycystic | 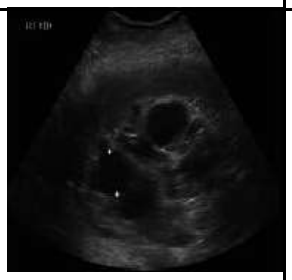 | 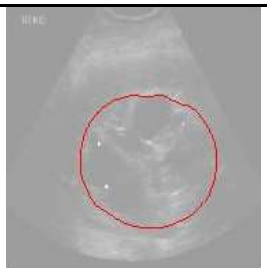 | 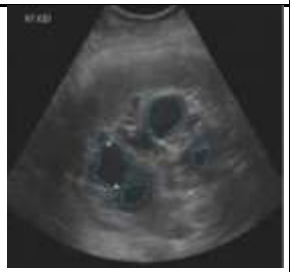 | DC=0.734<br>JC=0.741<br>Sensitivity=0.754<br>Specificity=0.750<br>Accuracy=0.784 |
| Polycystic | 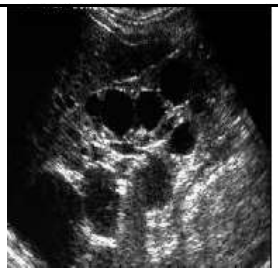 | 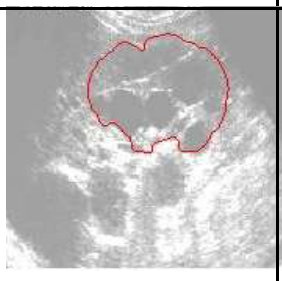 | 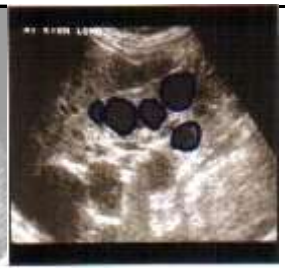 | DC=0.776<br>JC=0.781<br>Sensitivity=0.798<br>Specificity=0.793<br>Accuracy=0.792 |

Fig. 3.8. Results of kidney cysts segmentation using proposed GVF model

The segmented results of cystic kidney images are shown in Fig. 3.8. All the 74 images are segmented using GVF. Some of the samples are shown in Fig. 3.8.

Fig 3.9 (a) to (e) show the sample denoised image of a single-stone kidney, initial contour, the intermediate stage of GVF deformation, the finally segmented image, and manually marked image by medical expert respectively. A good resemblance observed between the segmented image by GVF and the manually marked image by the medical expert. The size of the stone is calculated as 17.7 $mm^2$ and the value mentioned by a medical expert is 15 $mm^2$. A small relative error is observed in the experimentally obtained value.

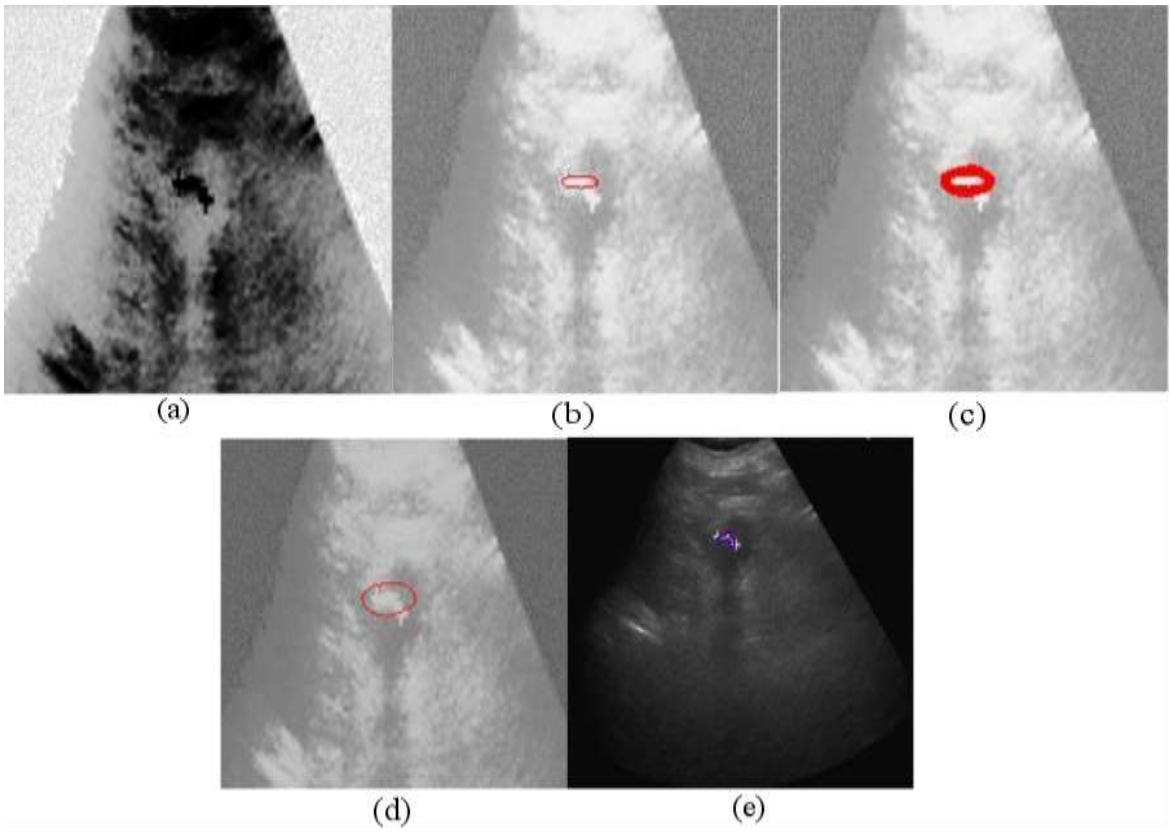


Fig. 3.9. Segmentation of single-stone kidney using GVF model: (a) Denoised single-stone ultrasound image of kidney (b) User-defined initial contour (c) Deformed intermediate image (d) Finally segmented image (e) Manual annotation by medical expert

Similarly, the segmentation of multi-stone ultrasound image of the kidney is described in Fig 3.10 (a) to (e). Fig 3.10(a) shows a sample denoised image, the Fig 3.10(b) is the pre-defined initial contour, Fig 3.10(c) is the intermediate stage of GVF deformation and the Fig 3.10 (d) is the finally segmented image of a multi-stone kidney. Fig 3.10 (e) is the manually marked

image by the urologist. The values of Dice coefficient and Jaccard coefficient calculated for segmented ultrasound image of the multiple-stones kidney are 0.617 and 0.624 respectively. The execution time for segmentation of multiple –stone image sample is 19.347 seconds. Similar to polycystic image, the comparison between Fig 3.10 (d) and Fig 3.10 (e) shows that a single region containing all the stones is segmented instead of segmenting the individual stones.

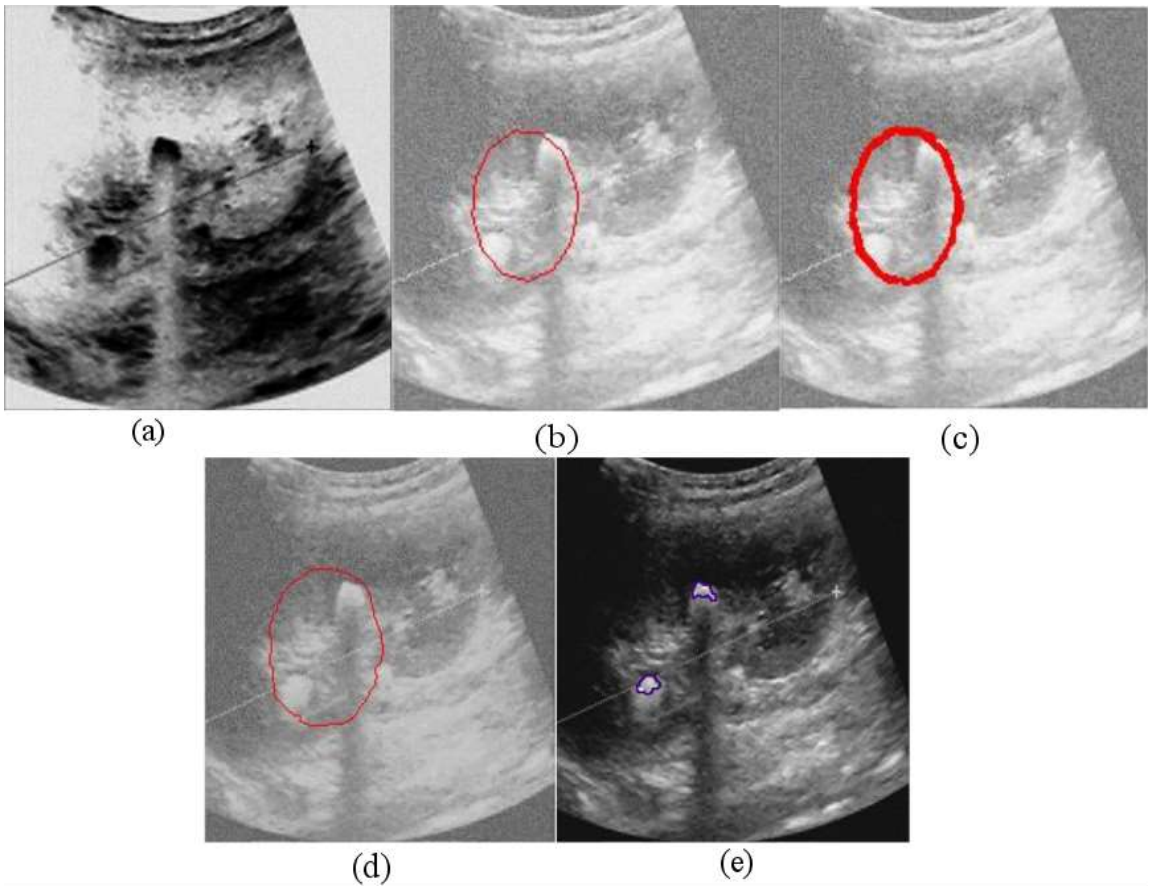


Fig. 3.10. Segmentation of multiple-stones kidney using GVF model: (a) Denoised multiple-stones ultrasound image of the kidney (b) Predefined Initial contour (c) Deformed intermediate image (d) Finally segmented image (e) Manual annotation by medical expert

All 74 renal calculi images are tested using GVF. The dataset includes 38 single-stone and 36 multiple-stones images. The results of segmentation for some of the samples are shown in Fig. 3.11.

From Fig. 3.11, it is observed that the proposed GVF algorithm effectively segments single-stone kidney US images. However, a single larger region enclosing all the stones is segmented for multiple-stones image.

| Image class | Input US image | Manually annotated image by medical expert | Segmented image by proposed GVF method | Results |
|---|---|---|---|---|
| Single stone | 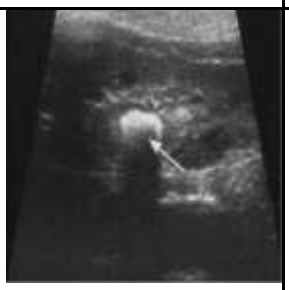 | 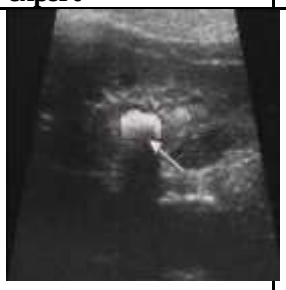 | 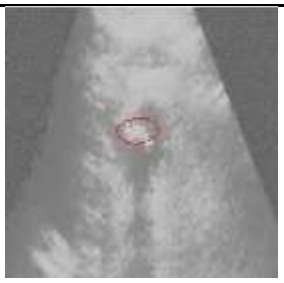 | DC=0.886<br>JC=0.878<br>Sensitivity=0.886<br>Specificity=0.891<br>Accuracy=0.885<br>Stone size= 17.7mm$^2$ |
| Multiple -stones | 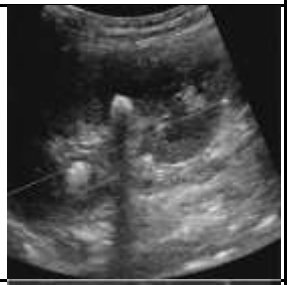 | 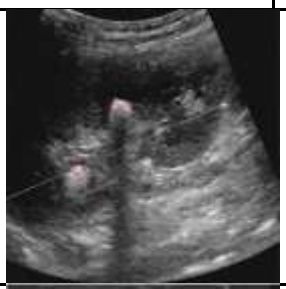 | 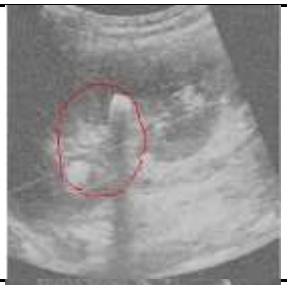 | DC=0.721<br>JC=0.719<br>Sensitivity=0.743<br>Specificity=0.752<br>Accuracy=0.740 |
| Multiple -stones | 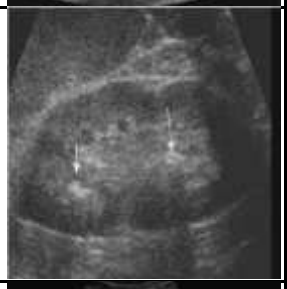 | 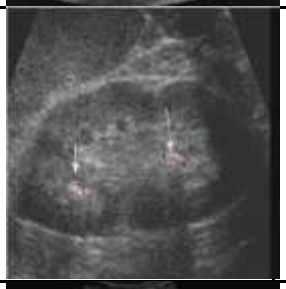 | 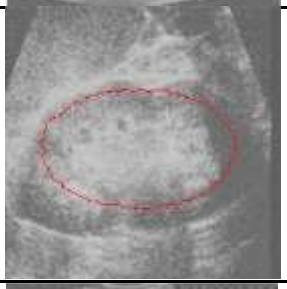 | DC=0.641<br>JC=0.6466<br>Sensitivity=0.647<br>Specificity=0.674<br>Accuracy=0.665 |
| Single stone | 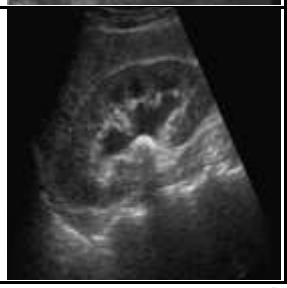 | 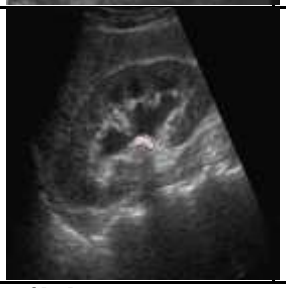 | 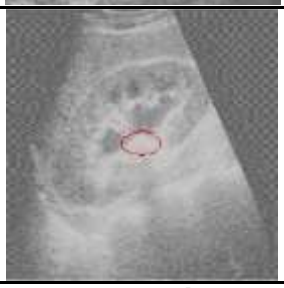 | DC=0.934<br>JC=0.941<br>Sensitivity=0.944<br>Specificity=0.935<br>Accuracy=0.941<br>Stone size= 15.2mm$^2$ |

Fig. 3.11. Results of kidney stones segmentation proposed GVF model

Considering all the images of the dataset specified in section 1.5, the performance of the GVF algorithm is calculated using DC, JC, and the execution time for segmentation of normal kidney, cysts, and stone in US images of the kidney. The mean and standard deviation of these parameters are computed considering all the images in both the datasets. The results obtained are shown in Table 3.2.

Table 3.2 Segmentation accuracy of the proposed GVF method

| Image class | Segmentation accuracy | | | | Execution time (in Sec.) |
|---|---|---|---|---|---|
| | DC | | JC | | |
| | Mean | SD | Mean | SD | |
| Normal kidney | 0.724 | 0.086 | 0.732 | 0.09 | 12.6 |
| Single cystic | 0.81 | 0.07 | 0.802 | 0.08 | 9.6 |
| Polycystic | 0.709 | 0.10 | 0.722 | 0.10 | 16.15 |
| Single stone | 0.746 | 0.08 | 0.761 | 0.07 | 9.8 |
| Multiple-stones | 0.654 | 0.09 | 0.682 | 0.09 | 13.2 |

From Table 3.2, it is observed that the proposed GVF algorithm can effectively segment the normal kidney, cysts, and stones in US images. The execution time required for the segmentation of polycystic and multiple-stones images are comparatively more. This is because of a single larger contour is deformed enclosing all the cystic/stone regions. The performance of GVF is evaluated using another set of parameters namely; sensitivity, specificity, and accuracy as elaborated in section 1.7.5 of Chapter 1, are shown in Table 3.3.

Table 3.3 Pixel level evaluation of the proposed GVF method

| Image class | Performance metrics | | | | | |
|---|---|---|---|---|---|---|
| | Sensitivity | | Specificity | | Accuracy | |
| | Mean | SD | Mean | SD | Mean | SD |
| Normal kidney | 0.84 | 0.06 | 0.86 | 0.07 | 0.85 | 0.07 |
| Single cystic | 0.78 | 0.07 | 0.79 | 0.06 | 0.79 | 0.10 |
| Polycystic | 0.70 | 0.09 | 0.702 | 0.08 | 0.71 | 0.09 |
| Single stone | 0.85 | 0.06 | 0.85 | 0.05 | 0.86 | 0.08 |
| Multiple-stones | 0.71 | 0.09 | 0.72 | 0.10 | 0.71 | 0.09 |

The set of parameters in Table 3.3 carry out a pixel-level comparison of segmented region and ground truth obtained by a medical expert. From Table 3.3, it is observed that there is a good agreement between the segmented image by applying GVF and the manually annotated image by medical expert for normal kidney, single stone and single cystic images of kidney.

One of the limitations of the GVF segmentation algorithm is, it segments a single larger region containing all cysts and all stones, in case of polycystic and multiple-stones ultrasound images of the kidney.

## 3.4 Summary

This chapter discusses about the segmentation of the normal kidney, single-cystic, polycystic, single-stone, and multiple-stones kidney US images using the GVF snake model. Speckle noise removal is one of the essential step, before the segmentation and classification of ultrasound images. Various filters and transform domain methods are used for the despeckling of kidney ultrasound medical images. Among all transform domain and spatial domain filters, contourlet transform is found to be better.

It is observed that GVF segmentation performs well in segmenting the normal kidney, single-cystic, and single–stone renal ultrasound images. The performance of the segmentation is measured using DC, JC, sensitivity, specificity, accuracy, and the amount of execution time taken for segmentation. The results obtained show the effectiveness of the method. The proposed GVF algorithm performs well in segmenting single-cystic and single –stone US images of kidney. But, in the case of polycystic and multiple-stones images, a single region enclosing all the cysts or stones is marked rather than segmenting individually.

GVF needs an explicit specification of the initial contour by the user. This is a time consuming process for the medical experts. In order to completely automate the segmentation algorithm, initial contour is automatically generated in subsequent chapters.

# Chapter 4

# AUTOMATIC SEGMENTATION OF CYSTS IN ULTRASOUND IMAGES OF KIDNEY USING ACTIVE CONTOUR MODEL

## 4.1 Introduction

The active contour model (ACM) is also known as the snake model. ACM is an effective frame-work to find the object boundary, particularly for 2D images (Cohen L.D. and Cohen I., 1990). It is more suitable for noisy images. A deformable curve (snake) is controlled by external and internal forces (Cohen L.D. and Cohen I., 1990). An external force drags the snake towards the object boundary. However, the internal force prevents the deformation movement outside the actual boundary. ACM uses a common approach for matching a deformable spline using energy minimizing function/term. Region-based ACM has its own strengths over its edge-based version. The region-based model works on the statistical data of the contour for controlling the deforming spline. Chan Vase(C-V) model (T. Chan and L. Vese, 2001) is used for the implementation. The C-V model is capable to segment all the ROIs in the two-dimensional image.

In some of the earlier methods, users have initialized a deformable model nearer to the ROI of the object to be segmented. It is deformed further to get a ROI of perfect shape and size. Users have used the interactive abilities of these models to manually tune the segmentation until perfectness is achieved. Additionally, if the user is satisfied with the result on an initial contour specified, then it can be used as the initial boundary approximation for other adjoining parts of the image as well. The resultant structure of 2-D contours can then be coupled together, to frame a continuous three-dimensional model (Lin, W.C. and Chen, S.Y., 1989; Chang, L.W., Chen, H.W. and Ho, J.R., 1991; Cohen, L.D., 1991; Cohen, L.D. and Cohen, I., 1993).

---

[1] Akkasaligar Prema T. , and Biradar Sunanda, "Automatic Segmentation of Kidney Cysts in Medical Ultrasound Images", UGC Sponsored National Conference on Recent Trends in Image Processing and Pattern Recognition-2016,, Karnataka Arts, Science and Commerce College, Bidar, Karnataka, India 2-3 April 2016, pp. 140-147.

Several segmentation algorithms including GVF and ACM require an initial contour or seed point to be specified explicitly. A fixed shape of the ellipse for the kidney is assumed globally to segment it. Further, Fisher-Trippets are used to find the gray level properties of an image and to classify. This method does not work on different orientations of the image (Huang J., Yang H., Chen Y. and Tang L., 2013).

The survey of several segmentation algorithms for US images including watershed, region, and edge-based is found (Jeyakumar V, Hasmi M. K., 2013). Many researchers have integrated the knowledge of the shape of ROI to be segmented in deformable models using shape templates. These methods use manually defined shape structures to express a priori information needed for several applications of automated segmentation. The concept of pre-defined templates for deformation can be found in the initial works on spring-loaded templates (M. A. Fischler and R. A. Elschlager, 1973). In semi-automatic segmentation methods, seed point or initial contour has to be mentioned manually as in the GVF algorithm discussed in the previous Chapter. A fully automatic segmentation method for cysts segmentation in ultrasound images of kidney using ACM is proposed and described in this chapter.

Chapter 4 includes the discussion on automatic segmentation of cysts in despeckled and contrast-enhanced renal US images. It highlights about automatic generation of initial contour, ACM algorithm, results, performance evaluation, and analysis.

## 4.2 Proposed method

The proposed method for the segmentation of cysts in ultrasound images of the kidney using active contour model is shown in Fig. 4.1. The input image dataset is denoised using the contourlet transform. The detection of initial contour automatically is one of the major steps before the segmentation. Morphological operators are effectively used for initial contour detection followed by segmentation of cysts using ACM.

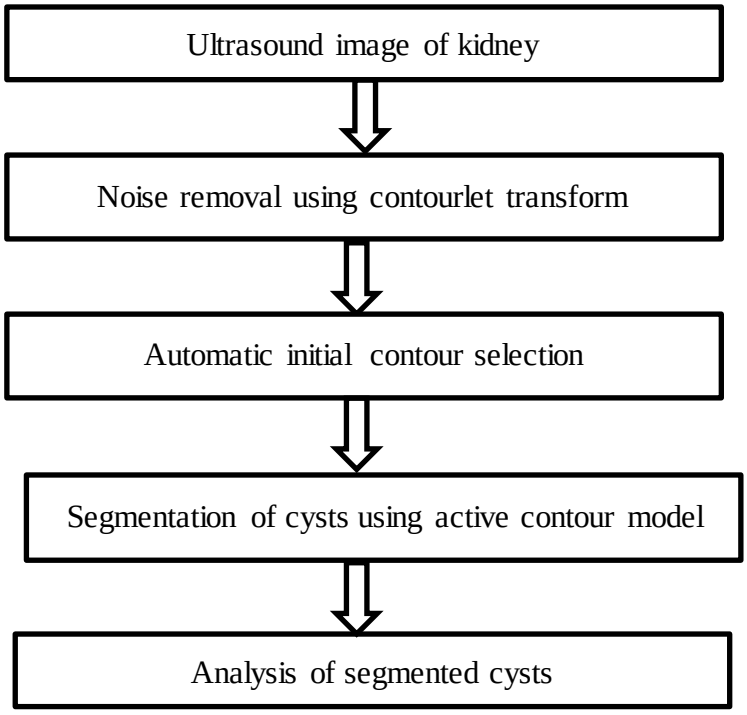


Fig. 4.1. Proposed method for segmentation of cysts in renal ultrasound images using ACM.

### 4.2.1 Automatic initial contour detection of cysts

Morphological operations have various applications in the field of image processing. They are used to segment the objects in two-dimensional images approximately. The size and shape of the segmented region by morphological operations are slightly varied compared to the actual ROI. Hence, the morphologically segmented region is taken as initial contour by ACM and is refined further to the actual ROI required. Algorithm 4.1 shows the steps to find the initial contour automatically, without the user intervention.

**Algorithm 4.1: Automatic generation of initial contour**

*Input:* Despeckled and contrast-enhanced renal US image(S).

*Output:* Initial contour generated (A) automatically.

*Begin*

*Step 1:* Read the despeckled and contrast-enhanced renal US image S.

*Step 2:* Find the binary form of S.

*Step 3:* Apply erosion to eradicate the elements that are thinner than their adjoining components attached to the image boundary.

*Step 4:* Compute the contour matrix for the eroded image.

*Step 5:* Apply morphological opening using disk-shaped SE (with a size of $M_1$) to remove weak edges.

*Step 6:* Erode the image in step 5 with a SE of size $M_2$ to discard the spurious regions.

*Step 7:* Find the count of regions and their boundary pixels to get the initial contour (A) automatically for each region in the image(S).

*End.*

The resultant image with automatic initial contour of Algorithm 4.1 is free from the regions with a lesser area than $M_1$ and $M_2$. The values of $M_1$=20px and $M_2$=10px, are empirically obtained. Thus initial contour is generated automatically using morphological operators irrespective of image size, orientation.

### 4.2.2 Segmentation of cysts using active contour model

ACM fundamentals discussed in Chapter 1, section 1.7.2 is used for the segmentation of cysts in renal US images. An input image defined with the initial contour is used for segmentation further. The step by step procedure is described in Algorithm 4.2.

**Algorithm 4.2: ACM based segmentation of renal cysts in US image** .

*Input:* Despeckled US image having an initial contour (A).

*Output:* Segmented renal cystic image.

*Begin*

*Step 1:* Read the image A.

*Step 2:* Set ∅(u)=0 and allocate to initial contour A which is to be deformed further.

*Step 3:* Compute the interior and exterior of energy terms of A.

*Step 4:* Find the value of energy minimizing function and start deformation.

*Step 5:* Continue deformation until it reaches the zero-crossing points or exceeds the prescribed number of iterations; then stop. Otherwise, go to Step 3.

*End.*

The proposed ACM method shown in Algorithm 4.2 is effectively used for completely automated segmentation of cysts in the kidney US images.

## 4.3 Analysis of segmented images

The analysis and interpretation of segmented outputs is extremely essential. The analysis can provide information such as the size, shape, location, and orientation of the extracted ROI. Automatic analysis of medical images can reduce the burden of doctors from the labor-intensive work of labeling and marking. It provides an alternative approach for improved accuracy, consistency, and reproduction of the interpretation.

In the analysis step, the information like the number of cysts and their size is computed after segmentation. The segmented image is binarized to calculate the number of regions indicating the number of cysts. The area is obtained by finding the pixel count covering the cystic region. The area of cyst is computed using the Eq. (4.1), mentioned in (P. R. Tamilselvi and P. Thangaraj, 2011).

$$\text{Area} = \sqrt{\text{P}} \times 0.264 \tag{4.1}$$

P is the number of pixels covering the cyst region. The sq. root of P is multiplied by 0.264. As the known fact is "1mm is equal to 0.264 pixels". Analysis of the segmented result provides useful information to the end-users. Particularly it is very important in the case of medical images, revealing the necessary information to the clinicians.

## 4.4 Experimental Results and Discussion

The experimentation is performed on all 74 US images of kidney cysts. 39 single-cystic and 35 polycystic kidney images present in the dataset specified in section 1.5 are used for experimentation. The ACM algorithm is implemented on a system of Intel core i5 processor with 4GB RAM @ 2.5GHz, using MATLAB 7.11. The denoising of images is carried out using contourlet transform as discussed in section 3.3.1 of Chapter 3. The denoised images are applied with the Algorithm 4.1 to generate the initial contour automatically. Further, the denoised images with initial contour are segmented by applying the ACM algorithm.

### 4.4.1 Automatic initial contour selection

The denoised image is binarized to apply morphological operations. Algorithm 4.1 is applied to get the image with an initial contour. Fig. 4.2 shows the images obtained at different steps of the algorithm.

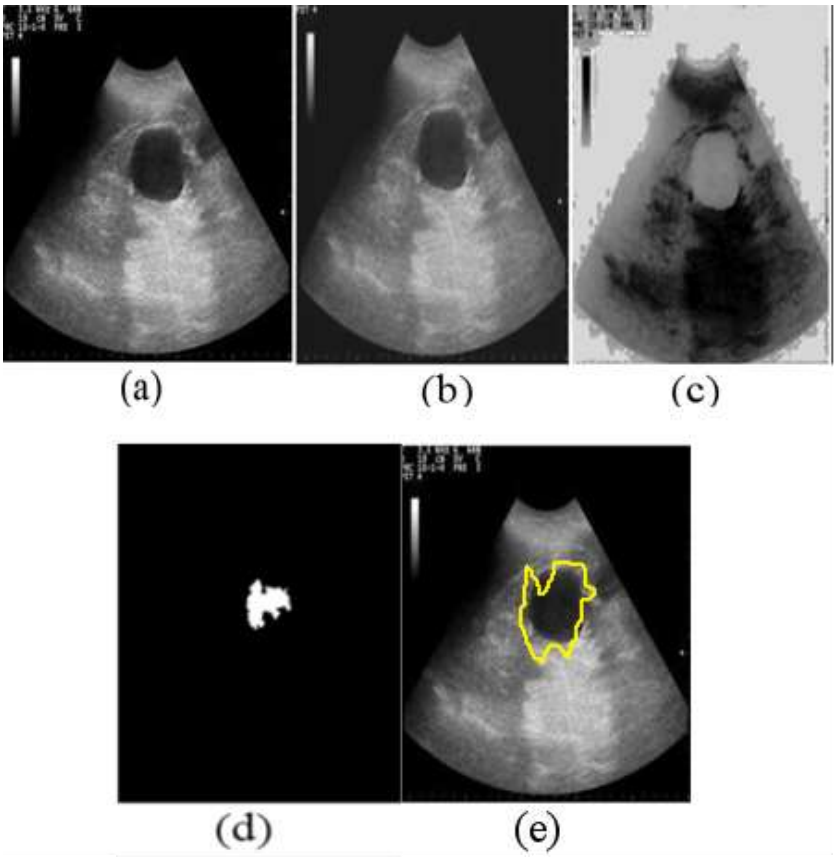


Fig. 4.2. Initial contour detection for single-cystic renal US image: (a) Original image (b) Despeckled image (c) Image after contrast enhancement (d) Image after a set of morphological operations resulting in initial contour (e) Automatically generated initial contour.

The initial contour needed for the segmentation of a single-cystic renal US image is obtained by applying Algorithm 4.1. A sample single-cystic renal US image is shown in Fig. 4.2(a). The despeckled image of Fig. 4.2 (a) is shown in Fig. 4.2 (b). The contrast-enhanced image is shown in Fig. 4.2 (c). After applying Algorithm 4.1 an initial contour for single-cystic renal US image is obtained and is shown in Fig 4.2 (d). A single region is obtained for a single-cystic image after applying a series of morphological operations as shown in Fig. 4.2 (d). The morphological opening is performed using a disk-shaped structuring element of size 20 pixels and holes of size 10 pixels are filled to discard the spurious regions. Fig. 4.2 (e) shows

the finally generated automatic initial contour for a single-cystic image. Thus, explicit specification of initial parameters required by the ACM segmentation algorithms is completely avoided.

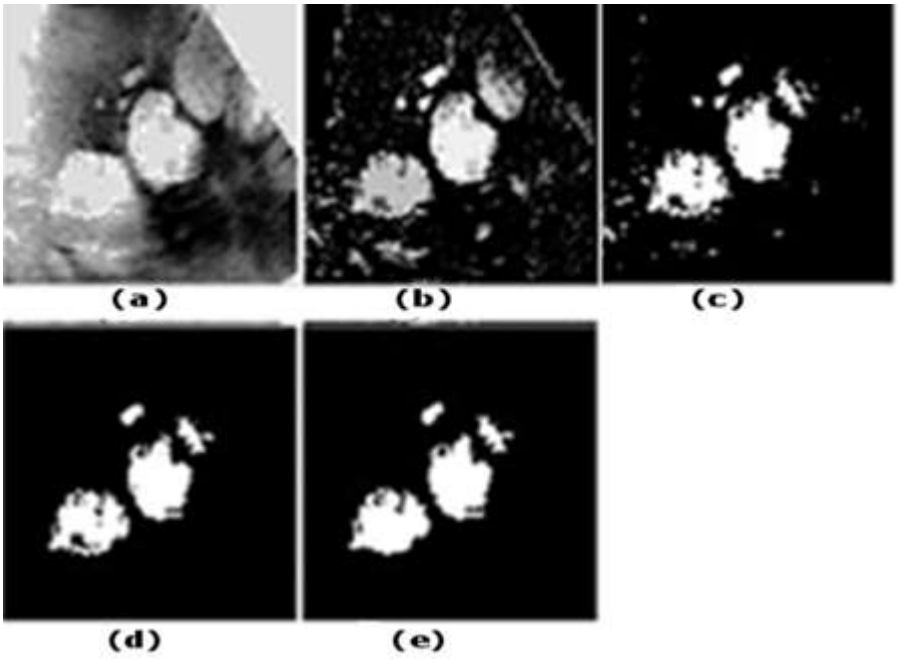


Fig. 4.3. Different stages of detecting initial contour for polycystic renal US image : (a) Despeckled image (b) Binary image (c) Eroded image (d) Image after morphological opening (e) Final image with distinct regions

The despeckled sample polycystic US image of the kidney, shown in Fig. 4.3(a) is converted into binary form, as shown in Fig 4.3 (b). Elimination of the elements that are thinner than the actual cyst ROI is performed using erosion and the resultant image is shown in Fig 4.3 (c). Further, a morphological opening is performed to remove the weaker edges as shown in Fig 4.3(d). For the opening, a disk-shaped SE of size 20 pixels is used. Further, it is passed through the filling of holes with a SE of size 10 pixels, resulting into Fig 4.3(e). Most of the spurious regions are discarded by morphological operations. Fig 4.3 (e) shows the clear separation of different cystic regions. Thus initial contour is generated automatically for both single-cystic and polycystic US images of the kidney.

### 4.4.2 Segmentation of cysts in renal US images

Algorithm 4.2 shows the detailed steps involved in the ACM model. Fig 4.4 shows the images obtained at different stages of ACM for the segmentation of a single cyst in renal US images. Fig 4.4(a) is the image obtained by applying the morphological operations as described in section 4.4.1. Internal and external energy terms are calculated. These two terms are used for computing the energy minimizing function, used for deformation. The deformed image in one of the intermediate stages after 60 iterations is shown in Fig 4.4(b). Deformation is continued until the maximum number of iterations is reached or no change is observed in successive iterations. The finally deformed image after 75 iterations is shown in Fig 4.4 (c). Finally, the segmented image can be compared with the manually marked image by a medical expert as shown in Fig 4.4 (d). The size of the cyst calculated using Eq. 4.1 is 26.5mm$^2$. The size specified by a medical expert is 28.2 mm$^2$. A smaller relative error is observed in the experimentally obtained value. Thus completely automatic ACM algorithm is effectively used for the segmentation of single-cystic images.

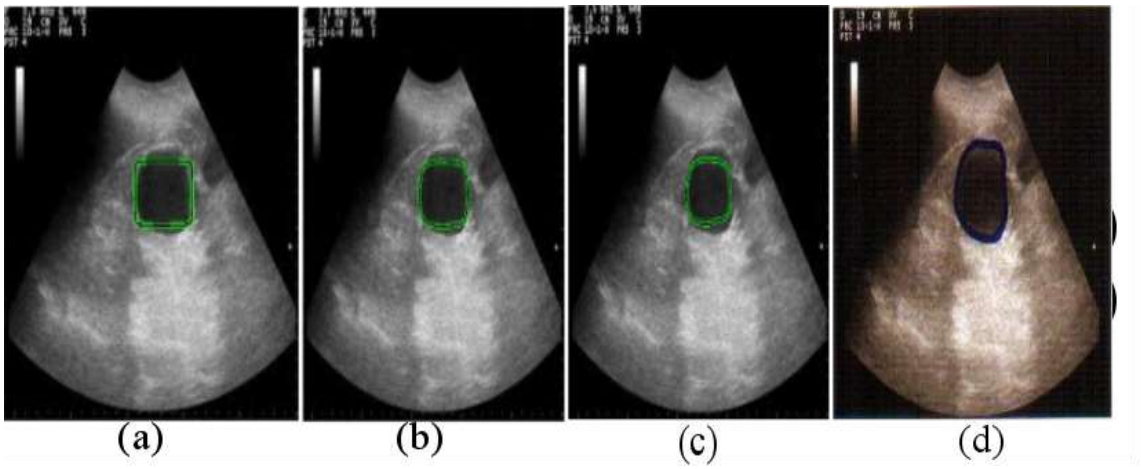


Fig.4.4. Different stages of segmentation of single-cystic renal US image: (a) Automatically generated initial contour (b)Intermediate deformation at the end of iteration number 60(c) Finally deformed boundary at the end of iteration number 75 (d) Manually marked image by a medical expert

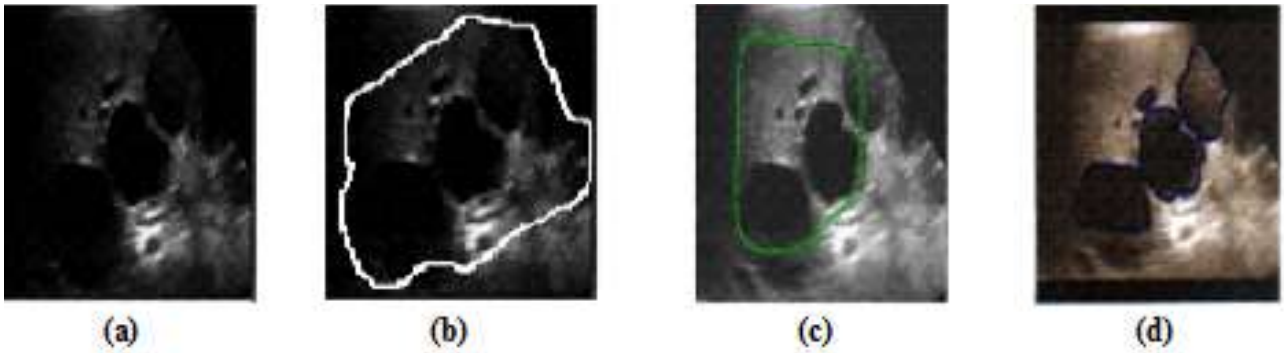


Fig. 4.5 Segmentation of polycystic renal US image : (a) Original input image (b) Automatically generated initial contour (c) Finally deformed boundary by ACM at the end of 90 iterations (d) Manually marked image by a medical expert.

Fig 4.5 shows the segmentation of polycystic renal US images using ACM. Fig 4.5 (a) is the sample polycystic renal image. ACM based segmentation algorithm accepts a single region as an initial contour. A single region is obtained by finding the minimum and maximum of X-Y coordinates by considering all the regions extracted by the initial contour detection algorithm specified by Algorithm 4.1. Finally, a larger single region covering all the cysts is determined as the initial contour for the segmentation of polycystic regions in renal US images. Thus, Fig 4.5 (b) shows the automatic initial contour generated for Fig 4.5 (a) using morphological operations. Fig 4.5(c) is finally segmented image after the completion of 90 iterations. It is compared with the manually marked image by a medical expert as shown in Fig 4.5 (d). ACM is unable to segment the individual cysts separately instead it segments a single region containing all the cysts.

### 4.4.3 Performance evaluation

Different parameters are used for performance evaluation of the segmentation such as Dice coefficient, Jaccard coefficient, sensitivity, specificity, and accuracy as discussed in section 1.7.5 of Chapter 1. All the single and polycystic images specified in section 1.5 of Chapter 1 are taken into account for the calculation of the mean and standard deviation. Some of the sample results obtained are shown in Fig. 4.6. Fig. 4.6 demonstrates the efficiency of the ACM method in the segmentation of single and polycystic renal US images. The proposed ACM algorithm segments the single-cystic images effectively without any user intervention.

| Image class | Input US image | Segmented image by proposed ACM method | Manually annotated image by a medical expert | Results |
|---|---|---|---|---|
| Single cystic | 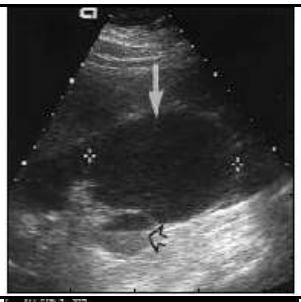 | 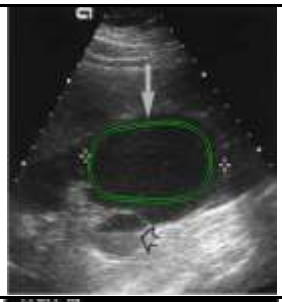 | 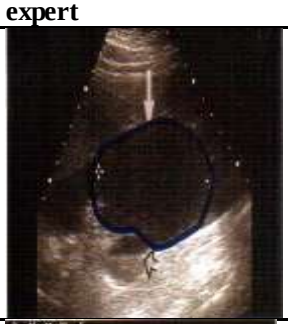 | DC=0.871<br>JC=0.867<br>Sensitivity=0.901<br>Specificity=0.907<br>Accuracy=0.915<br>Size of cyst= 36.1mm$^2$ |
| Single cystic | 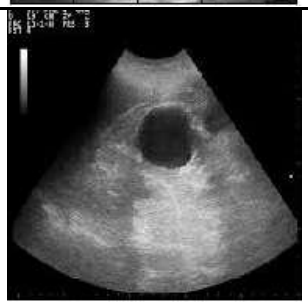 | 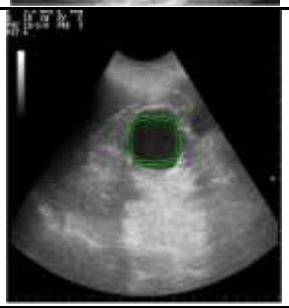 | 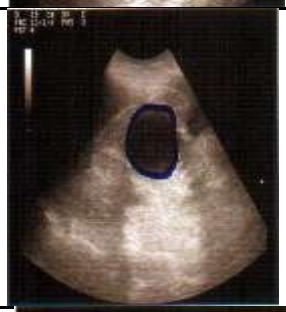 | DC=0.934<br>JC=0.931<br>Sensitivity=0.968<br>Specificity=0.962<br>Accuracy=0.964<br>Size of cyst= 26.5mm$^2$ |
| Polycystic | 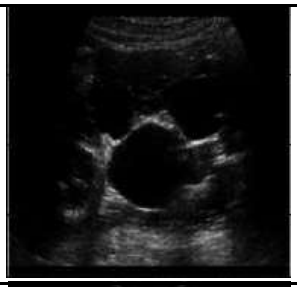 | 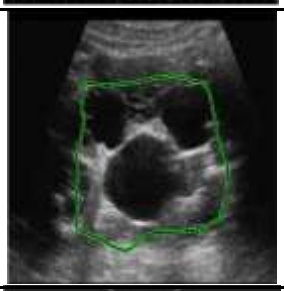 | 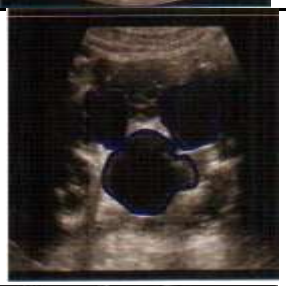 | DC=0.687<br>JC=0.682<br>Sensitivity=0.746<br>Specificity=0.781<br>Accuracy=0.773 |
| Polycystic | 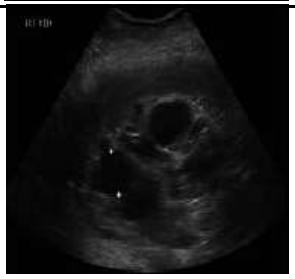 | 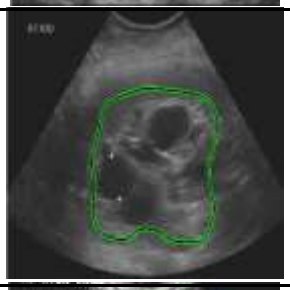 | 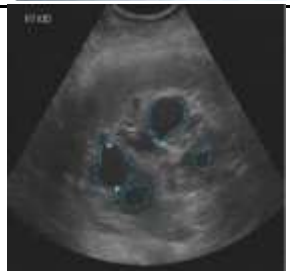 | DC=0.741<br>JC=0.740<br>Sensitivity=0.763<br>Specificity=0.765<br>Accuracy=0.792 |
| Polycystic | 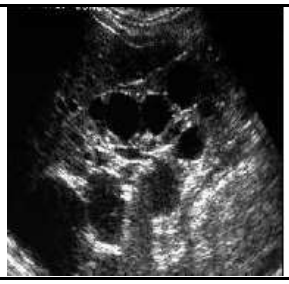 | 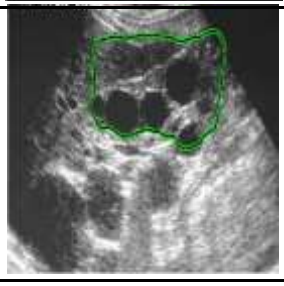 | 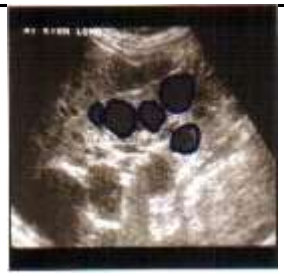 | DC=0.783<br>JC=0.782<br>Sensitivity=0.809<br>Specificity=0.806<br>Accuracy=0.799 |

Fig. 4.6. Results of cysts segmentation using proposed ACM algorithm

Fig.4.7 and 4.8 show the plots of performance parameters for the segmentation of single-cystic images. From Fig. 4.7and Fig. 4.8, it is observed that the mean values of DC, JC, sensitivity, specificity, and accuracy obtained for single cyst segmentation are nearer to 1 and are better than GVF based segmentation. The standard deviation values are too lower,

indicating no much deviation in the obtained values for the segmentation of individual images. Thus automatic segmentation of a single-cystic image is carried out successfully.

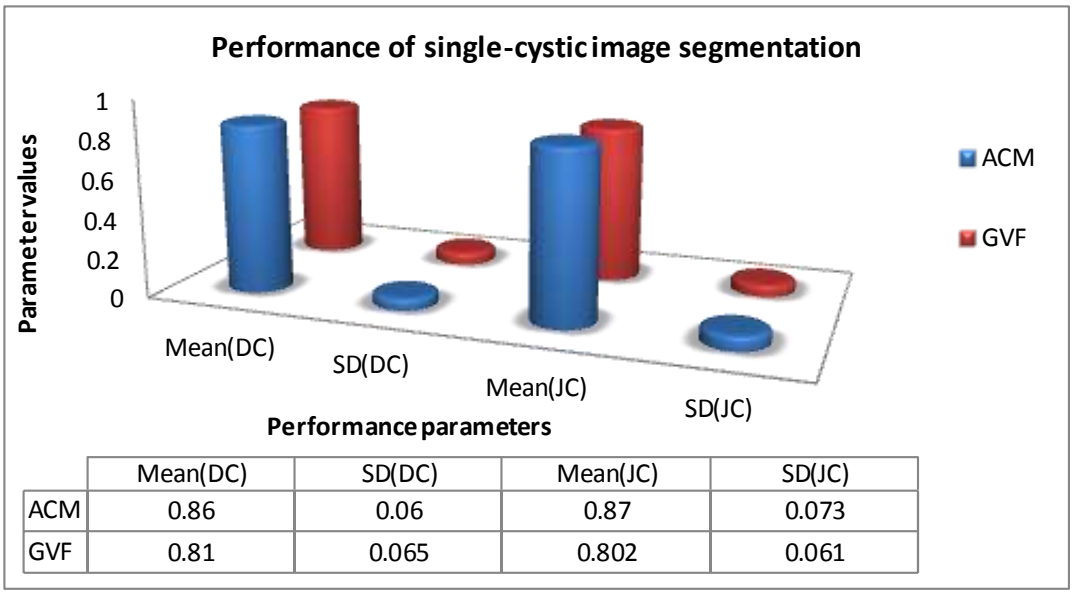


| | Mean(DC) | SD(DC) | Mean(JC) | SD(JC) |
|---|---|---|---|---|
| ACM | 0.86 | 0.06 | 0.87 | 0.073 |
| GVF | 0.81 | 0.065 | 0.802 | 0.061 |

Fig. 4.7 Performance analysis of single cyst segmentation in renal US images

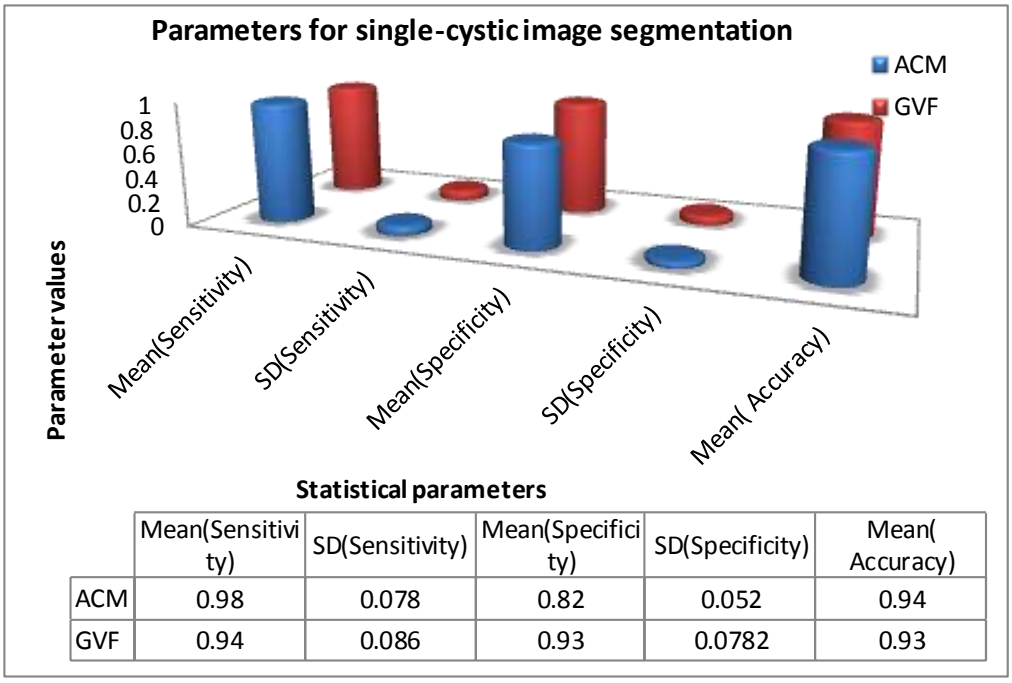


| | Mean(Sensitivity) | SD(Sensitivity) | Mean(Specificity) | SD(Specificity) | Mean( Accuracy) |
|---|---|---|---|---|---|
| ACM | 0.98 | 0.078 | 0.82 | 0.052 | 0.94 |
| GVF | 0.94 | 0.086 | 0.93 | 0.0782 | 0.93 |

Fig. 4.8 Statistical parameters of single cyst segmentation in renal US images

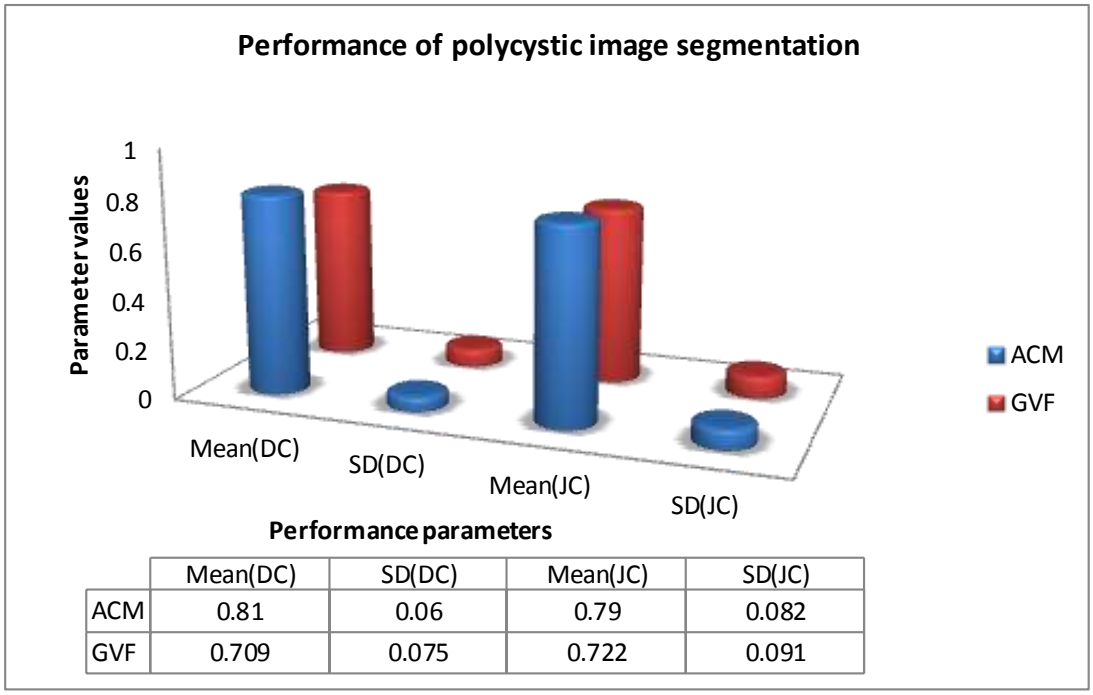


| | Mean(DC) | SD(DC) | Mean(JC) | SD(JC) |
|---|---|---|---|---|
| ACM | 0.81 | 0.06 | 0.79 | 0.082 |
| GVF | 0.709 | 0.075 | 0.722 | 0.091 |

Fig. 4.9 Performance analysis of polycysts segmentation in renal US images

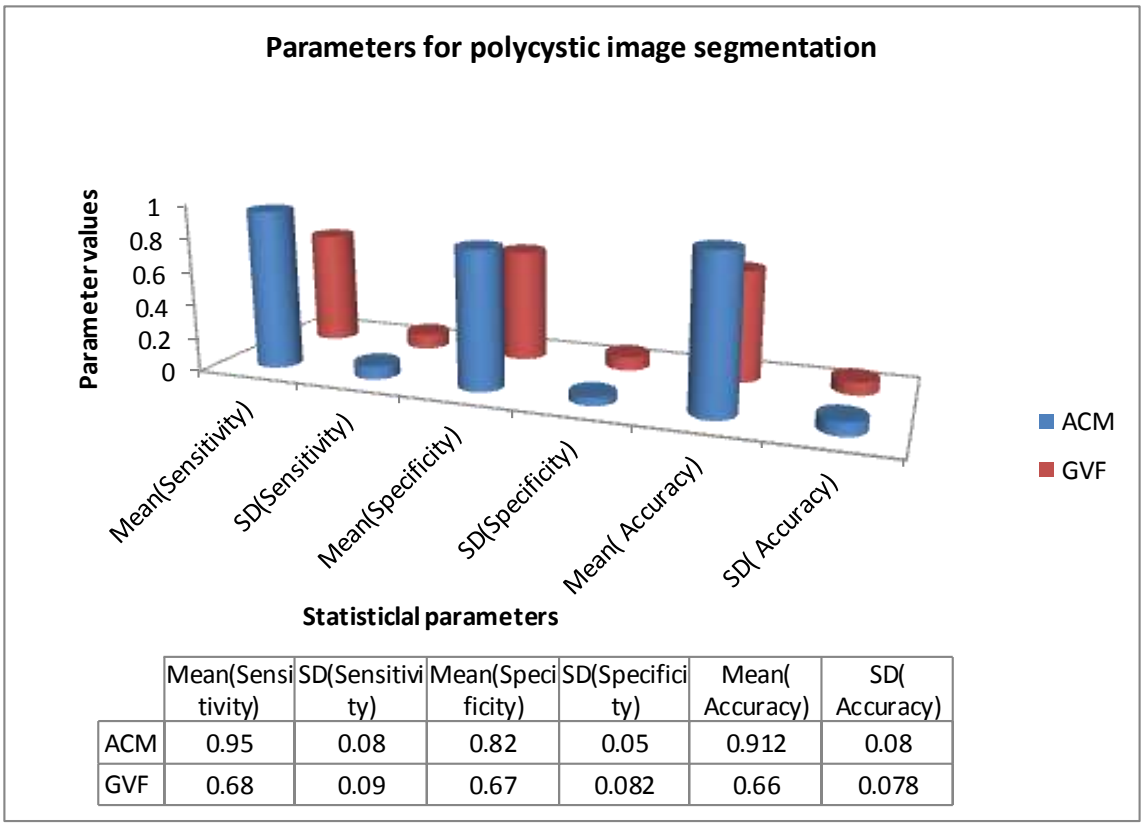


| | Mean(Sensitivity) | SD(Sensitivity) | Mean(Specificity) | SD(Specificity) | Mean( Accuracy) | SD( Accuracy) |
|---|---|---|---|---|---|---|
| ACM | 0.95 | 0.08 | 0.82 | 0.05 | 0.912 | 0.08 |
| GVF | 0.68 | 0.09 | 0.67 | 0.082 | 0.66 | 0.078 |

Fig. 4.10 Statistical parameters of polycysts segmentation in renal US images

Fig.4.9 and 4.10 show the plots of performance and statistical parameters for the segmentation of polycystic images. From Fig. 4.9 and Fig. 4.10, it is noticed that the performance is improved in the segmentation of polycystic images. The values of performance parameters DC, JC, sensitivity, specificity, and accuracy show the improvement in segmentation using the proposed ACM method compared to the GVF segmentation algorithm.

The ACM segmentation algorithm can be compared with the GVF algorithm as shown in Table 4.1. The mean values of DC, JC, and execution time for complete segmentation of single-cystic and polycystic images are shown in Table 4.1. The mean values of DC and JC are calculated by considering all the cystic images in both the datasets.

Table 4.1 Comparison of GVF and ACM method for segmentation of cysts in ultrasound images of kidney

| **Method** | **Image class** | **Performance parameter** | | **Average execution time for segmentation (in sec.)** |
|---|---|---|---|---|
| | | **Mean(DC)** | **Mean(JC)** | |
| ACM algorithm | Single-cystic | 0.86 | 0.87 | 8.25 |
| | Polycystic | 0.81 | 0.79 | 9.4 |
| GVF algorithm (Chapter 3) | Single-cystic | 0.81 | 0.802 | 9.6 |
| | Polycystic | 0.709 | 0.722 | 16.15 |

From Table 4.1, it is observed that the performance of segmentation is improved in the proposed ACM method compared to the GVF algorithm (discussed in Chapter 3) for the segmentation of single-cystic ultrasound images of the kidney. The amount of time taken for the segmentation of single-cystic images is comparatively less than that of segmentation cysts in polycystic images. Segmentation of polycystic image takes a larger initial contour and consumes more iterations to cover all the cysts. Hence, the execution time required is more in the case of polycystic kidney images.

As discussed in section 2.5 of Chapter 2, any standard method on the segmentation of cysts in US images of kidney is hardly found in the literature. It is observed that the fully automatic segmentation methods are also not available on imaging modalities like CT and MRI of the kidney. In (Sharma et al., 2017), authors have implemented the segmentation of

cysts using a convolution neural network on CT images of the kidney. In (Bae, et al., 2017), authors have used a semiautomatic method for kidney cysts segmentation in MRI images. Authors have used image editing software and the method is not fully automatic. However, the proposed ACM method is fully automated for the segmentation of cysts in kidney images.

## 4.5 Summary

In this Chapter, an automated ACM segmentation algorithm for the segmentation of cystic renal US images is proposed. The disadvantage of GVF based segmentation is resolved by completely avoiding the specification of initial parameters by the user. The initial contour needed by the ACM algorithm is effectively generated automatically using morphological operations. This reduces the burden and saves the time of medical experts to a greater extent avoiding manual annotation for every image. The efficiency of the algorithm is measured in two ways. One of the ways is comparing segmented images with manually marked images by the medical experts. The second way is verification using various performance parameters namely DC, JC, sensitivity, specificity, accuracy, and amount of time for execution. Thus proposed ACM based segmentation performs the segmentation of single-cystic images effectively. The performance of the proposed ACM based segmentation is better than GVF based segmentation.

Initial contour cannot be generated for ultrasound images of renal stones using morphological operations. Hence, the automatic segmentation of stones in ultrasound images of the kidney is not effectively performed. ACM method is unable to segment individual cysts in the polycystic US image of the kidney rather it segments the image into a single region containing all the cysts. Further, there is a need for improvement in the segmentation of polycystic kidney image and is discussed in subsequent chapters.

# Chapter 5

# AUTOMATIC SEGMENTATION OF CYSTS AND STONES IN ULTRASOUND IMAGES OF KIDNEY USING LEVEL SET METHOD

## 5.1 Introduction

The purpose of segmentation is to find the distinct regions within an image. In region-based algorithms, the pixels are grouped, based on their intensities. Generally, the pixels with similar intensity are distributed equally. Hence, the edge-based method is more appropriate than its region-based version. In the case of the level set, the contour deforms progressively considering the variance among neighborhood pixel values. This is employed through the partial differential equations. The level set method has many benefits compared to other methods such as ACM. The level set can effectively handle the complex contours as well. One more added benefit is that it performs contour merge and split automatically unlike ACM (Sussman M., Smereka P., and Osher S., 1994). It uses a cartesian grid for computation without the necessity of contour points. This algorithm works based on choosing a surface instead of the front. The front is specified with the pixels having no surface height.

Basically level set uses sign-magnitude for segmentation of the regions. The boundary is specified using the continuity points (Li C., Xu C., Gui C., and Fox M. D., 2010). The basic method does not segment all the images accurately as it uses the unbalanced level set function (LSF). The irregular LSF sometimes leads to wrong results during the evolution of

---

[1] Akkasaligar Prema T., Biradar Sunanda, "Automatic Kidney Cysts Segmentation in Digital Ultrasound Images", In: Shukla A. (ed.), Chapter 4, Medical Imaging Methods. Springer, Singapore, 2019, pp. 97-117.

[2] Akkasaligar Prema T., Biradar Sunanda, "Segmentation of kidney stones in medical ultrasound images", Recent Trends in Image Processing and Pattern Recognition, RTIP2R 2018, Communications in Computer and Information Science, vol. 1036, part 2, Springer Nature Singapore Ple. Ltd. 2019, pp. 200-208.

[3] Akkasaligar Prema T., Biradar Sunanda, "Automatic Segmentation and Analysis of Renal Calculi in Medical Ultrasound Images", Pattern Recognition and Image Analysis, vol. 30(4), 2020 (under press).

contour. The limitation of irregular LSF is resolved through reinitializing LSF during evolution (Li C., Xu C., Gui C., and Fox M. D., 2010). It is enhanced by using a distance regularization term for controlling the evolution accurately (Osher S. and Fedkiw, 2002). It also uses a sign-magnitude. An edge-based method using distance regularization LSF is used for the segmentation of cysts in renal US images.

As discussed in the previous chapter, the fully automatic segmentation of stones in ultrasound images of the kidney is not performed. Because initial contour generation for segmentation of stones in ultrasound images of the kidney using morphological operations is not effective. Further, the improved performance in the segmentation algorithm is an essential need.

Chapter 5 discusses the automatic segmentation of cysts and stones from denoised renal US images. This chapter elaborates the algorithms for automatic generation of initial contour, effective use of a level set algorithm, results obtained, performance evaluation, and analysis.

The proposed algorithm uses a LSF having a signed distance function indicating abortion and/or continuation of the deformation.

## 5.2 Proposed method

Medical image analysis can be broadly classified into completely automated methods and semiautomatic methods. The automated approach for medical image interpretation is highly accepted. Even though it is difficult to achieve but, it has many benefits. The benefits are increased speed, increased accuracy, consistent, and easily reproducible. On the other hand, semiautomatic approaches need manual effort through interactive inputs or editing by the clinician. The segmentation of cysts and stones from the renal US image is made completely automatic by specifying a method for the generation of initial contour. It prevents the labor-intensive work needed by the medical expert.

### 5.2.1 Automatic initial contour generation for segmentation of cysts

Morphological operations can be effectively used in the field of image processing for many applications. These operations are used for the generation of initial contour as well. The method specified in Algorithm 4.1 of Chapter 4 is used for the detection of initial contour for the level set method as well. Algorithm 4.1 results in an automatic initial contour that can be

used effectively to segment the single and multiple cysts in renal US images. For a single-cystic image, a single region containing cyst is obtained and is used as an automatic initial contour by a level set based method. In the case of polycystic kidney image, multiple cystic regions are extracted after applying algorithm 4.1. These all regions are taken as initial contour by level set based segmentation method for simultaneous deformation of all the cystic regions.

As discussed in Algorithm 4.1of Chapter 4, the empirically determined initial contours in the image are greater than M1 and M2 pixels are used for segmentation of single-cystic and polycystic images of the kidney.

### 5.2.2 Automatic initial contour generation for segmentation of stones

Renal calculi can have varying sizes. They can be as tiny as 1mm. Morphological operations based methods are not suitable for segmenting the stones. Because the stones of smaller sizes are filled, assuming them as holes and the stone ROI to be segmented is not retained during the process of initial contour detection.

It is generally observed that the renal calculi are not located in the upper part and corners of the US images. Hence a larger rectangle leaving the corners, lying in the center, is taken as an initial contour for segmentation algorithm is shown in Fig 5.1. The sections of the image bordered with red color are the regions in the US image not containing the stone. The pixel coordinates of the X-axis for the rectangle of the initial contour are computed using Eqs. 5.1 and 5.2. The Y coordinates of the rectangle corner are computed using Eqs. 5.3 and 5.4.

$$x_1 = \frac{m}{6} \tag{5.1}$$

$$x_2 = \frac{5*m}{6} \tag{5.2}$$

$$y_1 = \frac{n}{6} \tag{5.3}$$

$$y_2 = \frac{5*n}{6} \tag{5.4}$$

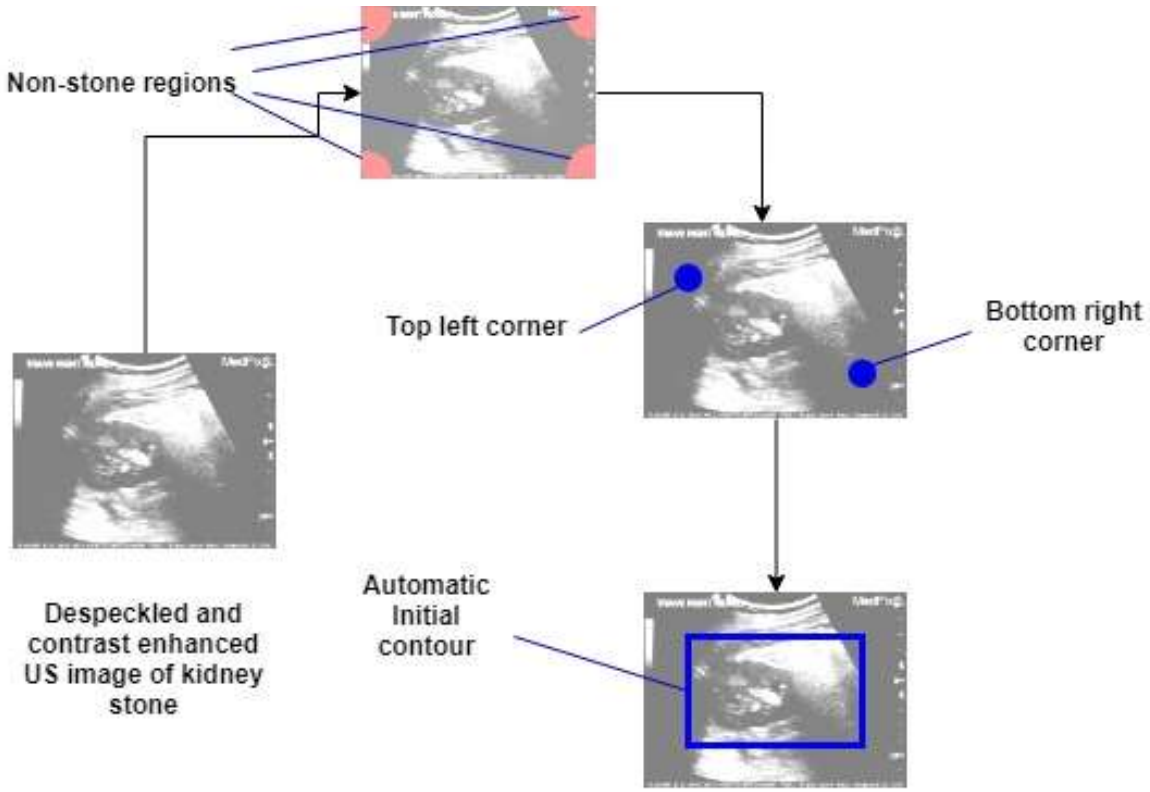


Fig. 5.1. Generation of automatic initial contour for renal calculus US image

The variables m and n represent the number of rows and columns of the image respectively. The different stages followed in the calculation of initial contour detection are shown in Algorithm 5.1.

**Algorithm 5.1: Generation of automatic initial contour for stones**

*Input:* Despeckled renal US image (S).

*Output:* Initial contour generated with the corners ($x_1$, $y_1$) and ($x_2$,$y_2$).

*Begin*

*Step 1:* Read the denoised renal US image S.

*Step 2:* Determine the image size (m, n).

*Step 3:* Compute the x-coordinate($x_1$) of the upper corner of the initial contour rectangle, by equating it to one-sixth of the width 'm' as mentioned in Eq. (5.1).

*Step 4:* Compute the x-coordinate(x2) of the bottom-right corner of the initial contour rectangle, subtracting one-sixth of the 'm' from the width of the image as mentioned in Eq. (5.2).

*Step 5:* Find the y- coordinate ($y_1$), of the upper corner of the initial contour rectangle, by equating one-sixth of 'n' to it as mentioned in Eq. (5.3).

*Step 6:* Find the y- coordinate($y_2$), of the bottom corner of the initial contour rectangle, by subtracting one-sixth of 'n' from the 'n' as mentioned in Eq. (5.4).

*Step 7:* The resultant coordinates ($x_1$, $y_1$) and ($x_2$, $y_2$) are used as the top left and bottom right corners of the initial contour rectangle respectively.

*End.*

Thus, the pixel coordinates ($x_1$, $y_1$) and ($x_2$, $y_2$) represent the endpoints for the initial contour rectangle. The larger rectangle of the initial contour is used for the level set segmentation of kidney stones to get the nearest and approximate ROI for the stone. The output of the first time application of the level set algorithm is used for calculation of the initial contour rectangle for by the level set method for the second time. The minimum and maximum X-Y coordinates of the first time segmented output is used to determine the initial contour rectangle. Thus the selection of initial contour for stones in US images of the kidney is automated completely.

### 5.2.3 Segmentation of cysts and stones

All the renal US images of cystic and stone type in both the datasets S1 and S2 specified in section 1.5 of Chapter 1 are used for experimentation. The level set method can be effectively used for the segmentation of cysts and stones. The different steps of the level set are described in Algorithm 5.2.

**Algorithm 5.2: Level set segmentation method**.

*Input:* Renal cystic or stone US image having initial contour (A).

*Output:* Segmented renal cystic or stone image.

*Begin*

*Step 1:* Apply the Gaussian kernel function to get a smoothened image.

*Step 2:* Partial differentiation is carried out on the edge indicator of the smoothened image.

*Step 3:* Find the distance regularization term using Eq. (5.7).

*Step 4:* Calculate Dirac delta and Heaviside functions.

*Step 5:* Obtain the energy function using the parameters obtained in *Step 3* and *Step 4*.

*Step 6:* Perform the deformation until the curve obtained in *Step 5* is changed (i.e. it has zero-crossing points) or until the number of iterations are exhausted.

*Step 7:* Return the segmented output image or return to *Step 2*.

*End*.

The evolution of the initial contour depends on the energy function. The energy function is computed using external energy and distance regularization term as shown in Eq. (5.5). Calculation of external energy and term for distance regulation is carried out using Eq. (5.6) and Eq. (5.7). External energy depends on the input. μ is a constant with a value greater than zero. L(ɵ) and A(ɵ) use an energy coefficient α larger than zero. These functions are defined as in Eq. (5.8) and Eq. (5.9). Here, 'del' represents the Dirac delta function and 'Hs' represents the Heaviside function. L(ɵ) defines the energy of line integral of a smoothened image along initial zero level contour. A(ɵ) is a weighted area of the region. The weighted area helps to enhance the speed of the contour evolution.

$$E(ɵ)=\mu R_{x(}ɵ)+E_{ex}(ɵ) \tag{5.5}$$

$$E_{ex}(ɵ)=\lambda L(ɵ)+\alpha A(ɵ) \tag{5.6}$$

$$R_x(ɵ)= \int X(|\nabla ɵ |)\ \Omega du \tag{5.7}$$

$$L(ɵ) \triangleq \int_{\Omega}^{x} s.\,del(ɵ)\,\nabla ɵ du \tag{5.8}$$

$$A(ɵ) \triangleq \int_{\Omega}^{x} s.\,Hs(-ɵ)du \tag{5.9}$$

The sign-magnitude associated with the distance regularization term (DRT) of the initial curve decides about the expansion and contraction of the curve. If the sign of DRT is positive the deforming curve grows expanding its size and if it is negative then the curve is

contracted during deformation. The initial sign-magnitude for DRT is positive during the segmentation of the renal cystic US image. Because the initial contour generated for cystic images is smaller in size than the actual cyst size.

In the case of single-cystic kidney images a single region generated by Algorithm 4.1 is used as an automatic initial contour by a level set algorithm for further deformation. However, Algorithm 4.1 generates multiple initial contours for polycystic kidney images. All these regions are deformed simultaneously to get the desired ROI of multiple cysts using a proposed level set based segmentation algorithm.

In the case of renal stone segmentation process, the initial sign-magnitude for DRT is negative as the generated initial contour for the renal calculus image is a larger rectangle. However, during the further stages of deformations, sign of the DRT image can be changed and accordingly the curve is expanded or reduced. Hence, the DRT plays a vital role in regulating the shape and size of a deforming curve. Thus, a level set algorithm can be effectively used in the segmentation of cysts and stones in US images of the kidney.

The stopping criteria for the deformation are: either the pre-specified iterations have exhausted or when no changes are observed in the curve obtained in the previous step and the curve obtained in the current step.

## 5.3 Experimental Results and Discussion

The experimentation is performed on all 185 US images of the kidney, cysts, and stones. The dataset specified in section 1.5 contains the clinical (S1) and web (S2) datasets, comprising of 37 normal kidney images, 39 single-cystic, 35 polycystic, 38 single-stone, and 36 multiple-stones images altogether. The algorithm is implemented on Intel core i5 processor with 4GB RAM @ 2.5GHz, using MATLAB 7.11. The denoising of images is carried out using contourlet transform as discussed in section 3.3.1 of Chapter 3.

The denoised image is binarized to apply morphological operations. Fig. 5.2((a) to (d)) shows the sample images of single-cystic, polycystic, single-stone, and multiple-stones renal US images respectively.

Algorithm 4.1 of Chapter 4 is applied to a single cystic image specified in Fig. 5.2 (a), to get the automatic initial contour for level set segmentation as shown in Fig. 5.3(a). The segmented region after complete deformation is shown in Fig. 5.3(c). The nature of LSF at the initial level and after complete evolution is shown in Fig. 5.3(b) and Fig. 5.3(d) respectively. The deformation is completed in 305 iterations for this particular example. However, the numbers of iterations vary based on the input image. The size of the cyst is determined as 27.6 $mm^2$ by using the Eq. (4.1). The size specified by a medical expert is 28.2 $mm^2$.

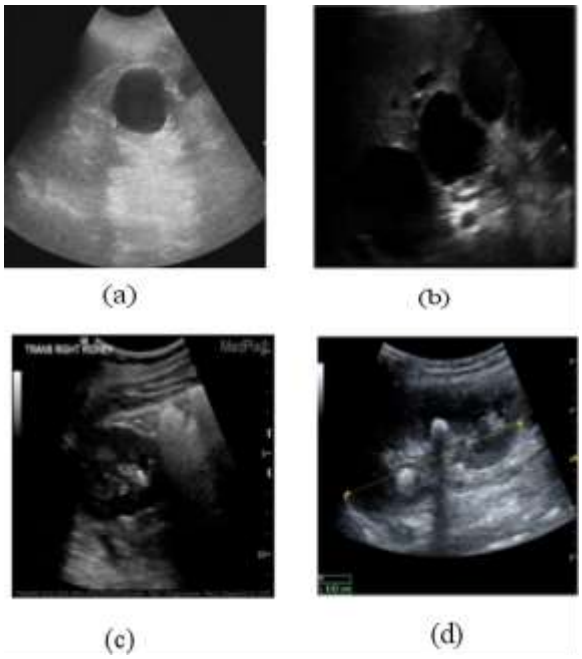


Fig. 5.2. Sample images: (a) Single-cystic renal US image (b) Polycystic renal US image (c) Single renal calculus US image (d) Multiple-stones renal US image

The multiple initial contours generated automatically for a polycystic renal US image using Algorithm 4.1 is shown in Fig. 5.4(a). All the regions deform simultaneously resulting in multiple cystic regions. The segmented polycystic region after complete deformation is shown in Fig. 5.4(c). The nature of LSF at the initial level and after complete evolution is shown in Fig. 5.4(b) and Fig. 5.4(d) respectively. The deformation is completed in 322 iterations for this particular example. The segmented output is binarized to obtain the number of stones and their sizes as discussed in section 4.3 of Chapter 4. For this particular sample image, number of cysts is computed as 4. The sizes of the cysts are computed as 35.4 $mm^2$, 33.5$mm^2$, 22.3$mm^2$, and 11.2$mm^2$ by using the Eq. (4.1). The sizes of the cysts specified by a medical expert are computed as 35.9 $mm^2$, 33$mm^2$, 21.7$mm^2$, and 11.6$mm^2$. A smaller

relative error is observed in the values. Thus complete automatic segmentation of cysts in medical US images of the polycystic kidney is performed successfully using the level set method.

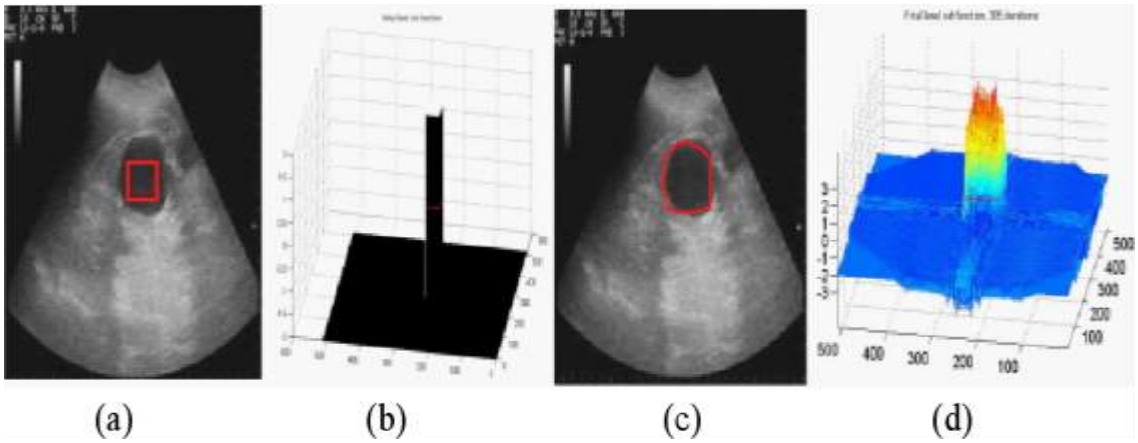


Fig. 5.3. Segmentation of single-cystic image : (a) Image with initial contour (b)Nature of LSF at initial stage (c) Finally deformed image at the end of 305 iterations (d) Nature of LSF at the end of deformation

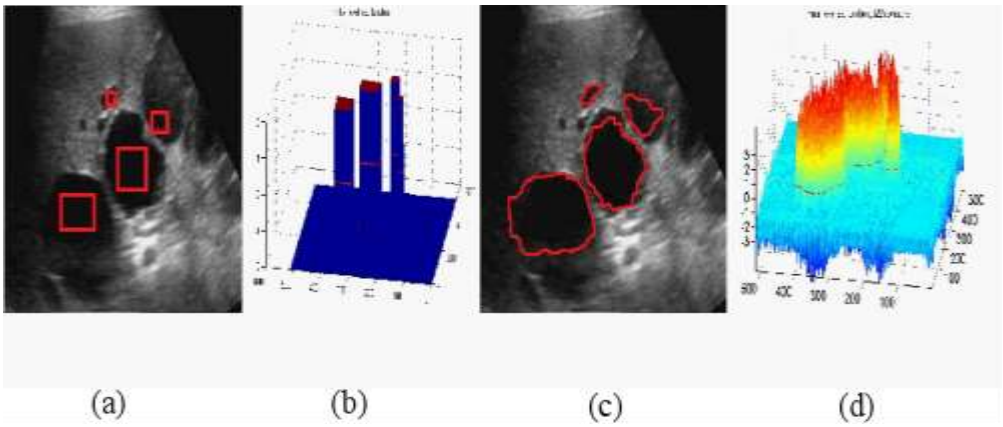


Fig. 5.4. Segmentation of polycystic image : (a) Image with initial contour (b)Nature of LSF at initial stage (c) Finally deformed image at the end of 322 iterations (d) Nature of LSF at the end of deformation

| Image class | Input US image | Segmentedimage by proposed level set method | Manually annotated image by a medical expert | Results |
|---|---|---|---|---|
| Single cystic | 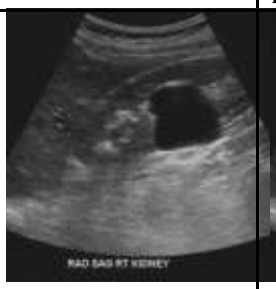 | 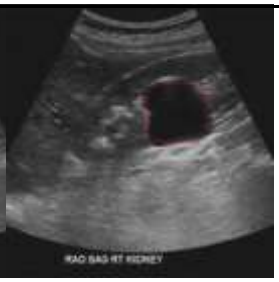 | 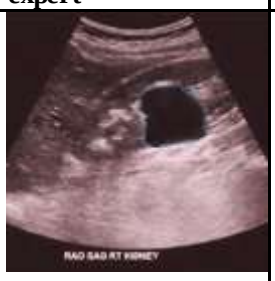 | DC=0.947<br>JC=0.951<br>Sensitivity=0.951<br>Specificity=0.958<br>Accuracy=0.964<br>Cyst size= 31.4mm$^2$ |
| Single cystic | 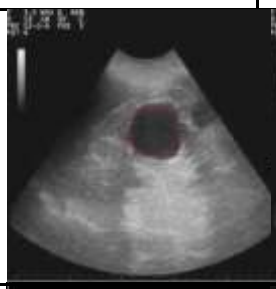 | 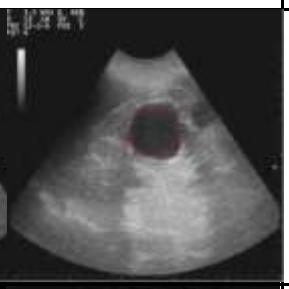 | 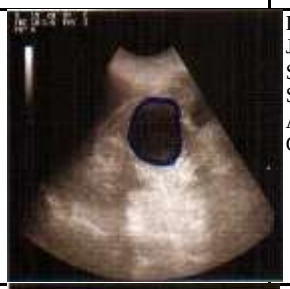 | DC=0.967<br>JC=0.971<br>Sensitivity=0.978<br>Specificity=0.972<br>Accuracy=0.975<br>Cyst size= 27.6mm$^2$ |
| Polycystic | 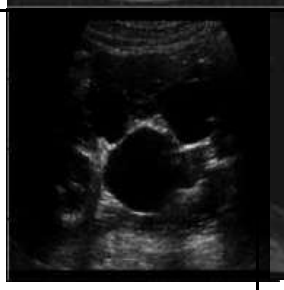 | 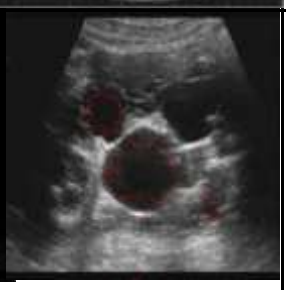 | 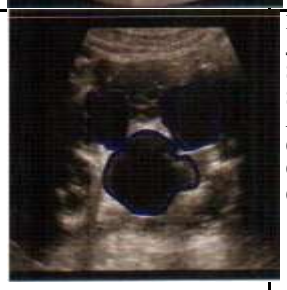 | DC=0.817<br>JC=0.812<br>Sensitivity=0.821<br>Specificity=0.819<br>Accuracy=0.823<br>Cyst1 size= 25.3mm$^2$<br>Cyst2 size= 26.1mm$^2$<br>Cyst3 size= 33.2mm$^2$ |
| Polycystic | 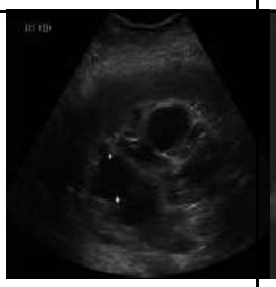 | 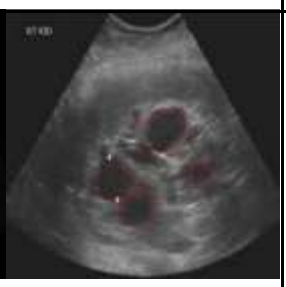 | 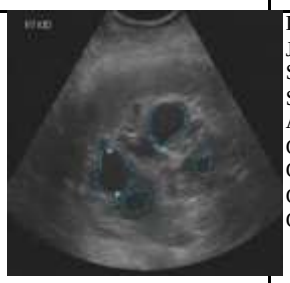 | DC=0.913<br>JC=0.917<br>Sensitivity=0.916<br>Specificity=0.923<br>Accuracy=0.927<br>Cyst1 size= 24.2mm$^2$<br>Cyst2 size= 26.3mm$^2$<br>Cyst3 size= 20.2mm$^2$<br>Cyst4 size= 21.8mm$^2$ |
| Polycystic | 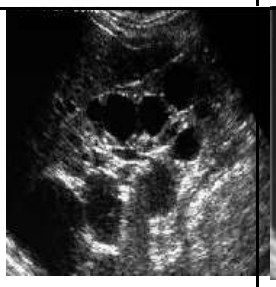 | 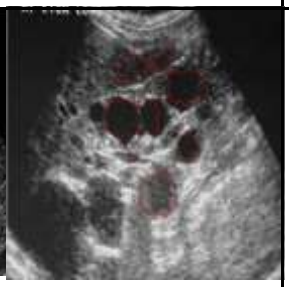 | 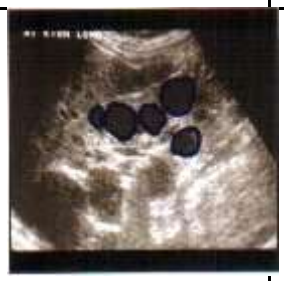 | DC=0.783<br>JC=0.782<br>Sensitivity=0.809<br>Specificity=0.806<br>Accuracy=0.799<br>Cyst1 size= 19.4mm$^2$<br>Cyst2 size= 15.3mm$^2$<br>Cyst3 size= 21.7mm$^2$<br>Cyst4 size= 28.2mm$^2$<br>Cyst5 size= 13.4mm$^2$<br>Cyst6 size= 23.2mm$^2$ |

Fig. 5.5. Results of segmentation of cysts in kidney US images using a level set

Experimentation is carried out on all cystic images specified in section 1.5 of Chapter1. Some of the sample outputs are shown in Fig. 5.5. From Fig. 5.5, it is observed that the

relative error in the segmentation of individual cyst in single-cyst and, polycystic images is improved. There is a good agreement between experimentally segmented images and manually annotated images by medical experts.

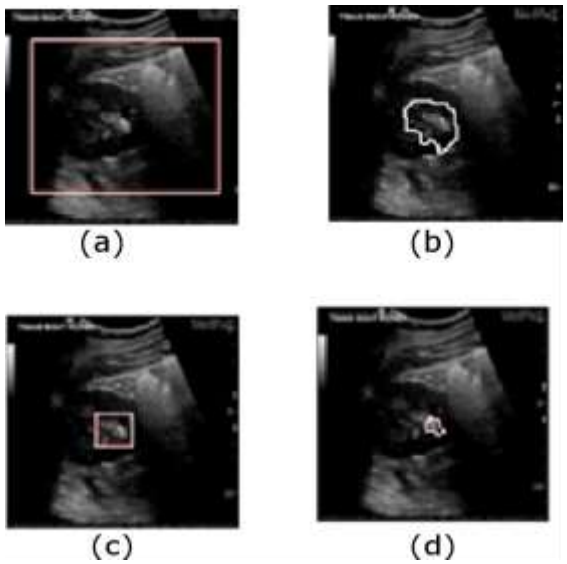


Fig. 5.6. Segmentation of single-stone image : (a) Automatic initial contour at the first time application of level set (b) Final segmented contour at the end of the first time application after 300 iterations (c) Refined initial contour for the second time application of level set (d) Final segmented contour at the end of the second time application after 165 iterations

Algorithm 5.2 is used for automatic initial contour selection for renal calculus stone in US images. In the first time application, a larger rectangle of the initial contour is generated automatically using Algorithm 5.1, as shown in Fig. 5.6(a). Segmented contour obtained at the end of the first time application of the level set method is shown in Fig.5.6 (b). For the sample image of renal calculus, it takes 300 iterations in the proposed level set algorithm. From Fig.5.6 (b), the initial contour for the second run of level set is obtained by finding the minimum and maximum of X-Y coordinates. This contour is shown in Fig 5.6 (c). It is considered as a final initial contour generated automatically.

The level set method is applied for the second time taking Fig. 5.6(c) as an initial contour for further evolution. This extracts the more refined contour of ROI as shown in Fig. 5.6(d) resulting in accurate segmentation of stones. For the considered example, level set evolution is completed in 165 iterations. Only one stone is identified, as a single segmented region is found. The computation of the number of stones and their size are carried out by binarizing the segmented output as discussed in section 4.3 of Chapter 4. The size of the stone is

computed as 11.54 $mm^2$ and the value mentioned by a medical expert is 10.75 $mm^2$. A smaller relative error is observed in the experimentally obtained value.

As observed, the level set needs more number of iterations at the first time application of level set segmentation. This is because of the larger initial rectangle. The number of iterations are reduced considerably during the second time. Thus, the proposed algorithm successfully deforms to the ROI of stone, locating, and marking the stone more accurately.

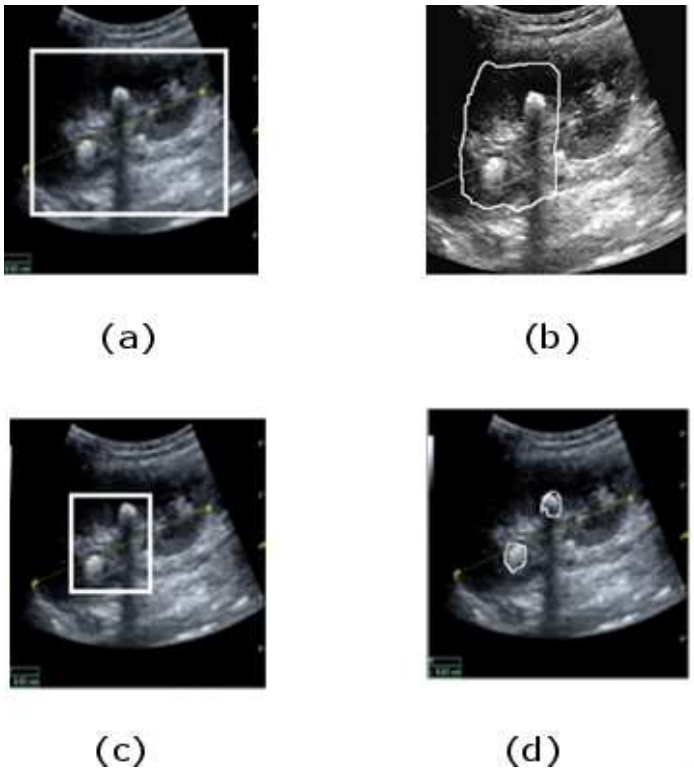


Fig. 5.7. Segmentation of multiple-stones image : (a) Initial contour at first time application of level set (b) Final segmented contour at the end of the first time application after 224 iterations (c) Refined initial contour for the second time application of level set (d) Final segmented contour at the end of the second time application after 162 iterations

Similar to single-stone, the multiple-stones renal image can be segmented effectively as shown in Fig. 5.7. The first larger initial contour is obtained automatically by applying Algorithm 5.1 as shown in Fig. 5.7(a). The deformed contour at the end of the first time application of level set based segmentation is shown in Fig. 5.7 (b). The level set uses 224 iterations to obtain the contour shown in Fig. 5.7 (b). The refined contour is obtained by finding minimum and maximum X-Y coordinates of the contour obtained in Fig. 5.7(b) is shown in Fig. 5.7 (c).

| Image class | Input US image | Segmented image by proposed level set method | Manually annotated image by a medical expert | Results |
|---|---|---|---|---|
| Single stone | 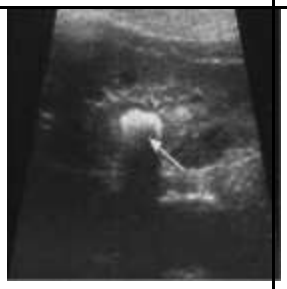 | 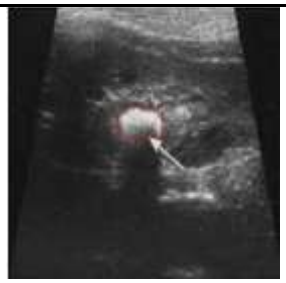 | 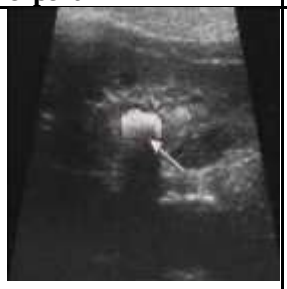 | DC=0.952<br>JC=0.9541<br>Sensitivity=0.971<br>Specificity=0.968<br>Accuracy=0.969<br>Stone size= 14.69mm$^2$ |
| Multiple -stones | 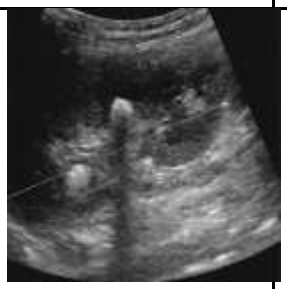 | 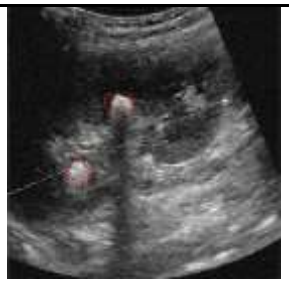 | 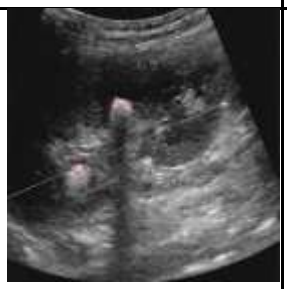 | DC=0.968<br>JC=0.969<br>Sensitivity=0.982<br>Specificity=0.986<br>Accuracy=0.984<br>Stone1 size= 13.92mm$^2$<br>Stone2 size= 11.43mm$^2$ |
| Multiple -stones | 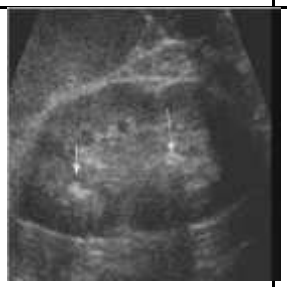 | 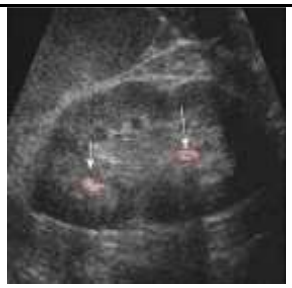 | 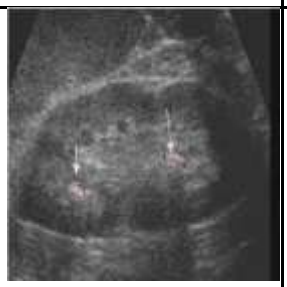 | DC=0.934<br>JC=0.937<br>Sensitivity=0.934<br>Specificity=0.945<br>Accuracy=0.9388<br>Stone1 size= 7.67mm$^2$<br>Stone2 size= 7.73mm$^2$ |
| Single stone | 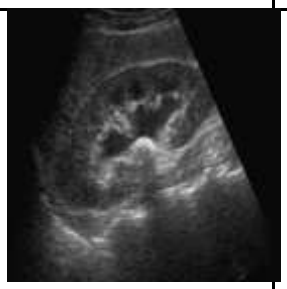 | 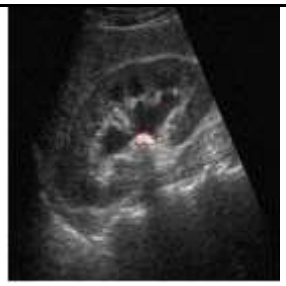 | 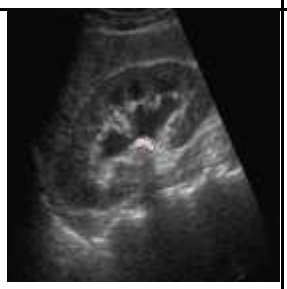 | DC=0.963<br>JC=0.967<br>Sensitivity=0.964<br>Specificity=0.958<br>Accuracy=0.962<br>Stone size= 12.82mm$^2$ |

Fig. 5.8. Results of kidney stones segmentation using the level set method

Fig. 5.7 (c) is used as an initial contour by the level set algorithm to get the more refined ROI of stones. The single initial contour is divided into multiple regions automatically based on the textural properties of the pixels in the image by level set based segmentation algorithm. This property of a level set algorithm is effectively used to individually segment the multiple-

stones present in the kidney US image. Finally, segmented stones by second-time application of the level set are shown in Fig. 5.7 (d). The number of iterations taken by level set for the second time is 162. The sizes of the stones are computed as 13.92 $mm^2$ and 11.43 $mm^2$ from the segmented kidney stone image. The sizes of the stones annotated by a medical expert are 13.21 $mm^2$ and 11.9 $mm^2$ respectively. A smaller relative error is observed in the experimentally obtained values.

Experimentation is carried out on all kidney stone images specified in section 1.5 of Chapter1. Some of the sample outputs for renal calculi images are shown in Fig. 5.8. From Fig. 5.8, it is observed that there is a good resemblance between experimentally segmented images and manually annotated images by medical experts.

The statistical acceptance of the experimentally obtained values is performed using the chi-square test. The details are shown in Appendix III. Thus, the proposed level set method segments the cysts and stones automatically and effectively. It is capable of segmenting individual cysts/stones in the case of the polycystic and multiple-stones US images respectively.

## 5.4 Performance evaluation

The performance of the segmentation is performed using the parameters Dice coefficient, Jaccard coefficient, sensitivity, specificity, and accuracy as discussed in section 1.7.5 of Chapter 1. The mean and standard deviation are computed by considering all the images in S1 (clinical) and S2 (web) datasets. The results obtained for level set segmentation of single and polycystic renal US images are compared with the ACM method (discussed in Chapter 4) using the plots in Fig. 5.9, Fig. 5.10, Fig. 5.11 and Fig. 5.12 respectively.

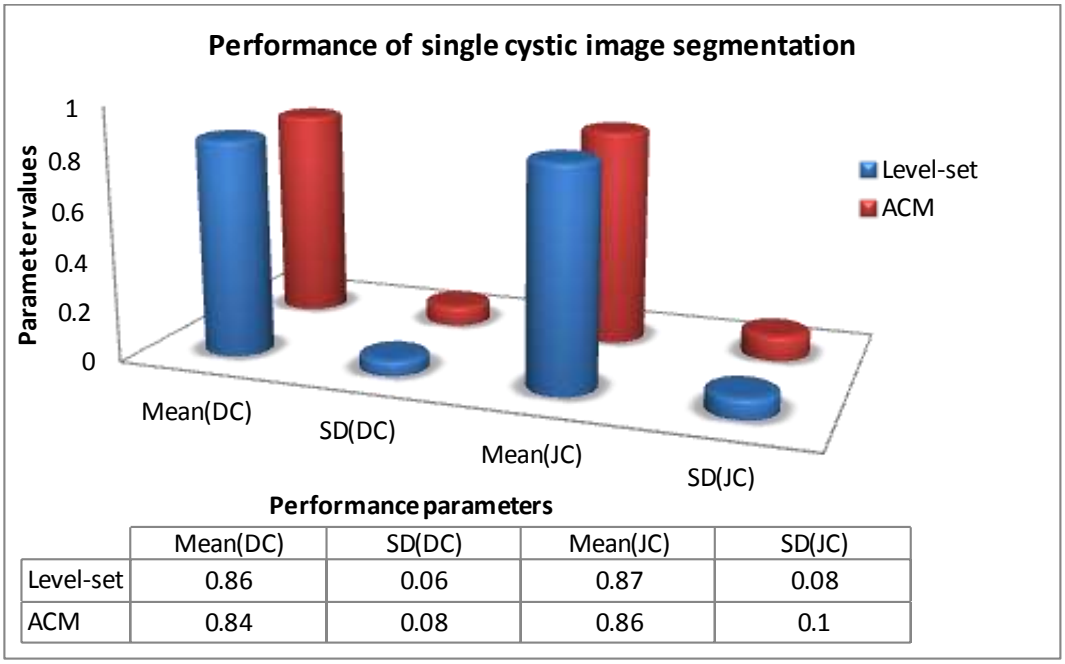


| | Mean(DC) | SD(DC) | Mean(JC) | SD(JC) |
|---|---|---|---|---|
| Level-set | 0.86 | 0.06 | 0.87 | 0.08 |
| ACM | 0.84 | 0.08 | 0.86 | 0.1 |

Fig. 5.9. Performance parameters of single cyst segmentation in renal US images

Obtained values in the plots of Fig 5.9 and Fig 5.10 show the improved accuracy in the proposed level set method over ACM based segmentation in terms of DC, JC, sensitivity, specificity, and accuracy for segmentation of single cystic US images of the kidney.

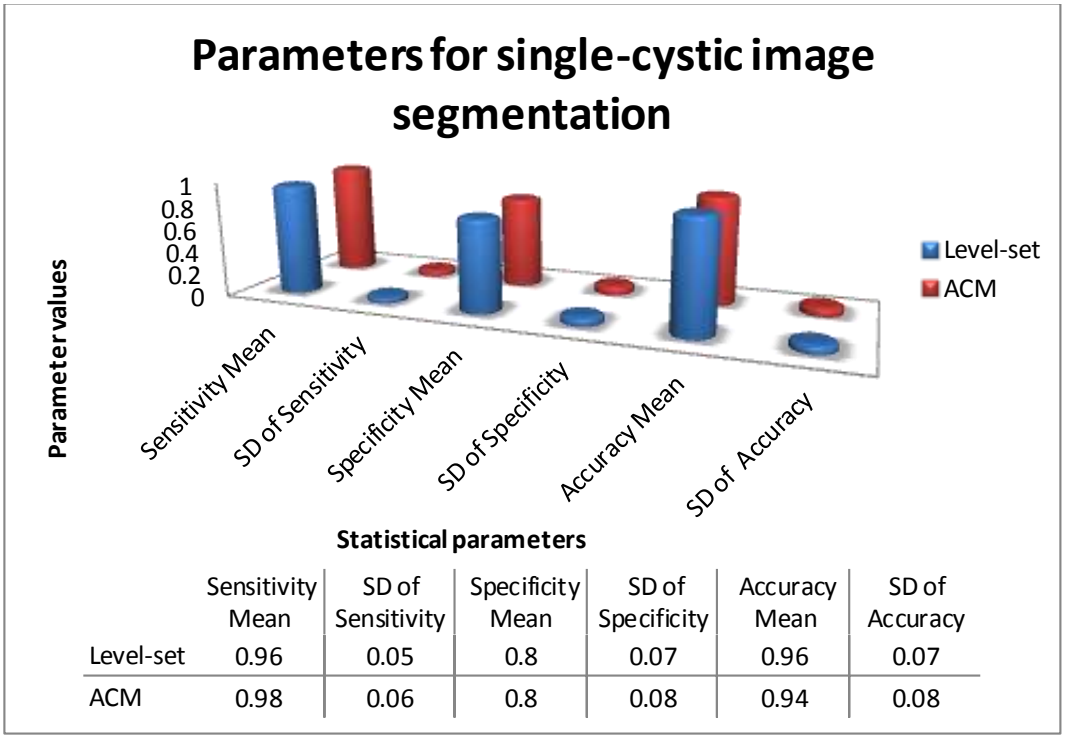


| | Sensitivity Mean | SD of Sensitivity | Specificity Mean | SD of Specificity | Accuracy Mean | SD of Accuracy |
|---|---|---|---|---|---|---|
| Level-set | 0.96 | 0.05 | 0.8 | 0.07 | 0.96 | 0.07 |
| ACM | 0.98 | 0.06 | 0.8 | 0.08 | 0.94 | 0.08 |

Fig. 5.10.Statistical parameters of single cyst segmentation in renal US images

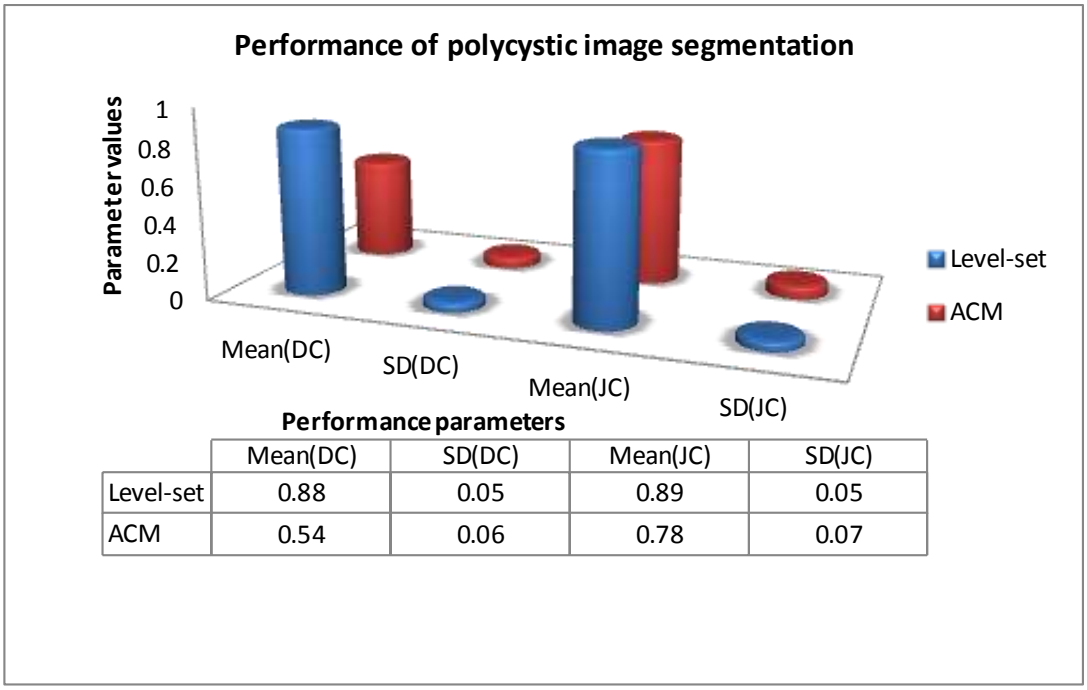


| | Mean(DC) | SD(DC) | Mean(JC) | SD(JC) |
|---|---|---|---|---|
| Level-set | 0.88 | 0.05 | 0.89 | 0.05 |
| ACM | 0.54 | 0.06 | 0.78 | 0.07 |

Fig. 5.11. Performance parameters of polycysts segmentation in renal US images

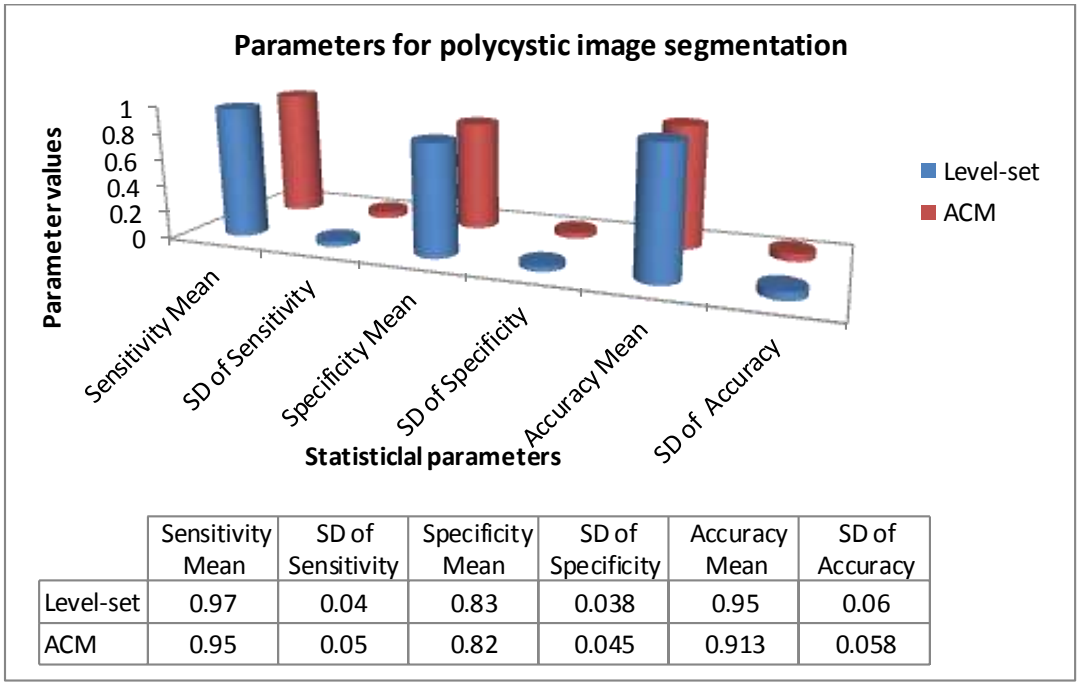


| | Sensitivity Mean | SD of Sensitivity | Specificity Mean | SD of Specificity | Accuracy Mean | SD of Accuracy |
|---|---|---|---|---|---|---|
| Level-set | 0.97 | 0.04 | 0.83 | 0.038 | 0.95 | 0.06 |
| ACM | 0.95 | 0.05 | 0.82 | 0.045 | 0.913 | 0.058 |

Fig. 5.12. Statistical parameters of polycysts segmentation in renal US images

From Fig 5.11 and Fig 5.12, it is observed that the proposed level set method results in more accurate segmentation of cysts in polycystic kidney US images.

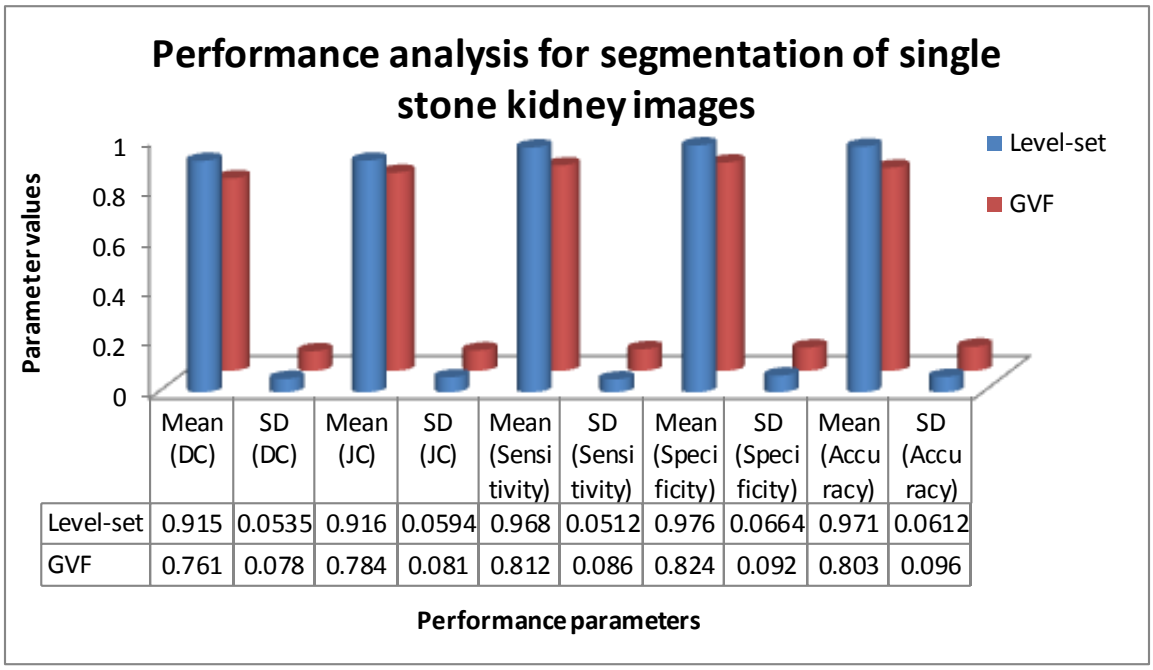


| | Mean (DC) | SD (DC) | Mean (JC) | SD (JC) | Mean (Sensitivity) | SD (Sensitivity) | Mean (Specificity) | SD (Specificity) | Mean (Accuracy) | SD (Accuracy) |
|---|---|---|---|---|---|---|---|---|---|---|
| Level-set | 0.915 | 0.0535 | 0.916 | 0.0594 | 0.968 | 0.0512 | 0.976 | 0.0664 | 0.971 | 0.0612 |
| GVF | 0.761 | 0.078 | 0.784 | 0.081 | 0.812 | 0.086 | 0.824 | 0.092 | 0.803 | 0.096 |

Fig. 5.13. Performance analysis for segmentation of single stone kidney images

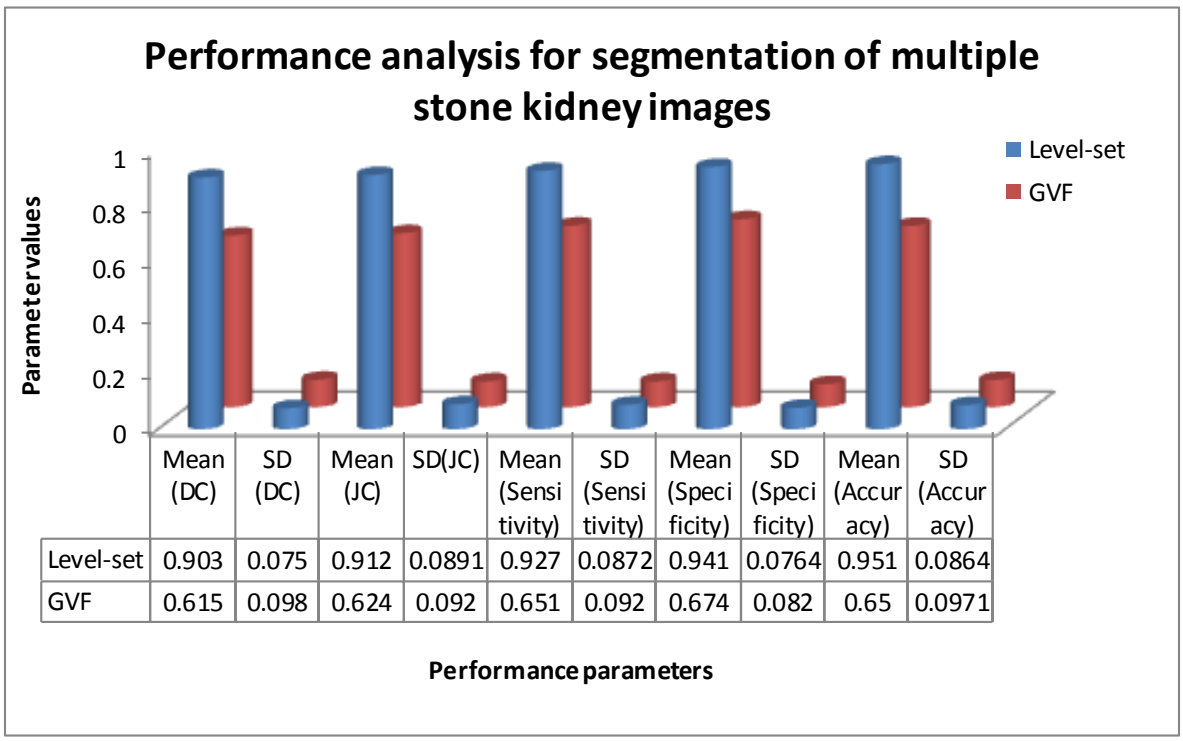


| | Mean (DC) | SD (DC) | Mean (JC) | SD(JC) | Mean (Sensitivity) | SD (Sensitivity) | Mean (Specificity) | SD (Specificity) | Mean (Accuracy) | SD (Accuracy) |
|---|---|---|---|---|---|---|---|---|---|---|
| Level-set | 0.903 | 0.075 | 0.912 | 0.0891 | 0.927 | 0.0872 | 0.941 | 0.0764 | 0.951 | 0.0864 |
| GVF | 0.615 | 0.098 | 0.624 | 0.092 | 0.651 | 0.092 | 0.674 | 0.082 | 0.65 | 0.0971 |

Fig. 5.14. Performance analysis for segmentation of multiple-stones kidney images

Fig. 5.13 and Fig. 5.14 show the comparison of the different parameters obtained for the proposed level set and GVF based segmentation of single and multiple-stones from the

ultrasound images of the kidney respectively. The obtained values show that the proposed level set method is more accurate than the GVF method using various parameters namely, DC, JC, sensitivity, specificity, and accuracy. Thus, from Figs. 5.9 to 5.14, it is found that the proposed level set based method performs fully automatic segmentation of cysts and stones successfully in US images of the kidney.

Table 5.1. Comparison of execution time in seconds for proposed level set method.

| **Method** | **Single-cystic images** | **Polycystic images** | **Single-stone images** | **Multiple-stones images** |
|---|---|---|---|---|
| Proposed level set method | 6.4 | 8.56 | 8.7 | 10.7 |
| ACM (Chapter 4) | 8.25 | 9.4 | -- | -- |
| GVF (Chapter 3) | 9.6 | 16.15 | 9.8 | 13.2 |

The comparison of the average execution time for complete segmentation of single-cystic, polycystic, single-stone, and multiple-stones images using the level set, ACM, and GVF based segmentation methods are shown in Table 5.1. It is observed that the execution time for the segmentation of polycystic and multiple-stones images is more than that of single-cystic/single-stone images in all the three algorithms. It is observed that the proposed level set method is capable to segment the kidney cysts and stones in lesser time than that of ACM and GVF based segmentation algorithms.

The proposed method of the level set for the segmentation of kidney stones is compared with the existing method specified by (W. Ardiatna et. al., 2018). Authors have used 50 clinical images, region-based segmentation with statistical descriptors is used. The algorithm needs a seed point by the user. An accuracy rate of 95% is achieved. The proposed level set method has an average accuracy rate of 96.1% and is completely automated without the need for user input. It is observed that the performance of the proposed method of a level set for the segmentation of renal calculi is better compared with the method in (W. Ardiatna et al., 2018). The proposed method is fully automatic. Hence, the proposed level set method performs the effective segmentation of renal stones in US images.

## 5.5 Statistical inference using Chi-square test

Chi-square test is performed on obtained and expert determined values of renal stone size as specified in Appendix III. Eight sample renal stone images are considered for the test. The chi-square distribution table value for a 5% level of significance is 15.507. The obtained value is lesser than the table value. i.e. 0.33 < 15.507. Hence, the null hypothesis $H_0$ is accepted. The acceptance indicates that the computed values are statistically acceptable.

## 5.6 Summary

In this chapter, an automated level set segmentation algorithm for the segmentation of cystic and renal stone US images is discussed. The segmentation of polycystic and multiple-stones images is carried out effectively by the level set method. The proposed level set segments the individual cysts and stones in polycystic and multiple-stones images respectively.

The experimental results of performance parameters show that the initial contour needed by the algorithm is effectively generated for both stone and cystic images automatically. The performance to measure the appropriate segmentation and execution time for computation, both are improved in the proposed level set method. Numbers of cysts/stones in the segmented image are determined along with their size. Chi-square test is performed on the kidney stone size, calculated after segmentation using the level set method. The test performed indicates that the computed values are statistically acceptable. Thus, the proposed level set based segmentation method performs fully automatic segmentation of cysts and stones successfully in US images of the kidney. The structural statistics found through the segmentation offer indispensable visual assistance for image-guided surgeries. Thus, the level set based segmentation algorithm is found to be more efficient in segmenting single-cystic, polycystic, single-stone, and multiple-stones images. Hence, the level set segmented output images are used for feature extraction and classification process discussed in the subsequent chapters.

# Chapter 6

# FEATURE EXTRACTION AND CLASSIFICATION OF KIDNEY ULTRASOUND IMAGES

## 6.1 Introduction

Among various diseases associated with the human kidney, the stone is a universally observed disorder. The recurrence rate of renal calculus is more. The other kidney disorder considered is polycystic kidney disease. It is one of the deadly diseases. It can further harm the organs like the liver, pancreas. In rare cases, the heart and brain can be affected in turn. Hence, the early diagnosis of these disorders is very important. The kidney is imaged to know its morphology.

It is necessary to extract the set of valuable features that explores the characteristics of the kidney accurately. So, the classification of renal cysts and stones in US images of the kidneys is one of the crucial research issues. It simplifies the process of diagnosing kidney diseases and their treatment.

In (K.B. Raja, M. Madheswaran, and K. Thyagarajah, 2000), an evaluation technique for principal curvature of the multi-scale differential is used. Classification of kidney image is carried out using obtained feature values. The analysis of features is a significant research issue. There is a major variation in intensities or colors of neighboring pixels. Particularly analysis of texture is a challenging problem because of the complex nature of texture. The image can be classified using texture analysis. The texture is used to separate the image into smaller regions. In (Shahabaz, D. K. Somwanshi, A. K. Yadav, and R. Roy, 2007), the authors explained that the small pixel value indicates smooth texture and the rough texture comprises larger values. The homogeneous graphical patterns are stated by texture features without a similar intensity or a single color.

---

[1] Akkasaligar Prema T., Biradar Sunanda, "Classification of Medical Ultrasound Images of Kidney", International Journal of Computer Applications, Special Issue on ICICT 2014, pp. 24-28.

[2] Akkasaligar Prema T., Biradar Sunanda, "Diagnosis of Renal Calculus Disease in Medical Ultrasound Images", IEEE International Conference on Computational Intelligence and Computing Research-2016, Agni College of Technology, Chennai, Tamilnadu, India, 15-17 Dec. 2016, pp. 948-952.

In (S. Poonguzhalil, B. Deepalakshmil, and G. Ravindran, 2007), the classification of ultrasonic liver images using texture features are discussed. The classification of normal and abnormal liver types is carried out using texture features. The principal component analysis (PCA) features are used followed by reduction. The K-means clustering is used for the identification of diseased and normal liver. Image analysis has a vital role in the medical field. In (S. Poonguzhali and G.Ravindran, 2006), the classification of liver tissue as normal or abnormal is carried out. Authors have used the wavelet, Laws' features, autocorrelation, and edge frequency features. The neural network classifier is used further for classification.

Three different segmentation algorithms namely, GVF, ACM, and level set for segmentation of kidney, cyst/stones in ultrasound images of the kidney have been discussed in Chapters 3, 4, and 5. The Level set based segmentation algorithm effectively segments the kidney cysts and stones in ultrasound images of the kidney. The level set is fully automated and demonstrates better performance in segmentation. It takes less computational time comparatively. Hence, the level set segmented images obtained from the algorithms Algorithm 5.2 and 5.3 discussed in Chapter 5, are used for feature extraction and classification process. Extraction of features from segmented renal US images of cysts and stones are discussed in the current Chapter. A different set of features and classifiers are used effectively. The experimentation details and results obtained are discussed. Various performance parameters used for determining the efficiency are elaborated. The combined approach for the selection of optimal feature sets for the classification of renal medical ultrasound images is explored.

## 6.2 Proposed method

A feature provides structural information about the image to be classified or an object of interest in an image. Different feature descriptors can be extracted from an image. For the classification of segmented renal US images into a normal kidney, single cystic, polycystic, single stone, and multiple-stones class, several sets of features are used.

The proposed methodology for feature extraction and classification is described in Fig. 6.1. The input ultrasound images of normal kidney, cystic, and calculi kidney are despeckled using a contourlet transform. The despeckled images are enhanced using histogram

equalization. Further, segmentation is applied using the level set method. The feature extraction is carried out to classify the images into the respective classes.

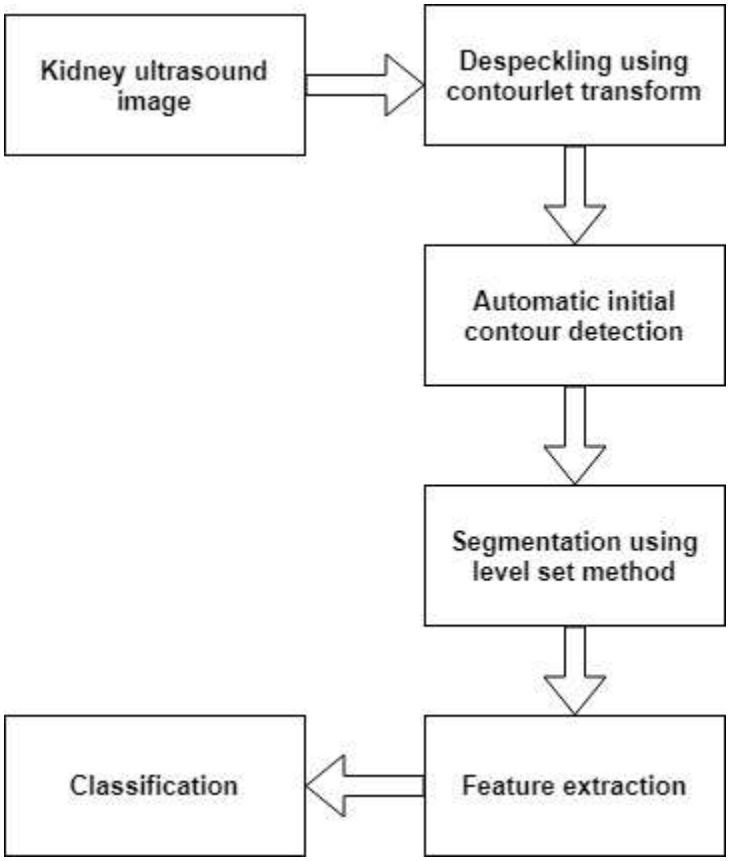


Fig. 6.1 Proposed method for feature extraction and classification of kidney US images

## 6.2.1 Feature extraction

The five feature sets namely Haralick features, shape features, wavelet features, Tamura features, and HOG features are applied individually for renal US images. The various features discussed in section 1.8 of Chapter 1 are used. All obtained feature values are normalized in the range of 0 to 1. Normalization aligns all the values within a specified range. It is essential as some of the feature values are of a larger range.

### *Haralick features*

Haralick features are extracted from the computed GLCM of input renal US image. The GLCM is computed based on the probability of gray-level distribution. The steps involved are elaborated in Algorithm 6.1.

**Algorithm 6.1: Haralick texture features extraction**

*Input:* Segmented renal ultrasound image.

*Output:* Sixteen normalized Haralick features.

*Begin*

*Step 1:* Read the input image.

*Step 2:* Compute the GLCM matrices in the directions of 0°, 45°, 90°, 135° using a a distance of 1 for the input image.

*Step 3:* Calculate the energy, homogeneity, contrast, and correlation for all the four matrices.

*Step 4:* Apply normalization to get the feature values in the range of 0 to 1, which gives a feature vector of 16 values.

*Step 5:* Store the normalized Haralick features vector for each input image.

*End.*

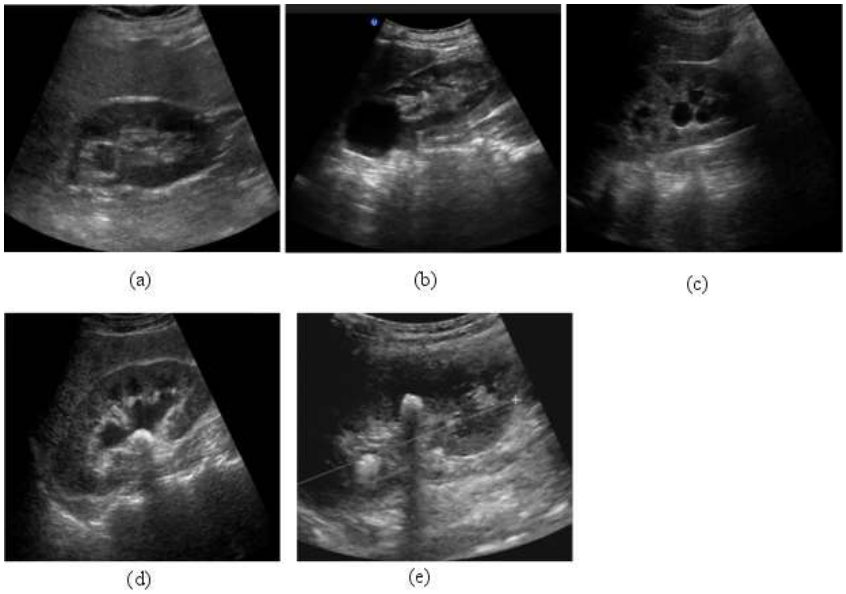


Fig. 6.2. Sample input images: (a) Normal US image of kidney (b) Single cystic US kidney image (c) Polycystic kidney image (d) Single stone kidney image (e) Multiple-stones kidney image

Table 6.1 shows the normalized values of Haralick features for sample inputs, one for each image class is given in Fig. 6.2.

Table 6.1 Normalized Haralick feature values for renal US image

| Features | Feature values | | | | |
|---|---|---|---|---|---|
| | Normal image | Single-cystic image | Polycystic image | Single-stone image | Multiple-stones image |
| Energy at $0^0$ | 0.118 | 0.346 | 0.382 | 0.366 | 0.248 |
| Homogeneity at $0^0$ | 0.129 | 0.155 | 0.174 | 0.159 | 0.142 |
| Contrast at $0^0$ | 0.296 | 0.161 | 0.063 | 0.141 | 0.224 |
| Correlation at $0^0$ | 0.305 | 0.319 | 0.385 | 0.328 | 0.306 |
| Energy at $45^0$ | 0.073 | 0.304 | 0.332 | 0.322 | 0.203 |
| Homogeneity at $45^0$ | 0.075 | 0.090 | 0.115 | 0.078 | 0.068 |
| Contrast at $45^0$ | 0.409 | 0.300 | 0.117 | 0.384 | 0.447 |
| Correlation at $45^0$ | 0.214 | 0.179 | 0.276 | 0.112 | 0.148 |
| Energy at $90^0$ | 0.094 | 0.334 | 0.362 | 0.344 | 0.235 |
| Homogeneity at $90^0$ | 0.100 | 0.143 | 0.147 | 0.122 | 0.122 |
| Contrast at $90^0$ | 0.366 | 0.106 | 0.078 | 0.232 | 0.229 |
| Correlation at $90^0$ | 0.234 | 0.307 | 0.319 | 0.217 | 0.260 |
| Energy at $135^0$ | 0.068 | 0.304 | 0.333 | 0.321 | 0.203 |
| Homogeneity at $135^0$ | 0.069 | 0.090 | 0.116 | 0.078 | 0.069 |
| Contrast at $135^0$ | 0.447 | 0.298 | 0.108 | 0.386 | 0.443 |
| Correlation at $135^0$ | 0.185 | 0.163 | 0.263 | 0.094 | 0.133 |

The Haralick features extracted are based on the location of pixels having similar gray level values. Cyst and stone are comprised of the pixels having completely different gray values. Thus, Haralick features obtained in Table 6.1 are effective in distinguishing kidney cyst from stone. However, distinguishing features cannot be obtained for a normal kidney.

## *Shape features*

The shape and size of cysts and stones are generally varying. The shape features contribute highly to the classification of renal cystic and stone images. The segmented image is converted into binary form to extract the features such as eccentricity, orientation, length of major, and minor axes. The binary image has a single region in case of single cystic and single stone images. It has multiple regions in the case of polycystic and multiple-stones images. The features are calculated on all the regions of the binary image. The various shape feature namely, area, perimeter, diameter, orientation, eccentricity, major, and minor axis length are used for renal kidney ultrasound image classification. Algorithm 6.2 describes the

steps involved in the shape feature extraction process. Table 6.2 shows the normalized values for shape features for different types of sample renal ultrasound images shown in Fig 6.2.

Table 6.2 Normalized shape feature values for renal US images

| Features | Feature values | | | | |
|---|---|---|---|---|---|
| | Normal image | Single-cystic image | Polycystic image | Single-stone image | Multiple-stones image |
| Area | 0.0023 | 0.0083 | 0.0724 | 0.0128 | 0.0076 |
| Convexarea | 0.0032 | 0.0265 | 0.0647 | 0.0102 | 0.0061 |
| Eccentricity | 0.3648 | 0.4492 | 0.2575 | 0.7148 | 0.1713 |
| Equi-diameter | 0.0064 | 0.0880 | 0.1876 | 0.1099 | 0.0845 |
| Major axis length | 0.0082 | 0.2091 | 0.1761 | 0.1095 | 0.0684 |
| Minor axis length | 0.0066 | 0.2189 | 0.1670 | 0.0857 | 0.0813 |
| Extent | 0.7134 | 0.1753 | 0.8944 | 0.8574 | 0.7763 |
| Filled area | 0.0021 | 0.0279 | 0.0676 | 0.0107 | 0.0064 |
| Orientation | 0.9996 | 0.0984 | 0.6022 | 0.9999 | 0.3805 |
| Perimeter | 0.0180 | 0.1408 | 0.1567 | 0.0870 | 0.0665 |
| Solidity | 0.8364 | 0.1717 | 0.8762 | 0.9017 | 0.8835 |

**Algorithm 6.2: Shape features extraction**

*Input:* Segmented renal ultrasound image.

*Output:* Eleven normalized shape features.

*Begin*

*Step 1:* Read the input image.

*Step 2:* Compute the shape features namely, area, perimeter, diameter, major axis, minor axis, eccentricity, and orientation using Eq. (1.8.5) to Eq. (1.8.8).

*Step 3:* Apply normalization to get the feature values in the range of 0 to 1, which gives a feature vector of 11 values.

*Step 4:* Store the normalized shape features vector for each input image.

*End.*

The segmented ROIs of normal kidney, cyst, and stone are of oval-shaped structures resembling the ellipse. Thus, the shape features namely area, perimeter, diameter, major axis length, minor axis length, eccentricity, and orientation shown in Table 6.2 are characterizing the unique properties of ROIs. Further, the shape features can effectively contribute to classification.

## *Wavelet features*

Wavelets are better in approximating the signals with sharp spikes or the discontinuous signals. Various wavelet families like as Daubechies, Haar, symlets, and biorthogonal filters and their combinations are experimented. A discrete wavelet transform (DWT) is tested for multiple decomposition levels. Table 6.3 shows the normalized values for some of the wavelet features for sample inputs shown in Fig. 6.2. (page no. 102)

Table 6.3 Normalized wavelet feature values for renal US images

| | Feature values | | | | |
|---|---|---|---|---|---|
| Wavelet family, level, sub-band, feature | Normal image | Single-cystic image | Polycystic image | Single-stone image | Multiple-stones image |
| Daubechies, Level 1, Horizontal, Mean | 0.580 | 0.858 | 0.552 | 0.593 | 0.222 |
| Daubechies,Level 1, Horizontal, Variance | 0.643 | 0.060 | 0.010 | 0.271 | 0.537 |
| Daubechies,Level 1, Horizontal, Range | 0.250 | 0.245 | 0.246 | 0.240 | 0.229 |
| Daubechies,Level 1, Horizontal, Energy | 0.957 | 0.035 | 0.077 | 0.008 | 0.005 |
| Daubechies,Level 1, Horizontal, Max. probability | 0.077 | 0.077 | 0.067 | 0.073 | 0.050 |
| Daubechies,Level 1, Horizontal, Homogeneity | 0.958 | 0.894 | 0.904 | 0.545 | 0.300 |
| Daubechies,Level 1, Horizontal, IDM | 0.690 | 0.025 | 0.382 | 0.855 | 0.807 |
| Daubechies,Level 1, Vertical, Mean | 0.905 | 0.520 | 0.730 | 0.706 | 0.705 |
| Daubechies,Level 1, Vertical, Variance | 0.400 | 0.085 | 0.085 | 0.280 | 0.323 |
| Daubechies,Level 1, Vertical, Range | 0.032 | 0.030 | 0.030 | 0.025 | 0.000 |
| Daubechies,Level 1, Vertical, Energy | 0.706 | 0.009 | 0.060 | 0.007 | 0.000 |
| Daubechies,Level 1, Vertical, Max. probability | 0.060 | 0.060 | 0.060 | 0.059 | 0.035 |
| Daubechies,Level 1, Vertical, Homogeneity | 0.975 | 0.277 | 0.995 | 0.952 | 0.929 |
| Daubechies,Level 1, Vertical, IDM | 0.009 | 0.000 | 0.730 | 0.892 | 0.873 |
| Daubechies,Level 1, Diagonal, Mean | 0.987 | 0.674 | 0.390 | 0.283 | 0.478 |
| Daubechies,Level 1, Diagonal, Variance | 0.300 | 0.006 | 0.039 | 0.069 | 0.039 |
| Daubechies,Level1, Diagonal, Range | 0.492 | 0.007 | 0.450 | 0.000 | 0.007 |
| Daubechies,Level 1, Diagonal, Energy | 0.508 | 0.000 | 0.025 | 0.000 | 0.000 |

It is determined that the decomposition up to level 3, for Daubechies and biorthogonal families are more appropriate empirically. Only detailed subbands are considered. In total 18 subbands are considered for feature extraction. These comprise of 3 at level 1, 3 at level2 and 3 at level3 for Daubechies and biorthogonal families. From these subbands, different features

such as mean, variance, range, energy, homogeneity, maximum probability, and IDM are extracted. Totally 126 features are extracted followed by normalization.

### *Tamura features*

Tamura features represent surface property and appearance of the objects. These features have the basis of visual perception. Coarseness, contrast, and direction are the features extracted for the classification of renal US images. Table 6.4 shows the normalized values for Tamura features for the sample inputs shown in Fig. 6.2 (page no. 103).

Table 6.4 Normalized Tamura feature values for renal US images

| Type of input renal US image | Normalized feature values | | |
|---|---|---|---|
| | Coarseness | Contrast | Direction |
| Normal | 0.664 | 0.978 | 0.964 |
| Single-cystic | 0.206 | 0.329 | 0.794 |
| Polycystic | 0.079 | 0.368 | 0.780 |
| Single-stone | 0.006 | 0.366 | 0.784 |
| Multiple-stones | 0.059 | 0.533 | 0.787 |

Tamura features shown in Table 6.4, contribute potentially in image representation. The effective role of Tamura features in classification US images of the kidney is justified with Kruskal Walli's test mentioned in Appendix III.

### *HOG features*

The HOG features are used for the classification of renal US images as discussed in section 1.8 of Chapter 1. The detailed process of HOG features extraction is shown in Algorithm 6.3.

**Algorithm 6.3: HOG features extraction**

*Input:* Segmented renal ultrasound image.

*Output:* A normalized vector of HOG features.

*Begin*

*Step 1:* Read the input image.

*Step 2:* Divide the image into cells of size 5X5.

*Step 3:* Find HOG directions for all the pixels within the cell.

*Step 4:* Discretize every cell in 9 bins based on the gradient directions of $0^0$ to $160^0$ at a variance of $20^0$.

*Step 5:* The blocks are constructed taking adjacent cells, based on histogram normalization.

*Step 6:* Save the histogram values as features for each block.

*End*.

The sets of Haralick, shape, wavelet, Tamura, and HOG features are used individually and in a combination of two, three, and all together as well.

### 6.2.2 Classification

The different features extracted from the US image of the kidney are classified using three different classifiers namely, k-NN, fuzzy k-NN, and SVM. The k-N N is an unsupervised machine learning algorithm. The input for the classifier is few closer training samples in the feature space. The output is a class membership to the nearest in the knowledge base. The classification is carried out based on a majority vote of its neighbors by using Euclidean distance. The sample to be tested is assigned to the class, most similar among its k nearest neighbors. k is tested with different values of 1, 2, 3, and 4. There is no explicit training phase for the k-NN algorithm. However, it is necessary to only store the feature vectors and class labels for the training samples. The testing is carried out by assigning the label which is most frequent among the k training samples and nearest to the query point. The k-NN is faster as there is no explicit training. But, the whole training set is needed during the testing stage.

SVM is a supervised classifier method. It works effectively in many classification problems wherever a large dataset is available. The algorithm works in two stages as the training and testing phase. Exhaustive training is needed to get better accuracy. Hence, it consumes more time than k-NN. The classification of kidney US image is also carried out using SVM.

Fuzzy set theory has found applications in many fields, such as pattern recognition, control systems, and medical applications (Sourabh Dash, Raghunathan Rengaswamy, and Venkat Subramanian, 2003; Nedeljkovic I., 2004). Fuzzy logic was initiated in 1965 by L. A. Zadeh (Zadeh L. A., 1965; Zadeh L. A., 1973; Zadeh L. A., 1984). It is also used to develop different techniques in image processing applications including ultrasound images (Kerre E.

E. and Nachtegael M., 2000; Khademi A., et al., 2009). The existence of inherent "fuzziness" in the nature of the image itself in terms of uncertainties associated with the definition of edges, boundaries, and contrast makes the fuzzy theory a remarkable tool for handling the ultrasound imaging applications (Hiremath P. S. and Tegnoor J. R., 2011). Hence, a fuzzy-based k-NN classifier algorithm is implemented to classify the US images of the kidney.

## 6.3 Experimental results and discussion

Feature extraction and classification are carried out on all 185 US images of the kidney, cysts, and stones. The dataset specified in section 1.5 contains the clinical (S1) and web (S2) datasets, comprising of 37 normal kidney images, 39 single-cystic, 35 polycystic, 38 single-stone, and 36 multiple-stones images altogether. The algorithms are implemented on Intel core i5 processor with 4GB RAM @ 2.5GHz, using MATLAB 7.11. The denoising of images is carried out using contourlet transform as discussed in section 3.3.1 of Chapter 3. The denoised images are segmented using the level set method specified in Chapter 5. The segmented images are passed through feature extraction and classification.

Different feature sets namely Haralick, shape, wavelet, Tamura, and HOG features are extracted as specified in section 6.2.1 using the Algorithms 6.1, 6.2, and 6.3. The different feature sets and their combinations are tested using three different classifiers namely k-NN, fuzzy k-NN, and SVM. These classifiers are used to classify the renal ultrasound images into normal kidney, single cystic, polycystic, single stone, and multiple-stones classes. For k-NN and fuzzy k-NN, k value of 3 is empirically determined. Euclidean distance is used as a distance metric. For SVM classifier, Gaussian radial basis kernel function with a scaling factor of 1 is determined as more suitable in the classification of kidney ultrasound images. The 5-fold validation is performed for all the classifiers. In all the three classifiers, the training and testing image sets are randomly selected using a 5-fold method. The average classification accuracy for individual feature sets using the three classifiers is shown in Fig 6.3.

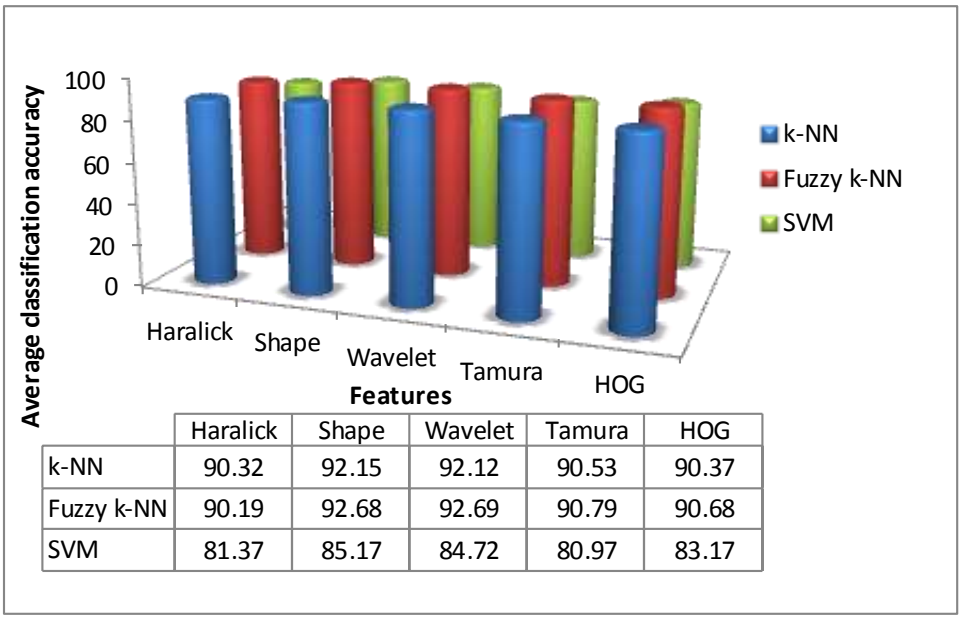


| | Haralick | Shape | Wavelet | Tamura | HOG |
|---|---|---|---|---|---|
| k-NN | 90.32 | 92.15 | 92.12 | 90.53 | 90.37 |
| Fuzzy k-NN | 90.19 | 92.68 | 92.69 | 90.79 | 90.68 |
| SVM | 81.37 | 85.17 | 84.72 | 80.97 | 83.17 |

Fig. 6.3 Average accuracy for k-NN, fuzzy k-NN, and SVM using individual feature sets

From Fig 6.3, it is observed that shape and wavelet feature sets are better in classifying the medical US images of the kidney. The performance of the fuzzy k-NN is better than the k-NN and SVM classifier.

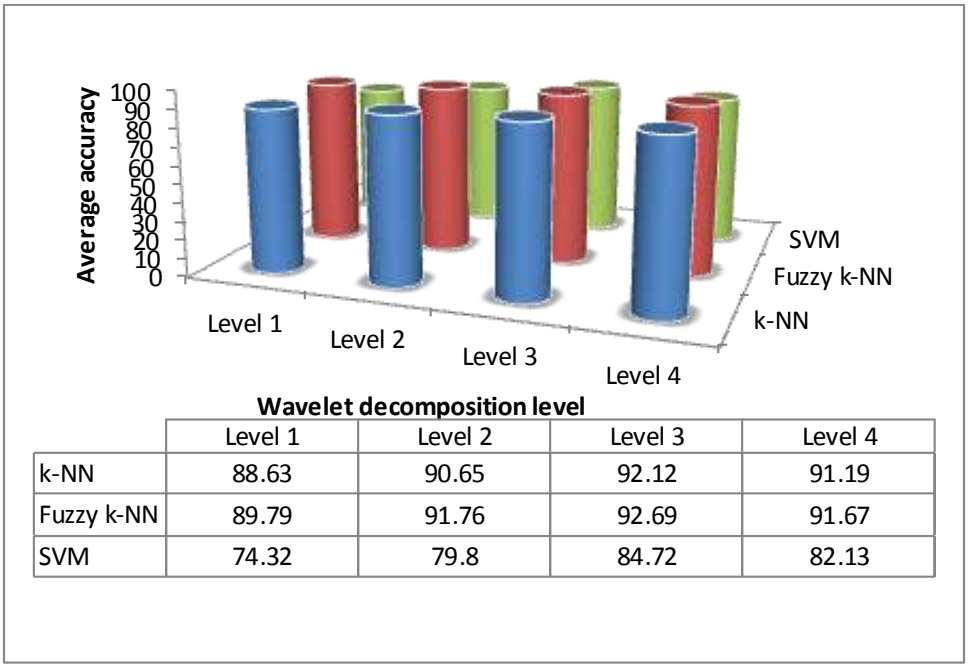


| | Level 1 | Level 2 | Level 3 | Level 4 |
|---|---|---|---|---|
| k-NN | 88.63 | 90.65 | 92.12 | 91.19 |
| Fuzzy k-NN | 89.79 | 91.76 | 92.69 | 91.67 |
| SVM | 74.32 | 79.8 | 84.72 | 82.13 |

Fig. 6.4 Average accuracy for wavelet feature model at different decomposition levels

Experimentation is carried out on feature sets obtained at different levels of wavelet decomposition such as level 1, level 2, level 3, and level 4 using the three classifiers. Fig 6.4 shows the plot of average accuracy obtained at different levels. From Fig 6.4, it is observed that the accuracy increases up to third level and decreases at fourth level. Hence, empirically third level decomposition is considered to be optimal. For better performance, the combined feature set of detailed subbands at all three levels of decomposition are considered for classification. The fuzzy k-NN classifier shows better performance among the three classifiers.

The models with a combined feature set of two and three feature sets are considered for classification of renal US images are shown in Fig 6.5 and Fig 6.6 respectively. The feature sets are labeled as H, S, W, T, and G indicating Haralick, shape, wavelet, Tamura, and HOG sets respectively. Fig 6.5 shows the graph of average classification accuracy obtained for the ten possible combinations of two feature sets, namely, Haralick-shape(H-S), Haralick-wavelet (H-W), Haralick-Tamura(H-T), Haralick-HOG(H-G), HOG-wavelet(G-W), Tamura-wavelet (T-W), Tamura-HOG(T-G), shape-Tamura (S-T), shape-HOG(S-G,) and shape-wavelet(S-W).

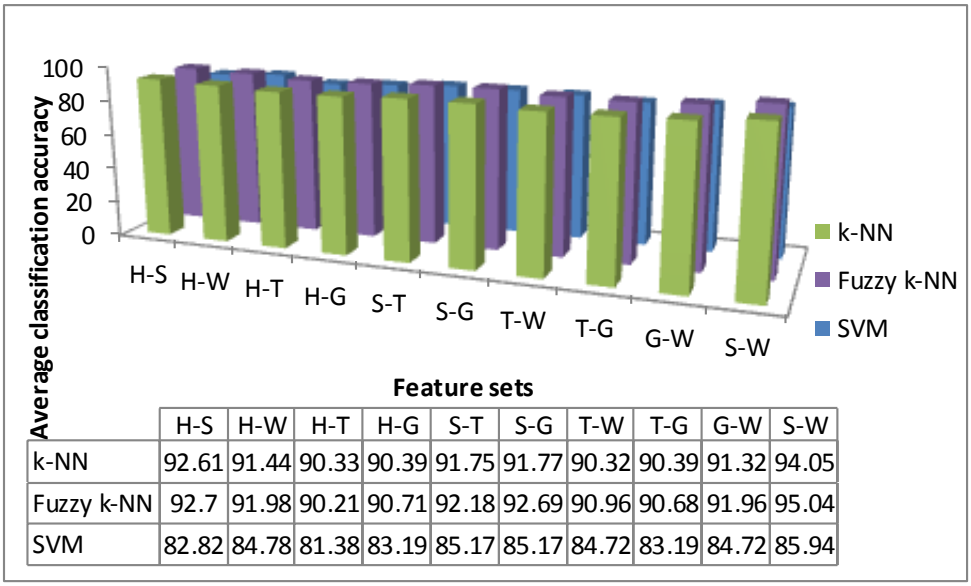


| | H-S | H-W | H-T | H-G | S-T | S-G | T-W | T-G | G-W | S-W |
|---|---|---|---|---|---|---|---|---|---|---|
| k-NN | 92.61 | 91.44 | 90.33 | 90.39 | 91.75 | 91.77 | 90.32 | 90.39 | 91.32 | 94.05 |
| Fuzzy k-NN | 92.7 | 91.98 | 90.21 | 90.71 | 92.18 | 92.69 | 90.96 | 90.68 | 91.96 | 95.04 |
| SVM | 82.82 | 84.78 | 81.38 | 83.19 | 85.17 | 85.17 | 84.72 | 83.19 | 84.72 | 85.94 |

Fig. 6.5 Average classification accuracy for a combination of two feature sets

In the plot of Fig 6.5 shape-wavelet(S-W) model is found to be the optimal combination as shown in the last column. The accuracy rate of 85.94% for SVM, 94.05% for k-NN, and 95.04% for fuzzy k-NN are obtained. Hence, fuzzy k-NN is found to be more suitable for the classification of kidney ultrasound images.

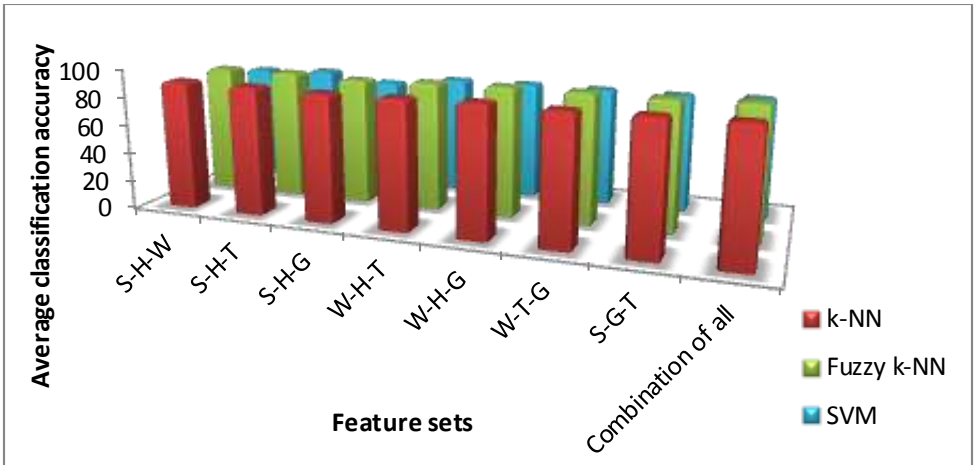


| | S-H-W | S-H-T | S-H-G | W-H-T | W-H-G | W-T-G | S-G-T | Combination of all |
|---|---|---|---|---|---|---|---|---|
| k-NN | 91.17 | 90.75 | 89.75 | 90.32 | 91.32 | 90.3 | 90.75 | 91.35 |
| Fuzzy k-NN | 91.68 | 91.68 | 89.68 | 91.19 | 91.96 | 91.6 | 91.08 | 92.17 |
| SVM | 82.17 | 84.17 | 78.17 | 83.72 | 84.02 | 83.67 | 83.17 | 84.35 |

Fig. 6.6 Average classification accuracy for a combination of three feature sets and combination of all features

Fig. 6.6 shows the plot of average classification accuracy for a combination of three feature sets and a combination of all features using three different classifiers namely k-NN, SVM, and fuzzy k-NN. From Fig 6.6, it is observed that the combined feature set of two feature sets (shown in Fig. 6.5) are generating better results as compared to the combined feature set of three features.

Experimentation on different values of k for k-NN and fuzzy k-NN for a combined feature sets of shape and wavelet features is carried out. The obtained accuracy values are shown in Table 6.5.

Table 6.5 Accuracy of k-NN and fuzzy k-NN for a combined feature sets of shape and wavelet(S-W) features

| | k=1 | k=2 | k=3 | k=4 |
|---|---|---|---|---|
| k-NN | 89.8 | 92.3 | 94.05 | 93.0 |
| Fuzzy k-NN | 90.6 | 92.9 | 95.04 | 93.5 |

From Table 6.5, it is observed that the performance of k-NN and fuzzy k-NN classifiers is optimal at k value of 3.

The confusion matrix for the combined feature set of shape and wavelet using the three classifiers namely, k-NN, SVM, and fuzzy k-NN is shown in Table 6.6, Table 6.7, and Table 6.8 respectively. It is possible to compute true positive, true negative, false positive, and false negative by using the confusion matrix as described in Fig. 1.16 of Chapter 1. In turn, these parameters can be used to compute accuracy as the ratio of the number of correctly classified images to the total number of images of a respective class.

Table 6.6 Confusion matrix for the combined feature set of shape and wavelet using k-NN

| | Normal kidney | Single-Cystic | polycystic | Single-stone | Multiple-stones |
|---|---|---|---|---|---|
| Normal kidney | 35 | 01 | -- | 01 | -- |
| Single-Cystic | 01 | 38 | -- | -- | -- |
| polycystic | 01 | 01 | 33 | -- | -- |
| Single-stone | 02 | -- | -- | 35 | 01 |
| Multiple-stones | 02 | -- | -- | 01 | 33 |

Table 6.7 Confusion matrix for the combined feature set of shape and wavelet using SVM

| | Normal kidney | Single-Cystic | polycystic | Single-stone | Multiple-stones |
|---|---|---|---|---|---|
| Normal kidney | 30 | 04 | 02 | 01 | -- |
| Single-Cystic | 02 | 37 | -- | -- | -- |
| polycystic | 01 | 01 | 32 | 01 | -- |
| Single-stone | 06 | 01 | 01 | 30 | -- |
| Multiple-stones | 03 | 02 | -- | 01 | 30 |

Table 6.8 shows the confusion matrix for the combined feature set of shape and wavelet features using the fuzzy k-NN classifier. Five-fold cross validation is carried out for the

classifiers and average values of all the 5 iterations in the validation are taken into consideration.

Table 6.8 Confusion matrix for the combined feature set of shape and wavelet using fuzzy k-NN

| | Normal kidney | Single-Cystic | polycystic | Single-stone | Multiple-stones |
|---|---|---|---|---|---|
| Normal kidney | 35 | -- | 01 | 01 | -- |
| Single-Cystic | 01 | 38 | -- | -- | -- |
| polycystic | 01 | -- | 33 | 01 | -- |
| Single-stone | 01 | -- | -- | 36 | 01 |
| Multiple-stones | 01 | 01 | -- | -- | 34 |

It is observed from Tables 6.6, 6.7, and 6.8 that the fuzzy k-NN classifier performs better compared to k-NN and SVM for the proposed method. The proposed fuzzy k-NN classifier with wavelet and shape features classifies the input images into normal kidney, cystic, and kidney stone images with an overall accuracy of 95.04% as shown in Fig 6.5.

The performance metrics namely precision, recall, F1score are calculated using the confusion matrices obtained for all the three classifiers. Precision computes the percentage of the relevant samples. Recall computes the percentage of the samples that are actually found among all the relevant classes. The F1 score is obtained by finding the harmonic mean of precision and recall. It reaches its best value at 1 and worst at 0 (Vijay Kotu and Bala Deshpande, 2019). Precision, recall, and F1 score are computed using the Eqs. 6.2, 6.3, and 6.4 respectively.

$$\text{Precision} = \frac{\text{true}_\text{p}}{\text{true}_\text{p}+\text{false}_\text{p}} \tag{6.2}$$

$$\text{Recall} = \frac{\text{true}_\text{p}}{\text{true}_\text{p}+\text{false}_\text{n}} \tag{6.3}$$

$$\text{F1 Score} = 2 * \frac{\text{Precision}*\text{Recall}}{\text{Precision}+\text{Recall}} \tag{6.4}$$

The values of the parameters obtained are shown in Table 6.9.

Table 6.9 Performance parameters of the classifiers

| Image class | k-NN | | | SVM | | | Fuzzy k-NN | | |
|---|---|---|---|---|---|---|---|---|---|
| | Precision | Recall | F1score | Precision | Recall | F1score | Precision | Recall | F1score |
| Normal kidney | 0.854 | 0.946 | 0.898 | 0.714 | 0.811 | 0.759 | 0.897 | 0.946 | 0.921 |
| Single-cystic | 0.95 | 0.974 | 0.962 | 0.822 | 0.948 | 0.881 | 0.974 | 0.974 | 0.974 |
| poly-cystic | 0.943 | 1.0 | 0.971 | 0.914 | 0.914 | 0.914 | 0.971 | 0.943 | 0.957 |
| Single-stone | 0.921 | 0.946 | 0.933 | 0.909 | 0.811 | 0.857 | 0.947 | 0.947 | 0.947 |
| Multiple-stone | 0.917 | 0.971 | 0.943 | 1.0 | 0.833 | 0.909 | 0.971 | 0.944 | 0.957 |

From Table 6.9, it is observed that the fuzzy k-NN achieves precision, recall, and F1 score nearer to 1, exhibiting the better performance of the classifier. From the experimental results, it is observed that the supervised classifiers such as SVM are not suitable for the smaller training sets. Another added advantage of non-parametric classifiers like k-NN and fuzzy k-NN is a substantial reduction in training time. Hence, the proposed method using combined sets of shape and wavelet features using a fuzzy k-NN classifier is found to be better than the existing methods discussed in the literature.

The details of comparison of the proposed method with the methods in the literature are shown in Table 6.10. The proposed method can be compared with the method in (Jyoti Verma, et al., 2017), kidney stones in ultrasound images are identified using k-NN and SVM classifiers. Morphological segmentation is applied before classification. In (K. Kumar, 2012), laboratory blood test parameters of 1000 patients are directly used for the identification of kidney stones using artificial neural networks, and an accuracy of 92% is achieved. In (Goel R. and Jain A., 2020), kidney abnormality and stones are detected with an accuracy rate of 90%.

Table 6.10 Comparison of results of the proposed method

| | Method in ( Jyoti Verma, et al., 2017) | Method in (Goel R. and Jain A, 2020) | Proposed method |
|---|---|---|---|
| Dataset | US images of the kidney (Clinical dataset) | US images of kidney | US images of kidney |
| Algorithms used | Morphological segmentation<br>SVM and k-NN | Region growing segmentation<br>GLCM features, SVM | Level set segmentation<br>Shape &wavelet features,<br>Fuzzy k-NN |
| Accuracy rate | 89% for k-NN<br>84% for SVM | 90% | 95.04% |

From Table 6.10, it is observed that the proposed fuzzy k-NN classifier using a combined feature set of shape and wavelet features performs better comparatively.

### *Mobile interface*

To provide an easy to use interface to the users on handheld devices like smartphone, an application is developed. The application is compatible with any Android device. The application offers various facilities to the radiologists, medical professionals, and patients, such as real-time viewing of segmented and classified results on US images of kidney. Computerized analysis on the segmented image such as size and location of the cysts/stone is also provided. The application enables collaboration between medical experts and patients effectively. It provides easy access for accurate diagnosis in real-time and thus helps in taking the right decision. The details of the user interface are discussed in Appendix II.

## 6.4 Summary

In this Chapter, the extraction of features and classification of segmented kidney US images is discussed. Segmented ultrasound images of the kidney using the level set method are used as input by the feature extraction module. Individual feature sets like Haralick, shape, wavelets, Tamura, and histogram oriented gradient features are extracted. Extracted features

are used in different combinations of two and three feature sets as well. Three different classifiers namely k-NN, fuzzy k-NN, and SVM are used to classify the input kidney US images into five classes namely, normal kidney, single cystic, polycystic, single stone, and multiple-stones. The performance of the classifiers is measured by the parameters accuracy, precision, recall, and F1 score. The accuracy rate of 95.04 % is achieved using fuzzy k-NN with combined features set of shape and wavelet features. The proposed algorithm can be used for clinical analysis of kidney medical ultrasound images by the medical experts.

# Chapter 7

# CONCLUSION AND FUTURE SCOPE

Automatic diagnosis of diseases through medical images is an important application in the field of health care. This research work attempts to provide a robust method on analysis of renal calculus and polycystic kidney disease in medical ultrasound images of the kidney using image processing techniques. The contributions made by this research work are highlighted with conclusions and scope for future works in this chapter.

## 7.1 Conclusion

The recent trends in medical image processing and the application of the available techniques have motivated in defining the problem of analysis on renal calculus and polycystic kidney diseases. Among the various available imaging modalities for diagnosis, ultrasound images are taken into account. Among the different kidney diseases, renal stones, and polycystic kidney disease are considered. Renal stone is the most common issue world-wide and polycystic kidney disease is a genetic disorder, if not treated at an earlier stage, it can affect the other major organs like heart and brain, leading to the death of a person. The overall process of implementation involves major steps of automatic initial contour generation, automatic segmentation, feature extraction, and detection of stones and cysts in US images of the kidney.

Different spatial domain and transform domain filters are tested for speckle noise removal of renal ultrasound medical images. The filters like Gaussian, Weiner, median, wavelet transform, and contourlet transform are used for denoising of kidney ultrasound images. The contourlet transform is found to be the better method for denoising of renal ultrasound images. It is justified using various performance parameters namely, MSE, PSNR, and CC.

Automatic initial contour generation for segmentation has many advantages. It reduces the burden and saves the time of medical experts to a greater extent avoiding manual annotation for every image. The segmentation of the denoised kidney US images is carried out using GVF based segmentation method. The proposed GVF based segmentation algorithm is a

semi-automatic method. It needs explicit specification of initial contour by the user, making the segmentation semi-automatic. It is observed that GVF segmentation performs well in segmenting the normal kidney, single-cystic, and single–stone renal ultrasound images.

An automated ACM segmentation algorithm is implemented for the segmentation of cystic renal US images. The algorithm is automated completely, avoiding the specification of initial parameters by the user. The automatic initial contour needed by the algorithm is effectively generated by using morphological operations. The efficiency of the proposed algorithm is measured by comparing segmented images with manually marked images by the medical experts. It is found that the proposed ACM method is good at segmenting single-cystic ultrasound images of the kidney. But it segments a single region enclosing all the cysts. Hence, it is not effective in polycystic kidney US images.

An automated level set segmentation algorithm can be effectively used for the segmentation of cystic and renal stone US images. The initial contour is generated automatically and effectively for segmenting the stones and cysts in US images of the kidney. The drawbacks of ACM based segmentation are improved to segment the individual cysts and stones in polycystic and multiple renal stone images respectively. Different performance parameters namely DC, JC, sensitivity, specificity, accuracy, and execution time are used for measuring the performance of the proposed segmentation algorithm. The performance to measure the appropriate segmentation method and execution time for computation, both are improved in the proposed level set method. The segmented results are analyzed to determine the number of cysts and stones with their size. The chi-square method, a statistical method is used to find the relevance between the values of stone sizes determined experimentally and by expert opinion. The structural statistics found through the segmentation offer indispensable visual assistance for image-guided surgeries.

Segmented ultrasound images using a level set algorithm are read as input for feature selection. Individual feature sets like Haralick, shape, wavelets, Tamura, and histogram oriented gradient features are extracted. The feature sets are used individually as well as in the combination of two and three feature sets by the decision support system. A combined approach having shape-based and wavelet features set is the best feature model for classification. Extracted features are classified by three different classifiers namely k-NN, fuzzy k-NN, and SVM. The performance of the proposed method is measured using

sensitivity, specificity, accuracy, precision, recall, and F1 score. The accuracy rate of 95.04 % is achieved using fuzzy k-NN with combined features sets of wavelet and shape features to classify the kidney US images into normal kidney, single-cystic, polycystic, single-stone, and multiple-stones classes.

The segmentation of kidney cysts and stones using a level set segmentation method followed by classification using a fuzzy k-NN classifier with combined features set of shape and wavelet yields better results. The proposed algorithm can be effectively used for clinical analysis of kidney medical ultrasound images such as number of cysts and stones along with size, by the medical experts for precise treatment. The proposed automated system can be used for mass screening to obtain the results in lesser time.

Overall, the significant contributions of the present research study are the following:

i. Semiautomatic segmentation of kidney cysts, and stones in US image using gradient vector force algorithm. Performance evaluation of the GVF based segmentation algorithm using DC, JC, sensitivity, specificity, accuracy, and amount of execution time (Chapter 3).

ii. Automatic initial contour detection using morphological operations and segmentation of kidney cysts in the US image using an active contour model. Performance valuation of the segmented algorithm and calculation of cyst size (Chapter 4).

iii. Fully automatic segmentation of kidney cysts, and stones in US image using the level set method is found to be superior to GVF and ACM based segmentation methods. Improved performance in terms of DC, JC, sensitivity, specificity, accuracy, and amount of execution time. Identification of the number of cysts/stones in the segmented US images of the kidney along with their sizes. Verification of statistical acceptance of determined stone size using the chi-square test (Chapter 5).

iv. Feature extraction and classification of the level set segmented kidney US images into the five classes using different classifiers. Verification of statistical importance of extracted features using the Kruskal Wallis test. The five classes are normal kidney, single-cystic, polycystic, single-stone, and multiple-stones. Experimentation on various classifiers such as k-NN, SVM, and fuzzy k-NN is carried out (Chapter 6).

It is found that the level set method proposed in Chapter 5 has yielded better segmentation results. Further the combined feature set of shape and wavelet-based features with fuzzy k-NN classifier has yielded better classification results for kidney diseases. An easy to use mobile interface is developed for the medical experts. The interface offers various functionalities such as real-time viewing of segmented and classified results on US images of kidney. It helps to collaborate with other medical experts and patients in an effective manner. It provides easy access for accurate diagnosis in real-time and thus helps in taking the right decision.

## 7.2 Future scope

The present study has further scope for enhancement. The development of a computer-aided automated diagnostic system for analysis of polycystic kidney disease and renal stones for the Indian race using deep learning techniques can be taken up as a major research objective. As there is no availability of benchmark datasets for ultrasound images of the kidney, PCKD, and renal stones, the benchmark dataset in consultation with a medical expert can be created. The diagnosis of other kidney disorders like chronic kidney disease, lupus nephritis, and kidney cancer can be taken up for research. Attention is required in the diagnosis of diseases in 3D ultrasound images. The work can be extended to the diseases associated with different organs. The images from different imaging modalities like CT, MRI can be taken up for the purpose of automatic diagnosis.

The development of ultrasound machines embedded with these advanced algorithms leading to immediate, real-time diagnosis and analysis of the various diseases requires due attention. The developed computerized algorithms can be directly connected with the real-time input of the ultrasound machine. This can be achieved through Aurdino and Raspberry pi models. Such methods can take further advantages with the use of IoT applications as well.

To conclude, the research investigation on analysis of renal calculus and polycystic kidney disease in medical ultrasound images recognition presented in this thesis opens further research avenues in the medical image analysis.

# Appendix I

# KIDNEY ULTRASOUND IMAGE DATASET

Ultrasound images of kidney are used for the design and development of an automatic diagnosis system for kidney diseases. Medical renal ultrasound B-mode images having different sizes and orientations are used. The input US image set is comprised of two sets S1 and S2. The images in S1 (Clinical dataset) are collected from BLDEDU's Shri. B.M. Patil Medical College and Research Centre, Vijayapura. The images in S2 (Website dataset) are collected from medical websites, namely, https://openi.nlm.nih.gov, http://www.sonoworld.com, and https://www.ultrasoundimages.com. Totally 185 images are used for the experimentation; the S1 set contains 105 images and S2 contains 80 images as shown in Table AI.1. The dataset includes normal, single cystic, polycystic, renal calculi medical ultrasound images.

Table AI.1 Image dataset

| Kidney Image type | Number of images | | |
|---|---|---|---|
| | Dataset S1 | Dataset S2 | Total |
| **Normal kidney** | 12 | 25 | 37 |
| **Single cystic** | 19 | 20 | 39 |
| **Polycystic** | 24 | 11 | 35 |
| **Single stone** | 24 | 14 | 38 |
| **Multiple-stones** | 26 | 10 | 36 |
| **Total number of images** | 105 | 80 | 185 |

## *Ultrasound Images of Normal Kidney*

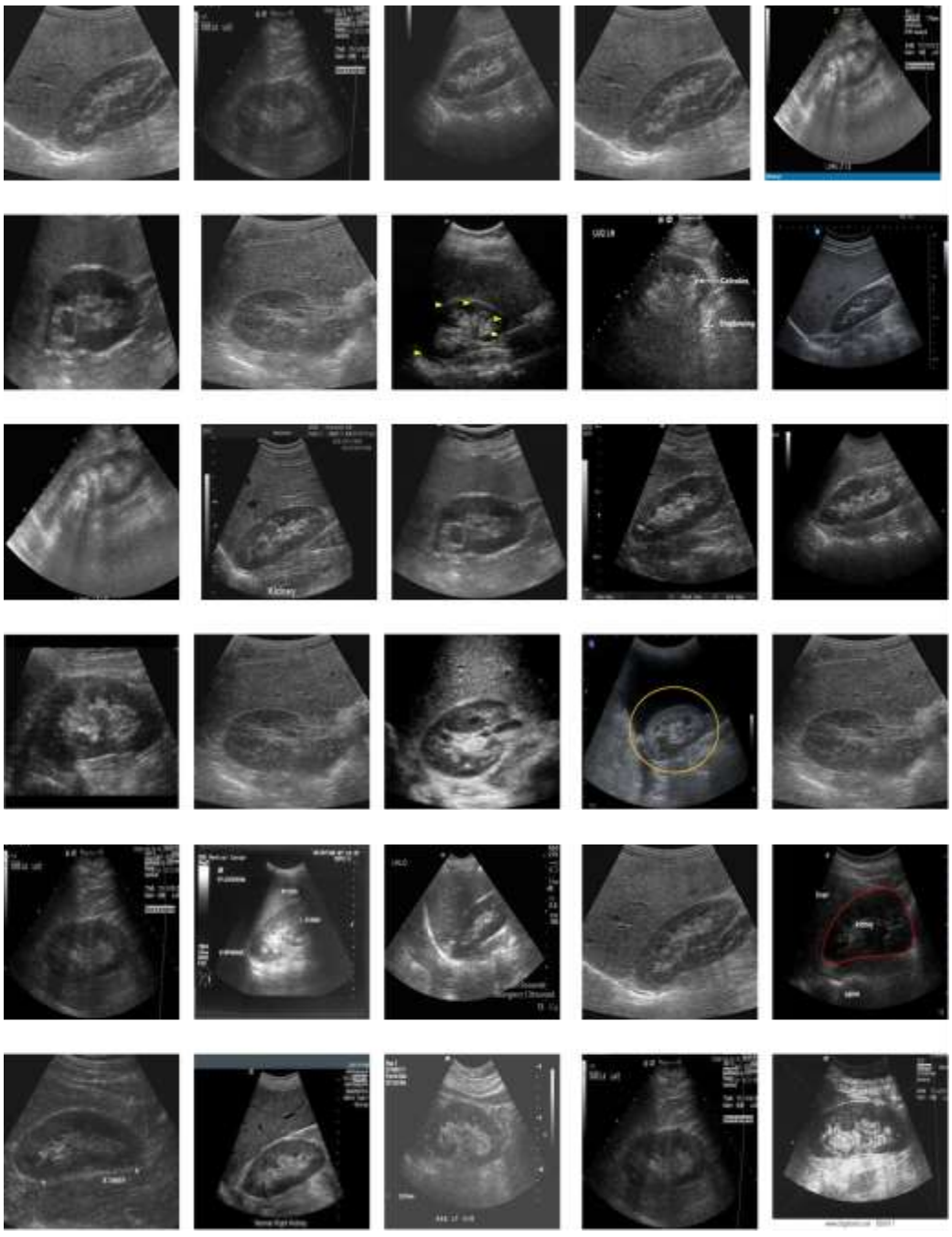

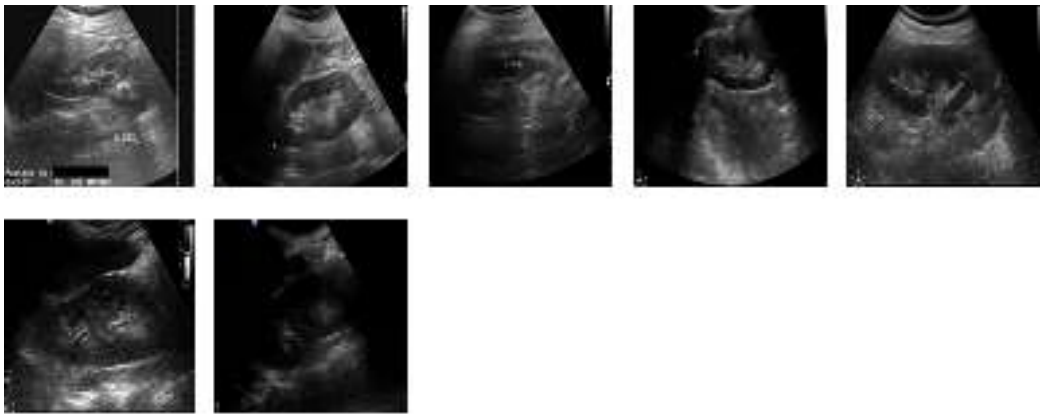

*Ultrasound Images of Single-Cystic Kidney*

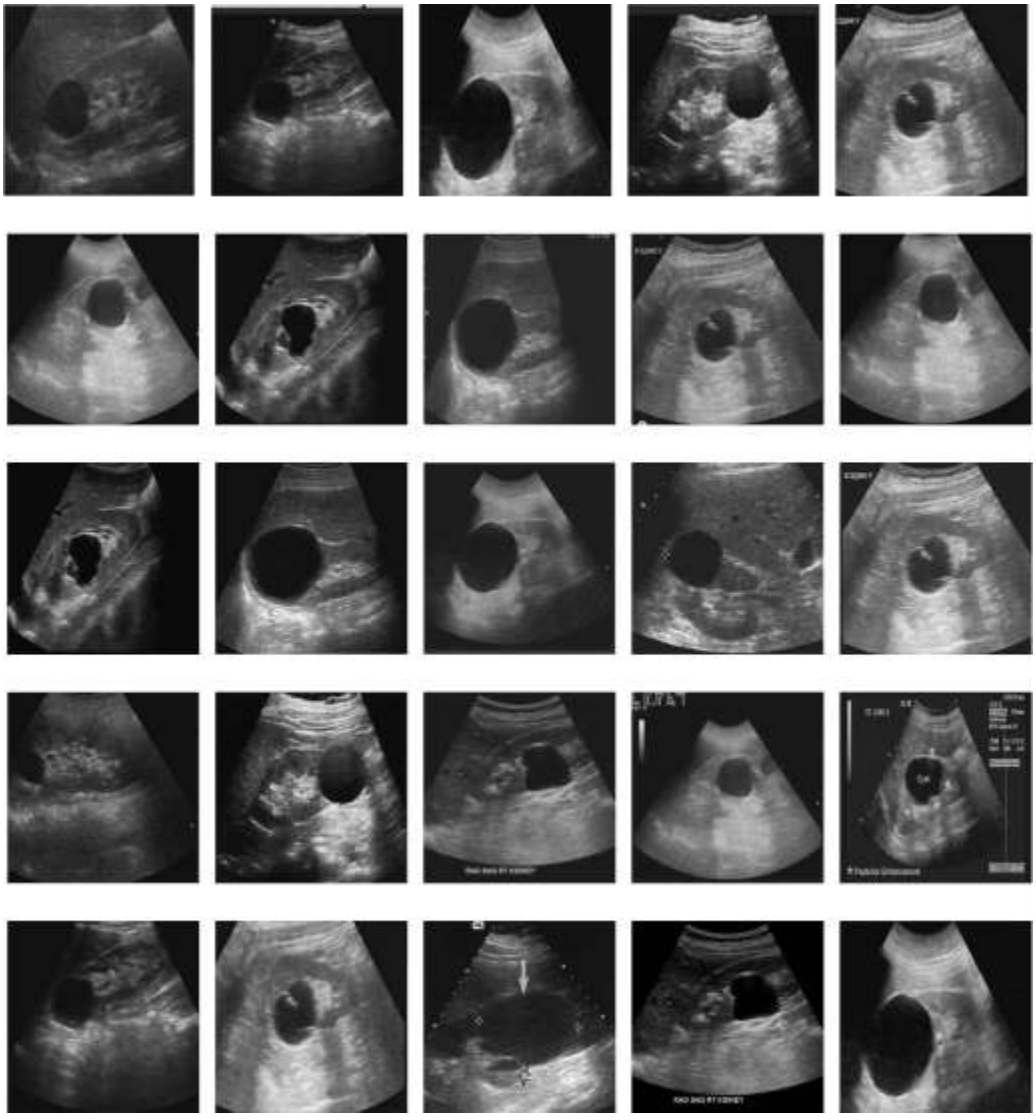

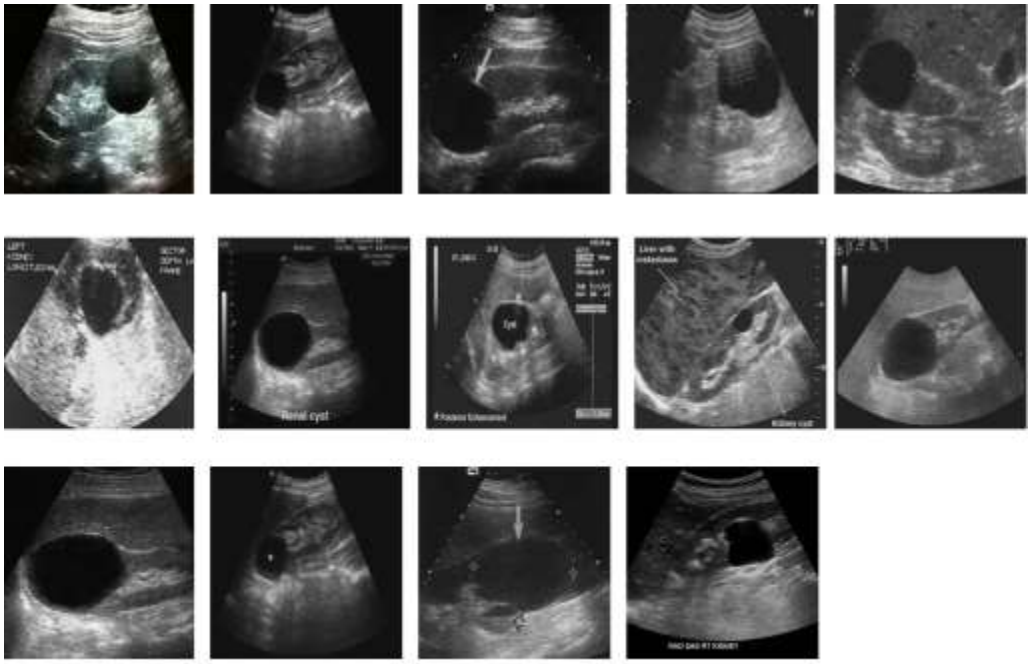


*Ultrasound Images of Polycystic Kidney*

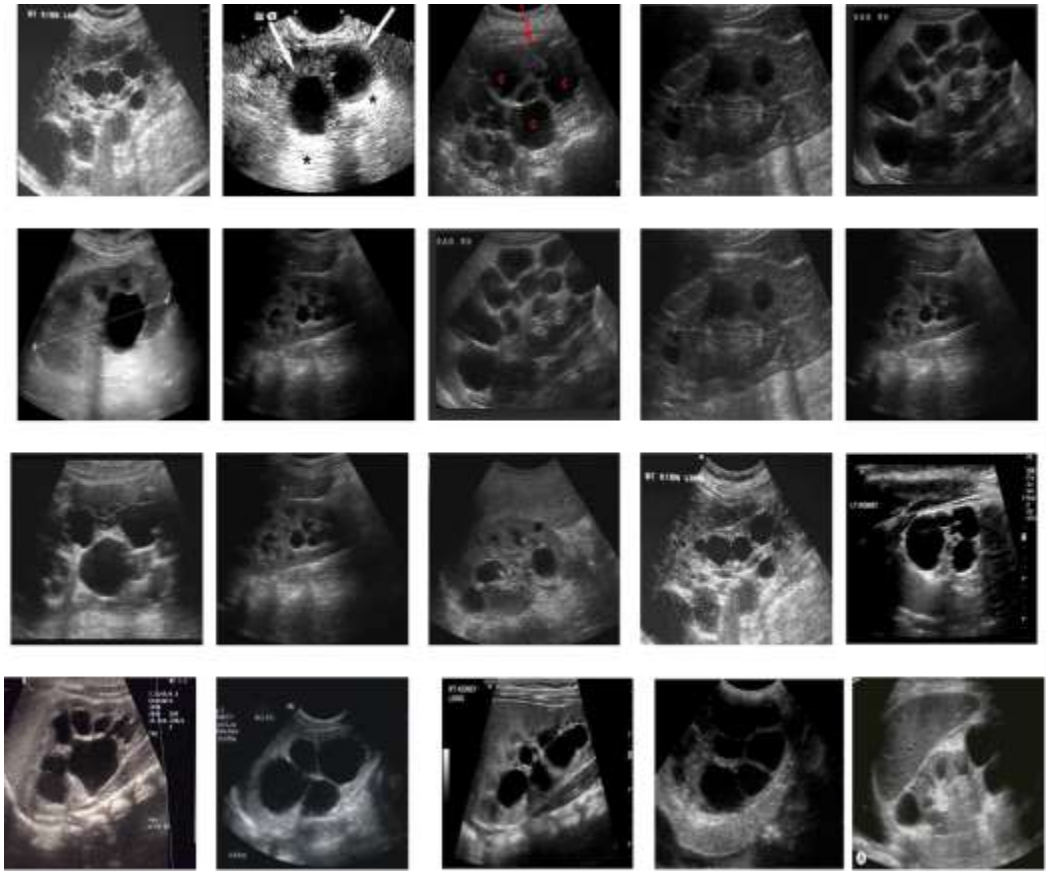

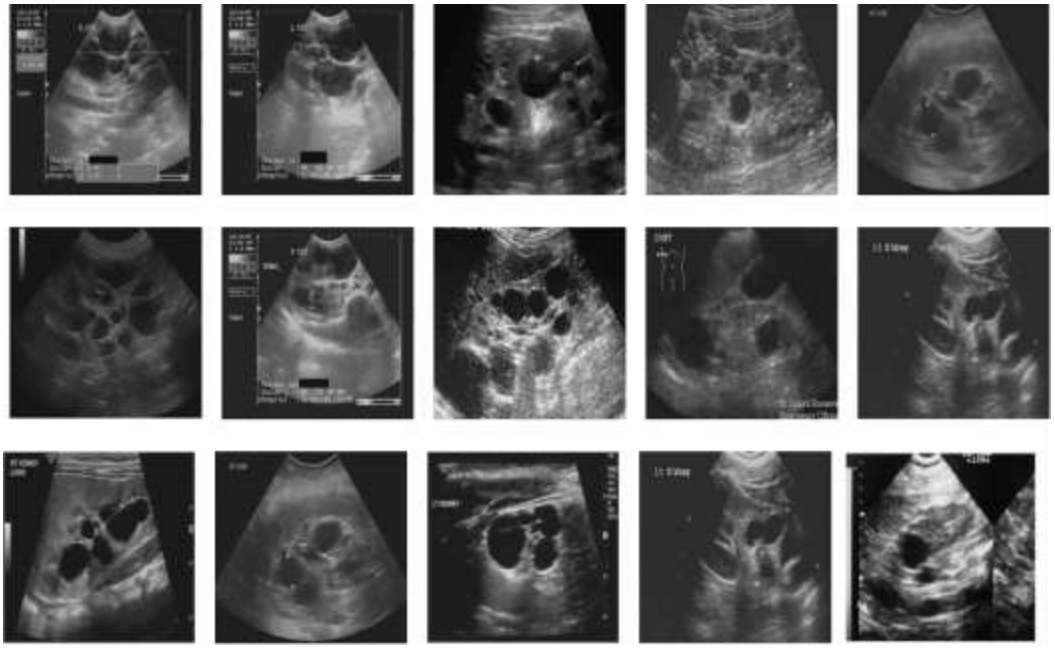

*Ultrasound Images of Single-stone Kidney*

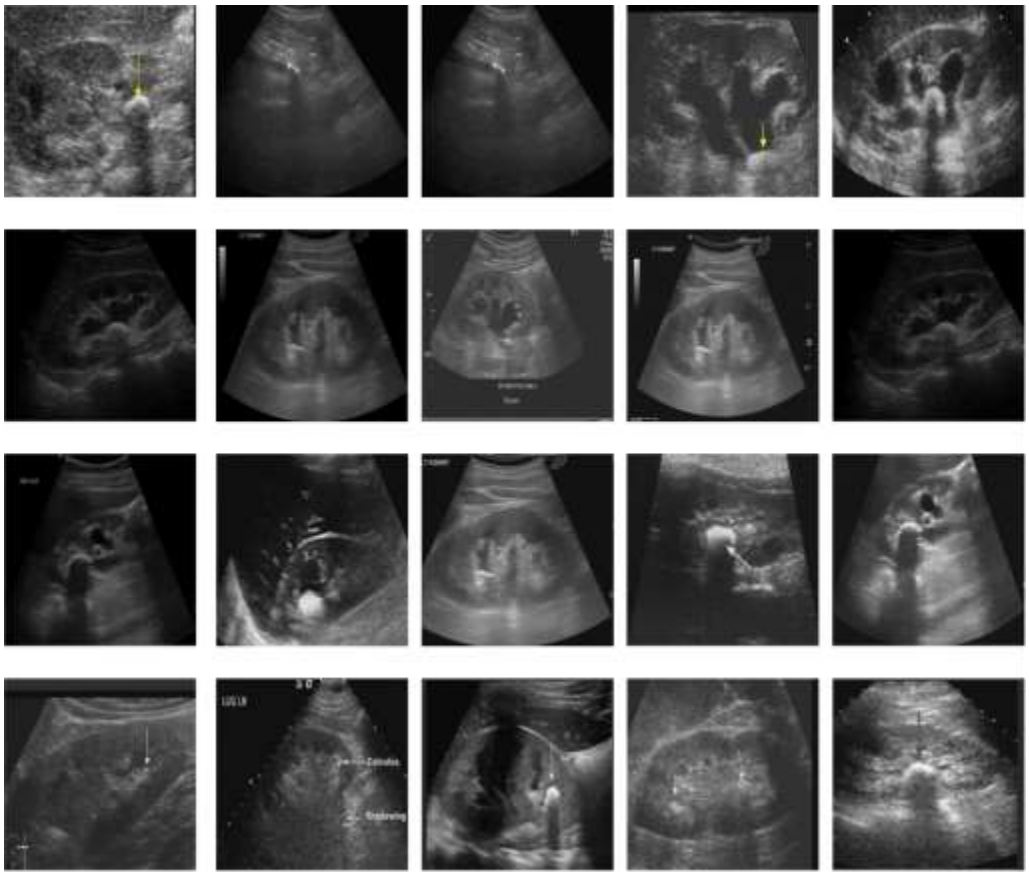

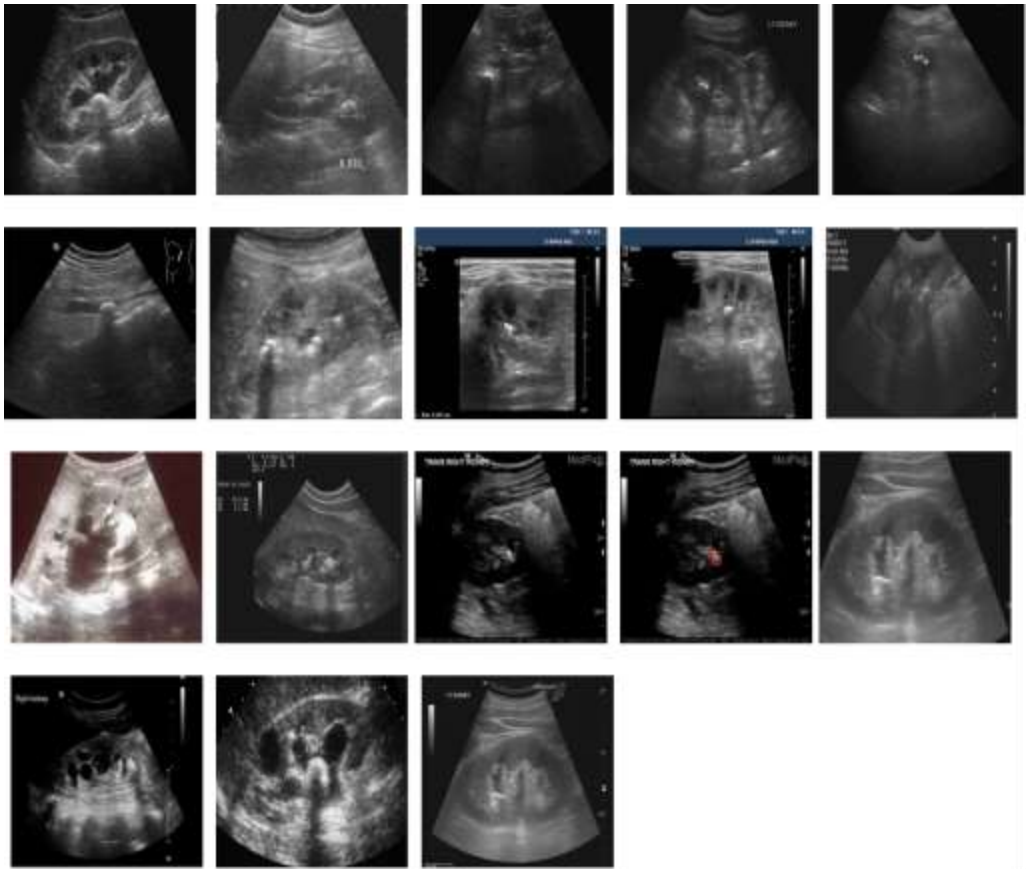

*Ultrasound Images of Multiple-stones Kidney*

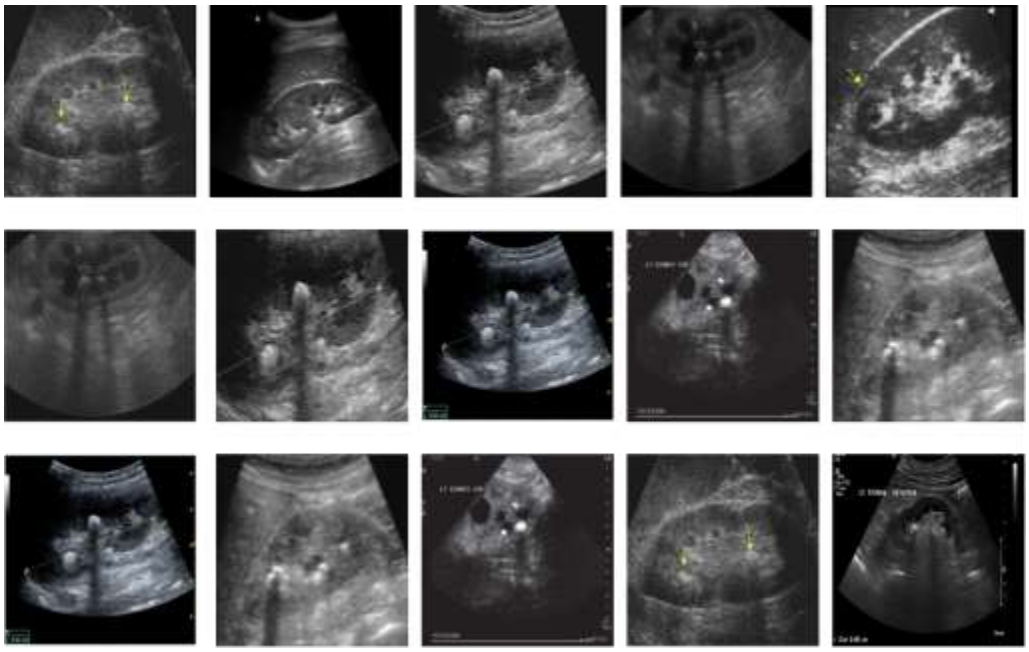

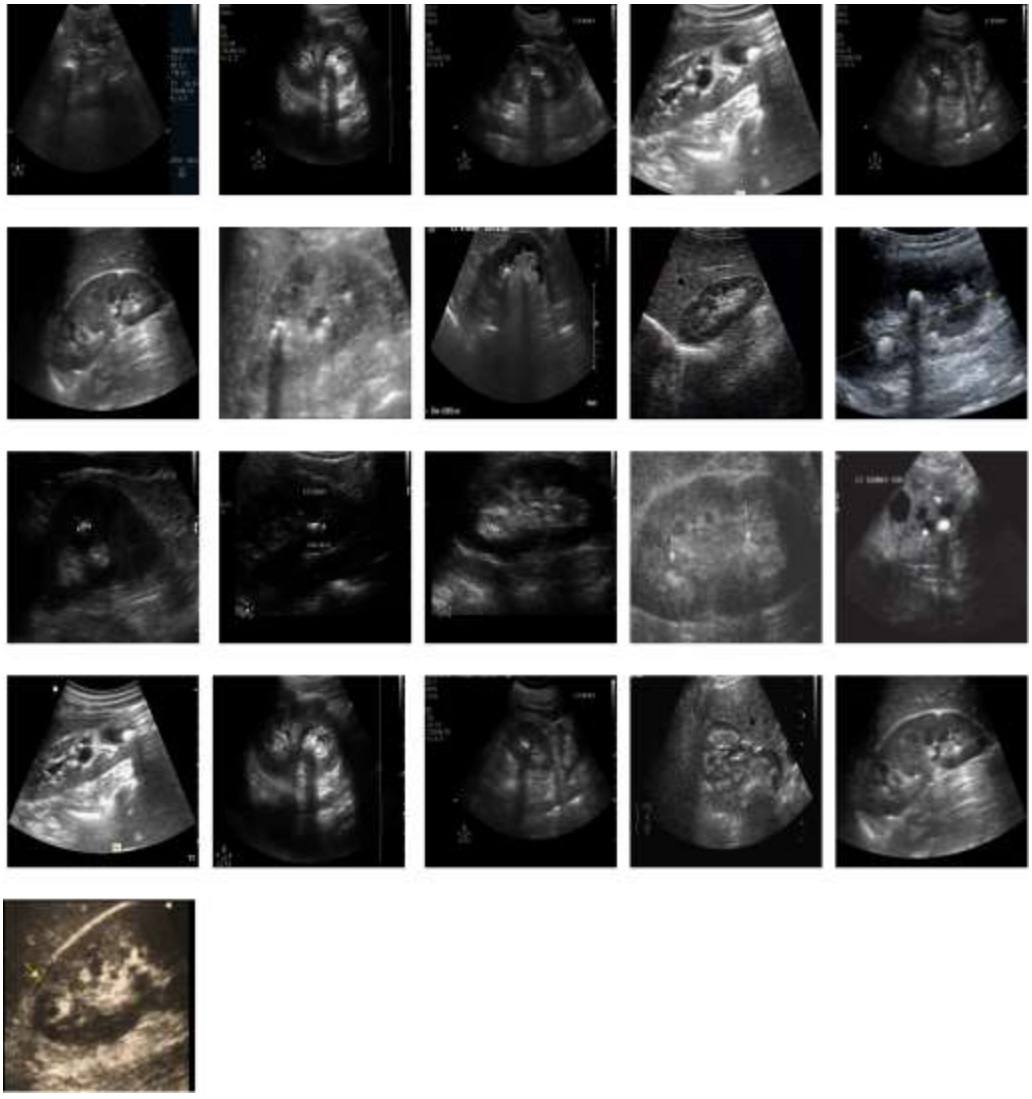

## Appendix II

# ANDROID MOBILE INTERFACE

The medical field has evolved beyond traditional boundaries with the advent of new technologies and tools. Android-based mobile devices are popular all over the world. In the modern era, hospitals are integrating their information system to enhance the quality of patient care services, using the concepts adopted worldwide. The technology used in the digital health system allows a large-scale network and image management systems, providing patient information, images to be shared and viewed remotely. Hence, an android interface for the system is developed for the end-users.

The mobile healthcare applications have brought new opportunities. In recent days, medical experts are adopting mobile applications to view or share images and reports. These applications are helpful to collaborate with other physicians for review discussions. About 15% of mobile applications are designed for healthcare professionals according to a survey carried out by research2guidance (Sarah Bruyn Jones, 2013).

Medical image analysis using smartphones focuses on enabling visualization and analysis through mobile devices. The system is implemented and tested on Samsung Note 9 cell phone, Exynos 9 Octa-core (2.7 GHz, Quad-core, M3 Mongoose, 1.7 GHz, Quad-core, Cortex A55) processor, 512 GB storage, 12 MP camera with 8 GB RAM running on Android version 8.1(Oreo) operating system. The interface is designed using MATLAB mobile application. Licensed MATLAB 2018b software with connectivity to the cloud is essential for the accessibility of MATLAB software

The initial setting for the connectivity between cloud and licensed MATLAB software is shown in Fig. AII.1 (a) and (b). The details like license number of MATLAB software and login id of a Mathworks account (https://mathworks.com) should be entered to connect to the MATLAB mobile application.

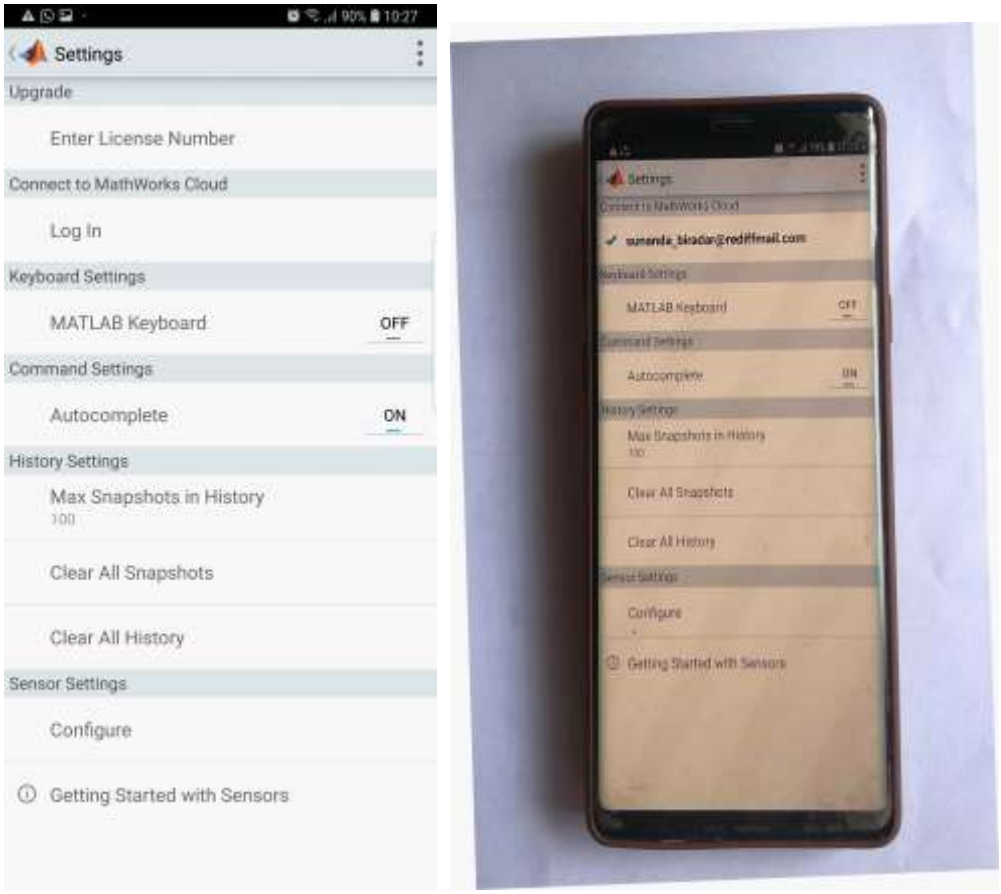


(a) (b)

Fig. AII.1 Setting in application (a) Snapshot of initial setting (b) Connectivity with the cloud

After connecting, files can be opened and executed in the mobile application. The execution of a file shows the instructions to the user to select the dataset. Initially, enter the image file name for testing as shown in Fig. AII.2(a). After reading the input it displays the result as shown in the snapshot Fig. AII.2(b).

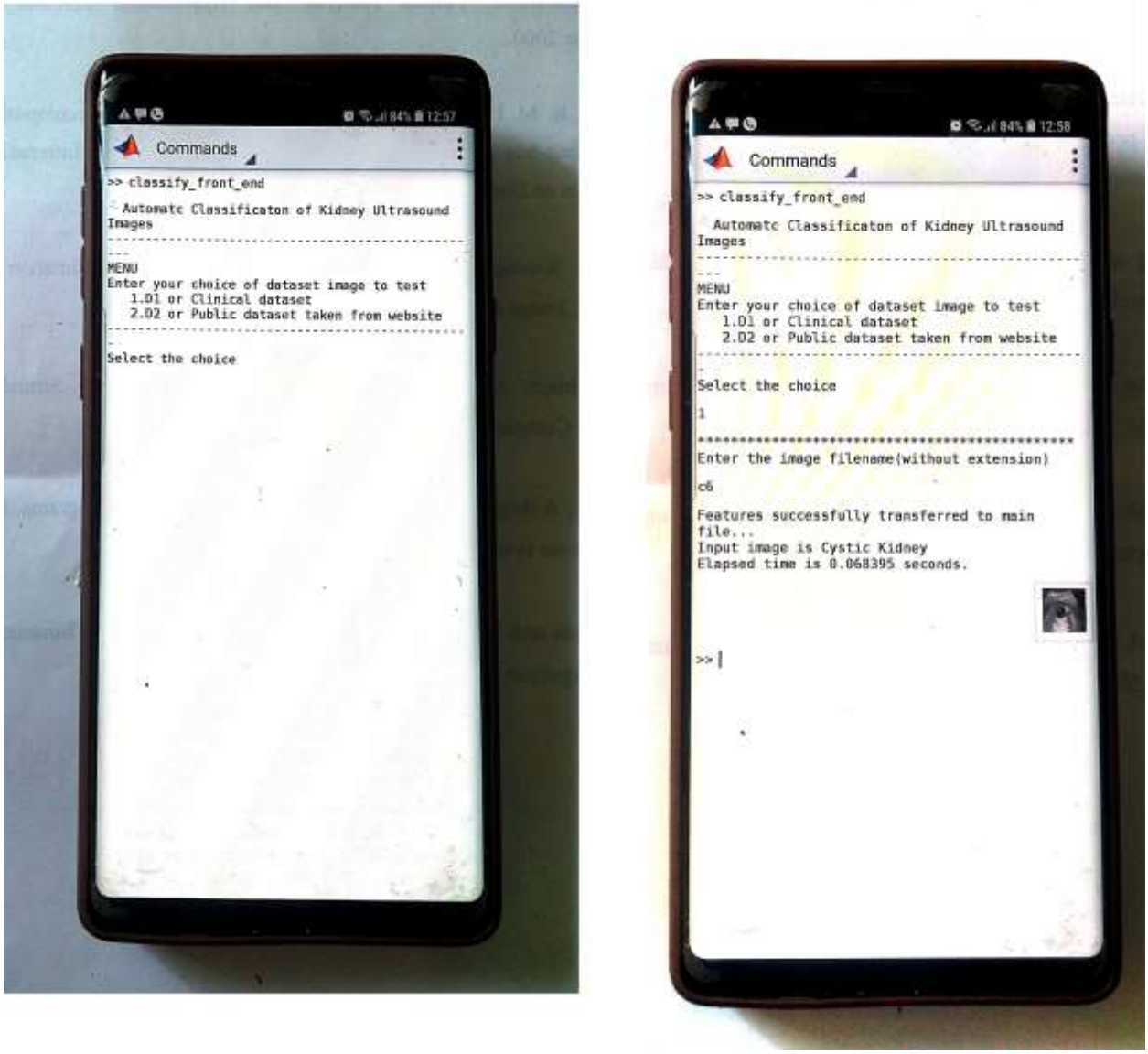


(a) (b)

Fig. AII.2 Snapshots of results (a) Display of instructions to specify the input (b) Output of the classifier

The execution time to perform the specified task and the input image is shown in a smaller size at the bottom line as shown in Fig. AII.2(b). The full view of the image can be seen by clicking on it as shown in Fig. AII.3.

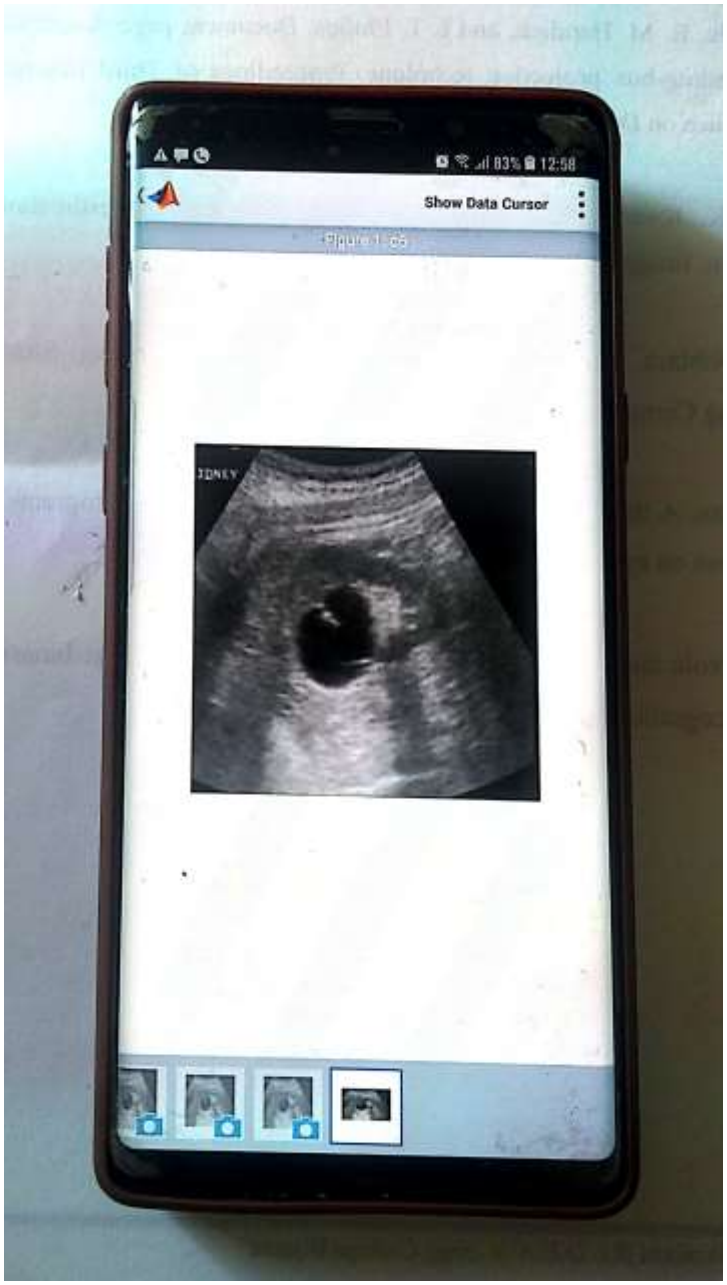


Fig. AII.3 Enlarged form of the processed image

Thus an easy to use mobile interface is developed for the end-users avoiding the requirement of computer to run the proposed algorithm for classification of segmented images using an automatic level set based segmentation method. The application offers various functionalities to the radiologists, medical professionals, and patients, such as real-time viewing of segmented and classified results on US images of kidney. The application facilitates collaboration with other medical experts and patients in an effective manner. It provides easy access for accurate diagnosis in real-time and thus helps in taking the right decision.

# Appendix III

# KRUSKAL WALLIS TEST AND CHI-SQUARE TEST

## Kruskal Wallis test

The Kruskal Wallis H test is a non-parametric test alternative to the one-way ANOVA. It is used to find out the statistically important variations among different sets of an independent variable on a continuous- dependent variable (sociostatatististics.com; Eva O., Oskar O., Jozef K., 2014). It is an improved version of the Mann-Whitney test. The Kruskal Wallis test supports the assessment of multiple independent sets.

The extracted features are tested for their statistically important variations between different features. This test is to justify that different features in a model have distinguishable importance in the proper classification. The working of Kruskal Wallis test is described in Algorithm AIII.1.

**Algorithm AIII.1: Kruskal Wallis test**.

*Input:* Extracted feature vector.

*Output:* Acceptance or rejection of the null hypothesis.

*Begin*

*Step 1:* Define the null hypothesis ($H_0$) and the alternative hypothesis ($H_1$)

$H_0$: The feature values are from populations with equal medians.

$H_1$: The feature values are from populations with the medians that are not all equal.

*Step 2:* Sort all the columns of a feature vector in ascending order.

*Step 3:* Assign rank to sorted feature values within a column.

*Step 4:* Find the sum of all the ranks for every column.

*Step 5:* Compute the Kruskal Wallis statistic using Eq. (A3.1).

$$K = \frac{12}{s(s+1)} \sum_{i=1}^{n} \frac{T_i^2}{s_i} - 3(s+1) \qquad \text{(A3.1)}$$

where, s = Total sum of samples in all the columns.

j = Number of groups(feature columns).

$T_i$ = Sum of the ranks for sample i.

$s_i$ = Size of sample i.

*Step 6:* Find the degree of freedom, j-1, and assign a level of significance alpha as 0.05 (5%).

*Step 7:* Obtain the critical value 'V' for the particular parameters in step 6 using chi-square table.

*Step 8:* Perform the comparison and

If K < V

then $H_0$ is accepted;

Otherwise $H_1$ is accepted and $H_0$ is rejected.

*End.*

Table AIII.1: Kruskal Wallis test on Tamura feature set

| **Normalized feature values (Sorted in ascending order)** | | | **Ranks assigned** | | |
|---|---|---|---|---|---|
| **Coarseness(f1)** | **Contrast(f2)** | **Direction(f3)** | **f1 rank** | **f2 rank** | **f3 rank** |
| 0 | 0 | 0 | 5.5 | 5.5 | 5.5 |
| 0.021 | 0 | 0 | 14.5 | 5.5 | 5.5 |
| 0.021 | 0 | 0.757 | 14.5 | 5.5 | 340 |
| 0.021 | 0 | 0.757 | 14.5 | 5.5 | 340 |
| 0.021 | 0 | 0.757 | 14.5 | 5.5 | 340 |
| 0.021 | 0 | 0.758 | 14.5 | 5.5 | 343.5 |
| 0.021 | 0 | 0.758 | 14.5 | 5.5 | 343.5 |
| 0.021 | 0.085 | 0.758 | 14.5 | 37.5 | 343.5 |
| 0.021 | 0.085 | 0.758 | 14.5 | 37.5 | 343.5 |
| 0.026 | 0.085 | 0.759 | 20 | 37.5 | 350 |
| 0.026 | 0.085 | 0.759 | 20 | 37.5 | 350 |
| 0.026 | 0.088 | 0.759 | 20 | 42.5 | 350 |
| 0.028 | 0.088 | 0.759 | 23 | 42.5 | 350 |
| 0.028 | 0.088 | 0.759 | 23 | 42.5 | 350 |
| 0.028 | 0.088 | 0.759 | 23 | 42.5 | 350 |

Table AIII.1 (Contd…): Kruskal Wallis test on Tamura feature set

| Normalized feature values (Sorted in ascending order) | | | Ranks assigned | | |
|---|---|---|---|---|---|
| **Coarseness(f1)** | **Contrast(f2)** | **Direction(f3)** | **f1 rank** | **f2 rank** | **f3 rank** |
| 0.034 | 0.088 | 0.759 | 25.5 | 42.5 | 350 |
| 0.034 | 0.088 | 0.759 | 25.5 | 42.5 | 350 |
| 0.059 | 0.123 | 0.76 | 27 | 69.5 | 355 |
| 0.079 | 0.123 | 0.762 | 29 | 69.5 | 360 |
| 0.079 | 0.123 | 0.762 | 29 | 69.5 | 360 |
| 0.079 | 0.123 | 0.762 | 29 | 69.5 | 360 |
| 0.08 | 0.132 | 0.762 | 32.5 | 74.5 | 360 |
| 0.08 | 0.132 | 0.762 | 32.5 | 74.5 | 360 |
| 0.08 | 0.143 | 0.762 | 32.5 | 81 | 360 |
| 0.08 | 0.143 | 0.762 | 32.5 | 81 | 360 |
| 0.083 | 0.163 | 0.762 | 35 | 95.5 | 360 |
| 0.096 | 0.163 | 0.762 | 47.5 | 95.5 | 360 |
| 0.096 | 0.163 | 0.763 | 47.5 | 95.5 | 370.5 |
| 0.096 | 0.163 | 0.763 | 47.5 | 95.5 | 370.5 |
| 0.096 | 0.181 | 0.763 | 47.5 | 103 | 370.5 |
| 0.102 | 0.182 | 0.763 | 52 | 108 | 370.5 |
| 0.102 | 0.182 | 0.763 | 52 | 108 | 370.5 |
| 0.102 | 0.186 | 0.763 | 52 | 114 | 370.5 |
| 0.102 | 0.186 | 0.764 | 52 | 114 | 378.5 |
| 0.102 | 0.186 | 0.764 | 52 | 114 | 378.5 |
| 0.111 | 0.186 | 0.764 | 56 | 114 | 378.5 |
| 0.111 | 0.186 | 0.764 | 56 | 114 | 378.5 |
| 0.111 | 0.186 | 0.765 | 56 | 114 | 383.5 |
| 0.114 | 0.186 | 0.765 | 58.5 | 114 | 383.5 |
| 0.116 | 0.186 | 0.765 | 62 | 114 | 383.5 |
| 0.116 | 0.203 | 0.765 | 62 | 126.5 | 383.5 |
| 0.116 | 0.203 | 0.765 | 62 | 126.5 | 383.5 |
| 0.116 | 0.203 | 0.766 | 62 | 126.5 | 390 |
| 0.116 | 0.203 | 0.766 | 62 | 126.5 | 390 |
| 0.117 | 0.222 | 0.766 | 66 | 135.5 | 390 |
| 0.117 | 0.222 | 0.766 | 66 | 135.5 | 390 |
| 0.117 | 0.222 | 0.766 | 66 | 135.5 | 390 |
| 0.126 | 0.222 | 0.767 | 72.5 | 135.5 | 394.5 |
| 0.126 | 0.225 | 0.767 | 72.5 | 139.5 | 394.5 |
| 0.14 | 0.225 | 0.769 | 77.5 | 139.5 | 403.5 |
| 0.14 | 0.227 | 0.769 | 77.5 | 141 | 403.5 |
| 0.14 | 0.242 | 0.769 | 77.5 | 147 | 403.5 |
| 0.14 | 0.245 | 0.769 | 77.5 | 150.5 | 403.5 |
| 0.143 | 0.259 | 0.771 | 81 | 156.5 | 410 |
| 0.152 | 0.259 | 0.771 | 84.5 | 156.5 | 410 |
| 0.152 | 0.259 | 0.771 | 84.5 | 156.5 | 410 |
| 0.152 | 0.259 | 0.771 | 84.5 | 156.5 | 410 |

Table AIII.1 (Contd…): Kruskal Wallis test on Tamura feature set

| Normalized feature values (Sorted in ascending order) | | | Ranks assigned | | |
|---|---|---|---|---|---|
| **Coarseness(f1)** | **Contrast(f2)** | **Direction(f3)** | **f1 rank** | **f2 rank** | **f3 rank** |
| 0.152 | 0.259 | 0.771 | 84.5 | 156.5 | 410 |
| 0.153 | 0.259 | 0.771 | 87.5 | 156.5 | 410 |
| 0.153 | 0.277 | 0.771 | 87.5 | 166.5 | 410 |
| 0.157 | 0.277 | 0.771 | 91 | 166.5 | 410 |
| 0.157 | 0.285 | 0.771 | 91 | 168 | 410 |
| 0.157 | 0.287 | 0.772 | 91 | 170 | 415.5 |
| 0.157 | 0.287 | 0.772 | 91 | 170 | 415.5 |
| 0.157 | 0.287 | 0.773 | 91 | 170 | 419.5 |
| 0.165 | 0.295 | 0.773 | 98 | 172 | 419.5 |
| 0.169 | 0.3 | 0.773 | 99 | 173 | 419.5 |
| 0.181 | 0.31 | 0.773 | 103 | 175 | 419.5 |
| 0.181 | 0.31 | 0.773 | 103 | 175 | 419.5 |
| 0.181 | 0.31 | 0.773 | 103 | 175 | 419.5 |
| 0.181 | 0.329 | 0.774 | 103 | 181.5 | 424 |
| 0.181 | 0.329 | 0.774 | 103 | 181.5 | 424 |
| 0.181 | 0.341 | 0.774 | 103 | 184 | 424 |
| 0.182 | 0.341 | 0.775 | 108 | 184 | 428 |
| 0.197 | 0.341 | 0.775 | 119 | 184 | 428 |
| 0.198 | 0.348 | 0.775 | 122 | 188 | 428 |
| 0.198 | 0.348 | 0.775 | 122 | 188 | 428 |
| 0.198 | 0.348 | 0.775 | 122 | 188 | 428 |
| 0.198 | 0.36 | 0.778 | 122 | 192.5 | 432 |
| 0.198 | 0.36 | 0.778 | 122 | 192.5 | 432 |
| 0.216 | 0.36 | 0.778 | 129 | 192.5 | 432 |
| 0.217 | 0.36 | 0.779 | 131 | 192.5 | 434 |
| 0.217 | 0.36 | 0.78 | 131 | 192.5 | 438.5 |
| 0.217 | 0.36 | 0.78 | 131 | 192.5 | 438.5 |
| 0.219 | 0.364 | 0.78 | 133 | 198.5 | 438.5 |
| 0.223 | 0.364 | 0.78 | 138 | 198.5 | 438.5 |
| 0.232 | 0.364 | 0.78 | 142.5 | 198.5 | 438.5 |
| 0.232 | 0.364 | 0.78 | 142.5 | 198.5 | 438.5 |
| 0.234 | 0.364 | 0.78 | 144 | 198.5 | 438.5 |
| 0.242 | 0.364 | 0.78 | 147 | 198.5 | 438.5 |
| 0.242 | 0.366 | 0.781 | 147 | 207 | 444 |
| 0.242 | 0.366 | 0.781 | 147 | 207 | 444 |
| 0.242 | 0.366 | 0.781 | 147 | 207 | 444 |
| 0.245 | 0.366 | 0.782 | 150.5 | 207 | 446.5 |
| 0.252 | 0.366 | 0.782 | 152.5 | 207 | 446.5 |
| 0.252 | 0.368 | 0.783 | 152.5 | 214 | 448 |
| 0.26 | 0.368 | 0.784 | 160.5 | 214 | 453 |
| 0.26 | 0.368 | 0.784 | 160.5 | 214 | 453 |
| 0.262 | 0.377 | 0.784 | 163.5 | 221.5 | 453 |
| 0.262 | 0.377 | 0.784 | 163.5 | 221.5 | 453 |
| 0.262 | 0.377 | 0.784 | 163.5 | 221.5 | 453 |

Table AIII.1 (Contd…): Kruskal Wallis test on Tamura feature set

| Normalized feature values (Sorted in ascending order) | | | Ranks assigned | | |
|---|---|---|---|---|---|
| **Coarseness(f1)** | **Contrast(f2)** | **Direction(f3)** | **f1 rank** | **f2 rank** | **f3 rank** |
| 0.262 | 0.377 | 0.784 | 163.5 | 221.5 | 453 |
| 0.323 | 0.377 | 0.784 | 178.5 | 221.5 | 453 |
| 0.323 | 0.377 | 0.784 | 178.5 | 221.5 | 453 |
| 0.323 | 0.379 | 0.784 | 178.5 | 226 | 453 |
| 0.323 | 0.379 | 0.785 | 178.5 | 226 | 461 |
| 0.342 | 0.379 | 0.785 | 186 | 226 | 461 |
| 0.366 | 0.388 | 0.785 | 207 | 233 | 461 |
| 0.366 | 0.388 | 0.785 | 207 | 233 | 461 |
| 0.366 | 0.388 | 0.785 | 207 | 233 | 461 |
| 0.366 | 0.388 | 0.785 | 207 | 233 | 461 |
| 0.366 | 0.388 | 0.785 | 207 | 233 | 461 |
| 0.366 | 0.401 | 0.786 | 207 | 239 | 466.5 |
| 0.372 | 0.405 | 0.786 | 217 | 241 | 466.5 |
| 0.372 | 0.405 | 0.786 | 217 | 241 | 466.5 |
| 0.372 | 0.405 | 0.786 | 217 | 241 | 466.5 |
| 0.384 | 0.411 | 0.787 | 228.5 | 243.5 | 469 |
| 0.384 | 0.411 | 0.788 | 228.5 | 243.5 | 470.5 |
| 0.386 | 0.42 | 0.788 | 230 | 245.5 | 470.5 |
| 0.391 | 0.42 | 0.789 | 236 | 245.5 | 474 |
| 0.398 | 0.426 | 0.789 | 237.5 | 247.5 | 474 |
| 0.398 | 0.426 | 0.789 | 237.5 | 247.5 | 474 |
| 0.436 | 0.462 | 0.789 | 249 | 258 | 474 |
| 0.437 | 0.462 | 0.789 | 250 | 258 | 474 |
| 0.442 | 0.462 | 0.79 | 251.5 | 258 | 479 |
| 0.442 | 0.489 | 0.79 | 251.5 | 260 | 479 |
| 0.453 | 0.494 | 0.79 | 253 | 261 | 479 |
| 0.455 | 0.516 | 0.79 | 254 | 270 | 479 |
| 0.46 | 0.518 | 0.79 | 255.5 | 271 | 479 |
| 0.46 | 0.522 | 0.791 | 255.5 | 276 | 486.5 |
| 0.495 | 0.522 | 0.791 | 262 | 276 | 486.5 |
| 0.498 | 0.522 | 0.791 | 263 | 276 | 486.5 |
| 0.504 | 0.522 | 0.791 | 264.5 | 276 | 486.5 |
| 0.504 | 0.522 | 0.791 | 264.5 | 276 | 486.5 |
| 0.512 | 0.523 | 0.791 | 267.5 | 279.5 | 486.5 |
| 0.512 | 0.523 | 0.791 | 267.5 | 279.5 | 486.5 |
| 0.512 | 0.533 | 0.791 | 267.5 | 282 | 486.5 |
| 0.512 | 0.538 | 0.791 | 267.5 | 283 | 486.5 |
| 0.521 | 0.549 | 0.791 | 272.5 | 285.5 | 486.5 |
| 0.521 | 0.549 | 0.792 | 272.5 | 285.5 | 493.5 |
| 0.524 | 0.574 | 0.792 | 281 | 288 | 493.5 |
| 0.54 | 0.574 | 0.792 | 284 | 288 | 493.5 |
| 0.588 | 0.574 | 0.792 | 290.5 | 288 | 493.5 |
| 0.588 | 0.59 | 0.793 | 290.5 | 292 | 501.5 |
| | | | | | |

Table AIII.1 (Contd…): Kruskal Wallis test on Tamura feature set

| Normalized feature values (Sorted in ascending order) | | | Ranks assigned | | |
|---|---|---|---|---|---|
| **Coarseness(f1)** | **Contrast(f2)** | **Direction(f3)** | **f1 rank** | **f2 rank** | **f3 rank** |
| 0.596 | 0.591 | 0.793 | 294.5 | 293 | 501.5 |
| 0.596 | 0.601 | 0.793 | 294.5 | 300.5 | 501.5 |
| 0.597 | 0.601 | 0.793 | 296.5 | 300.5 | 501.5 |
| 0.597 | 0.646 | 0.793 | 296.5 | 304.5 | 501.5 |
| 0.598 | 0.646 | 0.793 | 298.5 | 304.5 | 501.5 |
| 0.598 | 0.656 | 0.793 | 298.5 | 306 | 501.5 |
| 0.61 | 0.666 | 0.793 | 302.5 | 308 | 501.5 |
| 0.61 | 0.683 | 0.793 | 302.5 | 312.5 | 501.5 |
| 0.664 | 0.683 | 0.793 | 307 | 312.5 | 501.5 |
| 0.669 | 0.686 | 0.793 | 310 | 315 | 501.5 |
| 0.669 | 0.686 | 0.793 | 310 | 315 | 501.5 |
| 0.669 | 0.686 | 0.794 | 310 | 315 | 509 |
| 0.745 | 0.689 | 0.794 | 333 | 317 | 509 |
| 0.745 | 0.691 | 0.794 | 333 | 318 | 509 |
| 0.745 | 0.711 | 0.795 | 333 | 319.5 | 512.5 |
| 0.745 | 0.711 | 0.795 | 333 | 319.5 | 512.5 |
| 0.745 | 0.719 | 0.795 | 333 | 321.5 | 512.5 |
| 0.756 | 0.719 | 0.795 | 338 | 321.5 | 512.5 |
| 0.763 | 0.734 | 0.796 | 370.5 | 324.5 | 516 |
| 0.763 | 0.734 | 0.796 | 370.5 | 324.5 | 516 |
| 0.763 | 0.734 | 0.796 | 370.5 | 324.5 | 516 |
| 0.763 | 0.734 | 0.797 | 370.5 | 324.5 | 522 |
| 0.763 | 0.736 | 0.797 | 370.5 | 327.5 | 522 |
| 0.763 | 0.736 | 0.797 | 370.5 | 327.5 | 522 |
| 0.822 | 0.743 | 0.797 | 535 | 329.5 | 522 |
| 0.822 | 0.743 | 0.797 | 535 | 329.5 | 522 |
| 0.822 | 0.755 | 0.797 | 535 | 336.5 | 522 |
| 0.822 | 0.755 | 0.797 | 535 | 336.5 | 522 |
| 0.822 | 0.759 | 0.797 | 535 | 350 | 522 |
| 0.822 | 0.766 | 0.797 | 535 | 390 | 522 |
| 0.822 | 0.766 | 0.798 | 535 | 390 | 529 |
| 0.825 | 0.768 | 0.798 | 540.5 | 398.5 | 529 |
| 0.845 | 0.768 | 0.798 | 543.5 | 398.5 | 529 |
| 0.845 | 0.768 | 0.798 | 543.5 | 398.5 | 529 |
| 0.862 | 0.768 | 0.825 | 547.5 | 398.5 | 540.5 |
| 0.862 | 0.768 | 0.825 | 547.5 | 398.5 | 540.5 |
| 0.862 | 0.768 | 0.825 | 547.5 | 398.5 | 540.5 |
| 0.862 | 0.798 | 0.957 | 547.5 | 529 | 552.5 |
| 0.862 | 0.936 | 0.957 | 547.5 | 551 | 552.5 |
| 0.862 | 0.978 | 0.964 | 547.5 | 555 | 554 |

Sum of the ranks for column(f1 rank) $T_1$= 34750.5

Sum of the ranks for column(f2 rank) $T_2$= 38566

Sum of the ranks for column(f3 rank) $T_3$= 80973.5

$T_i$ is calculated as the sum of the ranks for the feature ranks columns. n is the total number of sample values taken. Applying the formula mentioned in Algorithm A3.1, we get the statistic

K= 276.7. The critical value V obtained from chi-square table is 5.991 for degree of freedom 2 at 5% level of significance. Therefore K>V and null hypothesis $H_0$ is rejected as shown in Algorithm A3.1. Hence, the three different Tamura features have an important significant difference. They have not come from a population with a common median. Each of the features contributes significantly in classifying the renal ultrasound medical images.

## *Chi-Square test*

Chi-Square, test of goodness is proposed by Pearson. It is a non-parametric test, mainly applied to determine, how obtained values are significantly varying from the expert-determined standard values. The test compares the obtained values distribution with probability distribution of actual values (Kothari C. R., 2004).

Chi-square test is used to evaluate the appropriateness of stone size calculated experimentally and the actual values obtained by medical experts. The various steps involved in chi-square test are shown in Algorithm AIII.2.

**Algorithm AIII.2: Chi-square test**.

*Input:* Observed value of stone area (O), expected value ($E_x$) mentioned by medical expert and predefined level of significance.

*Output:* Acceptance or rejection of null hypothesis.

*Begin*

*Step 1:* Define null hypothesis ($H_0$)

$H_0$: Values of the stone area calculated by the algorithm and the values obtained by medical expert are similar.

*Step 2:* Compute chi-square statistics using the O and $E_x$ values specified in Table 5.3 using the formula specified in Eq.A3.2.

$$\chi 2 = \sum \frac{(O - E_x)^2}{E_x} \quad \text{(A3.2)}$$

*Step 3:* Define level of significance (s) and obtain a degree of freedom (d) as in Eq. (A3.3) and Eq. (A3.4) respectively.

$$s = 5\% = 0.05 \quad \text{(A3.3)}$$

$$d = (n_r - 1)(n_c - 1) \quad \text{(A3.4)}$$

where $n_r$ and $n_c$ refer to the number of rows and number of columns in Table A3.2.

*Step 4:* Perform goodness of fit test by the computed value of $\chi^2$ and $\chi_f^2$ obtained value by a chi-square table, for a particular degree of freedom and level of significance.

If $\chi^2 < \chi_f^2$

then $H_0$ is accepted;

otherwise, $H_0$ is rejected.

*End.*

Table AIII.2. Chi-square test on sample values of renal calculus area

| Image sample | Stone size ( in mm$^2$) | | $\frac{(0 - E_x)^2}{E_x}$ |
|---|---|---|---|
| | Experimentally obtained (O) | Obtained by an expert (E) | |
| I1 | 11.54 | 10.75 | 0.058 |
| I2 | 7.75 | 8.46 | 0.060 |
| I3 | 12.82 | 13.77 | 0.066 |
| I4 | Stone1=13.92 | Stone1=13.21 | 0.038 |
| | Stone2=11.43 | Stone2=11.9 | 0.019 |
| I5 | 11.19 | 10.96 | 0.005 |
| I6 | 15.0 | 14.63 | 0.009 |
| I7 | 14.69 | 15.74 | 0.070 |
| I8 | 10.98 | 11.23 | 0.006 |
| | | Chi-square = | 0.33 |

Chi-square test is performed on obtained and expert determined values of renal stone sizes as specified in Algorithm AIII.2. Table AIII.2 shows the details of eight sample renal stone images considered for the test. The chi-square distribution table value for a 5% level of significance is 15.507. The obtained value is lesser than the table value. i.e. 0.33 < 15.507. Hence, the null hypothesis $H_0$ is accepted. The acceptance indicates that the computed values are statistically acceptable.

# AUTHOR'S PUBLICATIONS

| | |
|---|---|
| **No. of Journal Papers ( International)** | **03** |
| **No. of Book Chapters** | **02** |
| **No. of Conference papers (International)** | **02** |
| **No. of Conference papers (National)** | **01** |
| **No. of Journal Papers Under review** | **01** |

## Grants Utilized for the Research

The research work is carried under the financial assistance of Vision Group of Science and Technology, Government of Karnataka, under Research Grant Scheme for Scientists/Faculty(RGS/F) GRD No.729/2017-18 in the year 2017-2018. I would like to thank Vision Group of Science and Technology, Karnataka, India for the financial assistance of Rs.**5,00,000.00**.

## Journal papers:

[1] Akkasaligar Prema T., Biradar Sunanda, ***"Analysis of Polycystic Kidney Disease in Medical Ultrasound Images"***, International Journal of Medical Engineering and Informatics, vol. 10(1), 2018, pp. 49-64.

[2] Akkasaligar Prema T., Biradar Sunanda, ***"Classification of Medical Ultrasound Images of Kidney"***, International Journal of Computer Applications, Special Issue on ICICT 2014, pp. 24-28.

[3] Akkasaligar Prema T., Biradar Sunanda, "***Automatic Segmentation and Analysis of Renal Calculi in Medical Ultrasound Images***", Pattern Recognition and Image Analysis, vol. 30(4), 2020 (under press).

## Book chapters:

[1] Akkasaligar Prema T., Biradar Sunanda, "***Automatic Kidney Cysts Segmentation in Digital Ultrasound Images***", In: Shukla A. (ed.), Chapter 4, Medical Imaging Methods, Springer Nature, Singapore Ple. Ltd., 2019, pp. 97-117.

[2] Akkasaligar Prema T., Biradar Sunanda, "***Segmentation of Kidney Stones in Medical Ultrasound Images***", Recent Trends in Image Processing and Pattern Recognition, RTIP2R-2018, In: Santosh K, Hegadi R. (eds.), Chapter 18, Communications in Computer and Information Science, vol. 1036, part 2, Springer Nature, Singapore Ple. Ltd., 2019, pp. 200-208.

## Conference Papers:

[1] Akkasaligar Prema T., Biradar Sunanda, Kumbar Veena, "***Kidney Stone Detection in Computed Tomography Images***", IEEE International Conference On Smart Technology for Smart Nation, 2017, REVA University, Bangalore, Karnataka, India, 17-19 August 2017, pp. 886-889.

[2] Akkasaligar Prema T., Biradar Sunanda, "***Diagnosis of Renal Calculus Disease in Medical Ultrasound Images***", IEEE International Conference on Computational Intelligence and Computing Research-2016, Agni College of Technology, Chennai, Tamilnadu, India, 15-17 Dec. 2016, pp. 948-952.

[3] Akkasaligar Prema T., Biradar Sunanda, "***Automatic Segmentation of Kidney Cysts in Medical Ultrasound Images***", UGC Sponsored National Conference on Recent Trends in Image Processing and Pattern Recognition-2016, Karnataka Arts, Science and Commerce College, Bidar, Karnataka, India, 2-3 April 2016, pp. 140-147.

## Journal Papers (Under Review) :

[1] Akkasaligar Prema T., Biradar Sunanda, *"**Feature Extraction and Classification of Diseased Digital Kidney Ultrasound Images: A Hybrid Approach**"*, Communicated to Arab Journal of Engineering.

# REFERENCES


[1]. Adibi A., Adibi I. and Khosravi P. "Do kidney sizes in ultrasonography correlate to glomerular filtration rate in healthy children? ", Australas, Radiology, vol. 51, 2007, pp. 555–559.

[2]. Agarwal T., Tiwari M., Lamba S., "Modified histogram based contrast enhancement using homomorphic filtering for medical images", IEEE International Advance Computing Conference (IACC), Gurgaon, New Delhi, India, 2014, pp. 964-96.

[3]. Andrzej Pawel Wieczorek, Magdalena Maria Woźniak, Janusz F. Tyloch, "Errors in the ultrasound diagnosis of the kidneys, ureters and urinary bladder", Journal of Ultrasonography vol. 13, 2013, pp. 308–318.

[4]. Arlene B. Chapman and Wenjing Wei, "Imaging approaches to patients with polycystic kidney disease", Seminars in Nephrology, vol. 31(3), May 2011, pp. 237–244.

[5]. Arpana M. Kop and Ravindra Hegadi, "Kidney Segmentation from ultrasound images using gradient vector force", IJCA special issue on RTIPPR, 2010, pp. 104- 109.

[6]. Ashish K. Rudra , Ananda S. Chowdhury, Ahmed Elnakib, Fahmi Khalifa, Ahmed Soliman, Garth Beache, Ayman El-Baz , "Kidney segmentation using graph cuts and pixel connectivity", Pattern Recognition Journal, vol. 34, 2013 , pp. 1470–1475.

[7]. Bamber J. C. and C. Daft, "Adaptive filtering for reduction of speckle in ultrasound pulse-echo images", Ultrasonics, 1986, pp. 41-44.

[8]. C.B. Burckhardt, "Speckle in ultrasound B-mode scans", IEEE Trans. Sonics and Ultrasonics, vol. 25 (1), 1978, pp. 1–6.

[9]. C.R. Kothari, Gaurav Garg, "Research Methodology Methods & Techniques", Fourth Edition, New Age International publisher, New Delhi , 2019, pp. 235-286.

[10]. Candemir S, Jaeger S, Palaniappan K.., Musco J. P., Singh R. K., Xue Z., Karargyris A., Antani S., Thoma G., McDonald C. J., "Lung segmentation in chest radiographs using anatomical atlases with nonrigid registration", IEEE Trans. Medical Imaging, vol. 33(2), Feb. 2014, pp. 577-590 .

[11]. Nicolau C, Torra R, Badenas C, et al.., "Sonographic patterns of recessive polycystic kidney disease in young adults, differences from dominant form", Nephology Dialysis Transplantation, vol. 15, 2000, pp. 1373-1378.

[12]. Carlos S. Mendoza, Xin Kang, Nabile Safdar, Emmarie Myers, Craig A. Peters, Marius George Linguraru, " Kidney segmentation in ultrasound via genetic initialization and active shape models with rotation correction", IEEE International Symposium on Biomedical Imaging, April 2013, pp.1-8.

[13] Carol M. Rumack, Deborah Levine, "Diagnostic Ultrasound", 5th edition, vol. 1, Elsevier, 2018, pp.128-145.

[14]. Carovac A, Smajlovic F, Junuzovic D., "Application of ultrasound in medicine", Acta Informatica Medica, vol. 19 (3), September 2011, pp.168–171.

[15]. Chakravorty R. C., "The treatment of wounds and abscesses in the Sutrasthanam of the Sushrutasamhita", Indian Journal of Surgery, vol. 31, 1969, pp.261–266.

[16]. Chakravorty R.C., "Urinary stones: their cause and treatment", as described in the SUSHRUTA SAMHITA.
http://www.biusante.parisdescartes.fr/sfhm/hsm/HSMx1982x017xspec2/HSMx1982x017xspec2x0328.pdf.

[17]. Chan T, Vese L, "Active contours without edges", IEEE Trans. Image Processing, vol.10 (2), 2001, pp. 266–277.

[18]. Chang, L.W., Chen, H.W. and Ho, J.R. "Reconstruction of 3D medical images: A nonlinear interpolation technique for reconstruction of 3D medical images", Computer Vision, Graphics, and Image Processing, vol. 53(4), 1991, pp.382–391.

[19]. Chen, C. J., Pai, T.W., Fujita, H., Lee, C.H., Chen, Y.T., Chen K. S., and Chen, Y. C., "Stage diagnosis for Chronic Kidney Disease based on ultrasonography", 11th IEEE International Conference on Fuzzy Systems and Knowledge Discovery, 2014, pp. 526-530.

[20]. Chia- Hsiang Wu, Yung-Nien Sun, "Segmentation of kidney from ultrasound B-mode images with texture-based classification", Computer Methods and Programs in Biomedicine Journal, vol. 84, 2006, pp. 114-123.

[21]. W. Ardiatna, A. H. Saputro and D. Soeharso Soejoko, "Analysis of kidney ultrasound images characterization using statistical moment descriptor", 2018 International Conference on Computer, Control, Informatics and its Applications (IC3INA), Tangerang, Indonesia, 2018, pp. 17-22.

[22]. Chi Jim Chen, Tun Wen Pai, Hui-Huang Hsu, Chien Hung Lee, Kuo-Su Chen and Yung Chih Chen, "Prediction of chronic kidney disease stages by renal ultrasound imaging, Enterprise Information Systems", vol.14 (2), 2020, pp.178-195.

[23] Kuo C., Chang C., Liu K., et al., "Automation of the kidney function prediction and classification through ultrasound-based kidney imaging using deep learning", NPJ Digital Medicine, vol. 29, 2019, pp.1-9.

[24]. Cobbold, Richard S. C., "Foundations of biomedical ultrasound", Oxford University Press. 2007, pp. 422–423.

[25]. Cohen L.D. and Cohen I., "A finite element method applied to new active contour models and 3D reconstruction from cross sections", In proc. 3rd International Conference on Computer Vision, Osaka, Japan, 1990, pp. 587–591.

[26]. Cohen, L.D. and Cohen, I., "Finite element methods for active contour models and balloons for 2D and 3D images", IEEE Trans. on Pattern Analysis and Machine Intelligence vol. 15(11), 1993, pp.1131–1147.

[27]. Cohen, L.D., "On active contour models and balloons CVGIP", Image Understanding, vol. 53(2), 1991, pp. 211– 218.

[28]. Diabetes, http://www.who.int/news-room/fact-sheets/detail/diabetes, Accessed June 10, 2019.

[29]. Dimopoulos C, Gialas A, Likourinas M, Androutsos G, Kostakopoulos A., "Hippocrates: founder and pioneer of urology", British Journal of Urology, vol. 52(2), 1980, pp.73–74.

[30]. Global Health Observatory (GHO) data, http://www.who.int/gho/hiv/en/, Accessed May 27, 2019

[31]. Goel R. and Jain A., "Improved detection of kidney stone in ultrasound images using segmentation techniques" In: Kolhe M., Tiwari S., Trivedi M., Mishra K. (eds), Advances in Data and Information Sciences. Lecture Notes in Networks and Systems, Springer, Singapore, vol. 94, 2020, pp. 623-641.

[32] Gonzalez R. C. and Woods R. E. "Digital Image Processing", Second Edition, Pearson Edu., 2002, pp. 66-84.

[33]. H. M. Pollack and B. L. McClennan, "Clinical Urography", Second Edition, W. B. Saunders company, 2000, pp.1817-1823.

[34]. Hagen-Ansert S., Urinary System, "Textbook of Diagnostic Sonography", Diagnostic Ultrasound, Elsevier Mosby, Seventh Edition, 2011, pp.1-110.

[35]. Hélénon O., Correas J.M., Balleyguier C., Ghouadni M., and Cornud F., "Ultrasound of renal tumors", European Radiology, vol. 11(10), 2001, pp. 1890–1901.

[36]. Hiremath P. S. and Tegnoor J. R., " Fuzzy logic based detection of follicles in ultrasound images of ovaries, Proc. of Fifth Indian International Conference on Artificial Intelligence (IICAI-2011), 14-16 Dec 2011, Tumkur, Karnataka, India, pp. 178-189.

[37]. Hiremath P. S., Prema T. Akkasaligar and Sharan Badiger, "Despeckling medical ultrasound images using the contourlet transform", Proc. Indian International Conference on Artificial Intelligence, Tumkur, India, 16-18 Dec. 2009, pp. 1814-1827.

[38]. Hiremath P. S., Prema T. Akkasaligar and Sharan Badiger, "Speckle Noise Reduction in Medical Ultrasound Images", Advancements and Breakthroughs in Ultrasound Images in Tech Publishers, Crortia, 5th June 2013, pp. 201-241.

[39]. Hiremath P. S., Prema T. Akkasaligar and Sharan Badiger, "Visual enhancement of digital ultrasound images using multiscale wavelet domain", Int. J. of Pattern Recognition and Image Analysis, vol. 20(3), July 2010, pp.303-315.

[40]. Hiremath P.S., Akkasaligar Prema T., Badiger Sharan, "Speckle reducing contourlet transform for medical ultrasound images", World Academy of Science, Engineering and Technology-Special Journal Issue, 2011, pp.1217 – 1224.

[41]. Huang J., Yang H., Chen Y. ,Tang L., "Ultrasound Kidney Segmentation with a Global Prior Shape ", Journal of Visual Communication and Image Representation vol. 24, 2013, pp. 937-943.

[42] J. Alison Noble and Djamal Boukerroui, "Ultrasound image segmentation: a survey", IEEE Transactions on Medical Imaging, vol. 25(8), August 2006, pp. 987-1010.

[43]. J. K. Udupa, and V.R. LeBlanc., "Methodology for Evaluating Image Segmentation Algorithms," SPIE Medical Imaging, 2002, pp.266-277.

[44]. Jack W. McAninch, and Tom F. Lue, "Smith & Tanagho's General Urology", Eighteenth edition, McGraw Hill Medical, 2013, pp.170-181.

[45]. Jeyakumar V. and Hasmi M. K., "Quantitative analysis of segmentation methods on ultrasound kidney image", Int. J. Advanced Research in Computer and Communication Engineering, vol. 2(5), 2013, pp. 2319-5940.

[46]. Jie Wu, Skip Poehlman, Michael D. Noseworthy, and Markad V. Kamath, "Texture feature based automated seeded region growing in abdominal MRI segmentation", Journal of Biomedical Science and Engineering, vol. 2, 2009, pp. 1-8.

[47]. Jyoti Verma, Madhwendra Nath, Priyanshu Tripathi, and K. K. Saini, "Analysis and identification of kidney stone using kth nearest neighbour (KNN) and support vector machine (SVM) ", Pattern Recognition and Image Analysis, vol. 27(3), 2017, pp. 574–580.

[48]. K. B. Raja, M. Madheswaran, and K. Thyagarajah, "A general segmentation scheme for contouring kidney region in ultrasound kidney images using improved higher order spline interpolation", Int. J. Biological and Life Sciences, vol. 2(2), 2006, pp.168-175.

[49]. K. Kumar, and Abhishek B., "Artificial neural network for diagnosis of kidney stone disease", Int. J. Information Technology and Computer Science, vol. 7, 2012, pp. 20–25.

[50]. K. M. Meiburger, U. R. Acharya and F. Molinari, Automated localization and segmentation techniques for B-mode ultrasound images: A review Computers in Biology and Medicine, vol. 92, 2018, pp. 210-235

[51]. K. B. Raja, M. Madheswaran., and K. Thyagarajah, "Quantitative and qualitative evaluation of us kidney images for disorder classification using multi-scale differential features", ICGST-BIME Journal, vol. 7(1), 2000, pp. 1-8.

[52] Kanishka Sharma, Christian Rupprecht, Anna Caroli, et al., "Automatic segmentation of kidneys using deep learning for total kidney volume quantification in autosomal dominant polycystic kidney disease", Scientific Reports vol.7:2049, 2017, pp. 1-10.

[53]. Kerre E. E. and Nachtegael M., Fuzzy Techniques in Image Processing, Springer, Heidelberg, vol. 52, 2000, pp.211-285.

[54]. Khademi A., Sahba F., Venetsanopoulos A. and Krishnan S., "Region, lesion and border-based multiresolution analysis of mammogram lesions", Proc. of the Sixth International Conference on Image Analysis and Recognition (ICIAR), Halifex,

Canada, 6-8 July, 2009, pp. 802-813.

[55]. Kyongtae T Bae, Hongliang Sun, June Goo Lee, et al. , "Novel Methodology to evaluate renal cysts in polycystic kidney disease", American Journal of Nephrology, vol. 39, 2014, pp.210–217.

[56]. Li L., Ross P., Kruusmaa M., and Zheng X., "A comparative study of ultrasound image segmentation algorithms for segmenting kidney tumors", Proc. 4th International Symposium on Applied Sciences in Biomedical and Communication Technologies, 2011, pp. 1-5.

[57]. Li C., Xu C., Gui C., and Fox M. D., "Level set evolution without re-initialization: A new variational formulation", IEEE Trans. Imag. Process., vol. 19(12), 2010, pp. 3243–3254.

[58]. Lin, W.C. and Chen, S.Y., "A new surface interpolation technique for reconstructing 3D objects from serial cross-sections", Computer Vision, Graphics, and Image Processing vol. 48, 1989, pp.124–143.

[59]. Loizou C.P., Pattichis,Pantziaris M.,Tyllis T.,and Nicolaides A., "quality evaluation of ultasound imaging in the carotid artery based on normalization and speckle reduction filtering", International Federation for Medical and Biological Engineering, 2006, pp. 414-426.

[60]. Lucisano G., Comi N., Pelagi E., Cianfrone P., Fuiano L., and Fuiano G., "Can renal sonography be a reliable diagnostic tool in the assessment of chronic kidney disease?", J. Ultrasound Med. vol. 34, 2015, pp. 299–306.

[61]. M. A. Fischler and R. A. Elschlager, "The Representation and matching of pictorial structures," IEEE Transactions on Computers, vol. 100(1), 1973, pp. 67-92.

[62] M. B. Subramanya, S.Mukherjee, and M. Saini, "SVM-based CAC system for B-mode kidney ultrasound images", Journal of Digital Imaging, vol. 28, 2015, pp. 448-458.

[63]. M. Marsousi, Konstantinos N., Plataniots and S. Stergiopoulos, "Shape- based kidney detection and segmentation in three-dimensional abdominal ultrasound images", IEEE International Symposium, 2014, pp. 2890-2894.

[64]. Mahmoud Ramze Rezaee, Pieter M. J. vander Zwet, Boudewijn P. F. Lelieveldt, et al., "A multiresolution image segmentation technique based on pyramidal segmentation and fuzzy clustering", IEEE Transactions on Image Processing, vol. 9(7), July 2000, pp. 1238-1248.

[65]. Max Roser and Hannah Ritchie, Cancer, July 2015, https://ourworldindata.org/cancer, Accessed June 10, 2019

[66]. Michell A. R., "Urolithiasis-historical, comparative and pathophysiological aspects: a review", Journal of the Royal Society of Medicine, vol. 82(11), 1989, pp.669–672.

[67]. Monika Gradzik, Mariusz Niemczyk, Marek Gołębiowski, and Leszek Pączek, "Diagnostic imaging of autosomal dominant polycystic kidney disease", Polish J. Radiology, vol. 81, 2016, pp. 441-453.

[68]. N. R. Dunnick, Carl M. Sandler, and Jefry H. N.,"Text Book of Uroradiology", Fifth edition, Lippincott Williams and Wilkins Koloters Kluwer Business, 2013, pp. 138-224.

[69]. Nascimento A. B., Mitchell D. G., Zhang X.-M., Kamishima T., Parker, L., and Holland, G. A., "Rapid MR Imaging Detection of Renal Cysts: Age-based Standards", Radiology, vol. 221(3), 2001, pp. 628–632.

[70]. Nedeljkovic I., "Image classification based on fuzzy logic", The International Archives of the Photogrammetry, Remote Sensing and Spatial Information Sciences, vol. 34, 2004, pp.173-179.

[71]. Neil R. Owen, Oleg A. Sapozhnikov, Michael R. Bailey, Leonid Trusov and Lawrence A. Crum, "Use of acoustic scattering to monitor kidney stone fragmentation during shock wave lithotripsy", Proc. IEEE International Ultrasonics Symposium, Vancouver, Canada, 2006, pp. 736 – 739.

[72] O'Neill W. C., Renal relevant radiology: use of ultrasound in kidney disease and nephrology procedures. Clin. J. Am. Soc. Nephrol.: CJASN vol. 9, 2014, pp. 373–381.

[73]. Osher S., and Fedkiw, "Level set methods and dynamic implicit surfaces", New York:Springer-Verlag, 2002, pp.65-77.

[74]. P. R. Tamilselvi and P. Thangaraj, "Computer aided diagnosis system for stone detection and early detection of kidney stones", Journal of Computer Science Publications, vol. 7 (2), 2011, pp. 250-254.

[75]. P. R. Tamilselvi and P. Thangaraj, "Segmentation of calculi from ultrasound kidney images by region indicator with contour segmentation method", Global Journal of Computer Science and Technology, vol. 11(22), Dec. 2011, pp. 1-10.

[76]. P. R. Tamilselvi, "Effective segmentation approaches for renal calculi segmentation", International Journal of Science and Research (IJSR), vol. 2, June 2013, pp. 76-79.

[77]. P.N.T Wells, M. Halliwell, "Speckle in ultrasonic imaging", Ultrasonics 19, 1981, pp. 225–229.

[78]. Paul Suetens, Ultrasonic Imaging, "Fundamentals of medical imaging", Cambridge University Press 2002, pp.145-172

[79]. Pujari, R. M., and Hajare, V. D., "Analysis of ultrasound images for identification of Chronic Kidney Disease stages", Proc. IEEE First International Conference on Networks & Soft Computing ,2014, pp. 380-383.

[80]. Raja, K.B., Madheswaran, M., Thyagarajah, K., "Quantitative and qualitative evaluation of us kidney images for disorder classification using multi-scale differential features", ICGST-BIME Journal, vol. 7(1), May, 2000, pp. 1-8.

[81]. Ranjitha M., "Extraction and dimensionality reduction of features for renal calculi detection and artifact differentiation from segmented ultrasound kidney images", Proc. IEEE International Conference on Computing for Sustainable Global Development (INDIACom), 2016, pp. 3087- 3092.

[82] S. D. Chen, A. Ramli, "Contrast enhancement using recursive mean-separate histogram equalization for scalable brightness preservation," IEEE Trans. On Consumer Electronics, vol. 49(4), Nov.2003, pp. 1301-1309.

[83]. S. Manish, "Fuzzy-rough nearest neighbor algorithms in classification, Fuzzy Sets and Systems", vol.158, 2007, pp.2134 – 2152.

[84]. S. Poonguzhali, G. Ravindran, "Performance evaluation of feature extraction methods for classifying abnormalities in ultrasound liver images using neural network", Proceedings of the 28th IEEE EMBS Annual International Conference New York City, USA, Aug 30-Sept 3, 2006, pp. 4790-4794.

[85]. S. Poonguzhalil, B. Deepalakshmil and G. Ravindran, “Optimal feature selection and automatic classifi'cation of abnormal masses in ultrasound liver images”, IEEE - ICSCN 2007, MIT Campus, Anna University, Chennai, India. Feb. 22-24, 2007. pp. 503-506.

[86]. Sarah Bruyn Jones, Feb. 9, 2015, https://www.diagnosticimaging.com/authors/sarah-bruyn-jones, Accessed June 18, 2019

[87]. Sarah Bruyn Jones, “Top mobile apps for radiology”, PACS and Informatics, Practice Management, July 18, 2013, pp.6-10.

[88]. Shah J, Whitfield H. N., “Urolithiasis through the ages”, BJU International, vol. 89(8), 2002, pp. 801–810.

[89]. Shahabaz, D. K. Somwanshi, A. K. Yadav and R. Roy, "Medical images texture analysis: A review," International Conference on Computer, Communications and Electronics (Comptelix), Jaipur, 2007, pp. 436-440.

[90]. Shan Gaia, Boyu Zhangb, Cihui Yanga, Lei Yu, “Speckle noise reduction in medical ultrasound image using monogenic wavelet and Laplace mixture distribution”, Digital Signal Processing, vol. 72, 2018, pp. 192–207

[91]. Si Wang, Ting-Zhu Huang, Xi-Le Zhao, Jin-Jin Mei, Jie Huang, “Speckle noise removal in ultrasound images by first- and second-order total variation”, Numerical Algorithms, vol.78, 2018, pp. 513–533.

[92] Social Science Statistics, https://www.socscistatistics.com /tests/kruskal, Accessed 5 June, 2019

[93]. Sonka Milan, Hlavac Vaclav and Boyle Roger, “Image Processing, Analysis and Machine Vision”, Third Edition., Cengage Learning, 2013, pp. 630-635.

[94]. Sourabh Dash, Raghunathan Rengaswamy and Venkat Subramanian, “Fuzzy-logic based trend classification for fault diagnosis of chemical processes”, InternationalJournal of Computers and Chemical Engineering , vol. 27(3), 2003, pp.347-362.

[95]. Stamatelou K. K., Francis M.E., Jones C.A., Nyberg L.M. Jr, Curhan G.C.," Time trends in reported prevalence of kidney stones in the United States: 1976-1994", Kidney Int. 2003, pp.1817-1823.

[96]. Sussman M., Smereka P., Osher S., “A level set approach for computing solutions to in-compressible two-phase flow”, Journal, Comput. Phys., vol. 114(1), 1994, pp. 146–159.

[97]. T. Chan and L. Vese, “Active contours without edges”, IEEE Trans. Image Processing, vol.10(2), 2001, pp. 266–277.

[98]. T. Joel and R. Sivakumar, “Despeckling of ultrasound medical images: a survey”, Journal of Image and Graphics vol. 1(3), September 2013, pp. 161-165.

[99]. Ujjwal Maulik, "Medical image segmentation using genetic algorithms", IEEE Transactions on Information Technology in Biomedicine, vol. 13(2), March 2009, pp. 166-173.

[100]. V. Ulagamuthalvi and D. Sridharan, “Development of diagnostic classifier for ultrasound liver lesion images”, International Journal of Computer Applications, vol. 52, August 2012, pp. 12-15.

[101]. Vijay Jeyakumar and M. Kathirarasi Hasmi, “Quantitative analysis of segmentation methods on ultrasound kidney image”, International Journal of Advanced Research in Computer and Communication Engineering, vol. 2(5), May 2013, pp. 1974-1978.

[102]. Vijay Kotu and Bala Deshpande, “Model evaluation”, Data Science , Second Edition, Elsevier 2019, pp. 263-279.

[103] Vijayavani (kannada daily) (2019). Test your kidneys without fail. [online] p.3. Available at: http://epapervijayavani.in/index.php?dated=2019-03-15 Accessed 16 Mar. 2019

[104]. W. Ardiatna, A. H. Saputro and D. Soeharso Soejoko, "Analysis of kidney ultrasound images characterization using statistical moment descriptor", International Conference on Computer, Control, Informatics and its Applications (IC3INA), Tangerang, Indonesia, 2018, pp. 17-22.

[105]. Wan M. Hafizah, Eko Supriyanto, “Automatic generation of region of interest for kidney ultrasound images using texture analysis”, International Journal of Biology and Biomedical Engineering, vol. 6(1), 2012, pp. 1289-1305.

[106]. Wan M. Hafizah, Eko Supriyanto, “Feature extraction of kidney ultrasound images based on intensity histogram and gray level co-occurrence matrix”, IEEE Sixth Asia Modelling Symposium, 2012, pp. 115-120.

[107]. Wołyniec W., Jankowska M. M., Król E., et al., "Current diagnostic evaluation of autosomal dominant polycystic kidney disease", Polskie Archiwum Medycyny Wewnetrznej, vol. 118(12), 2008, pp. 767–773.

[108]. Xie, J., Jiang, Y., Tsui, H., "Segmentation of kidney from ultrasound images based on texture and shape prioris", IEEE Trans. on Medical Imaging, vol. 24(1), 2005, pp. 45-57.

[109]. Xiong X, Guo Y, Wang Y, et al. , "Kidney tumor segmentation in ultrasound images using adaptive sub-regional evolution level set models", The Journal of Biomedical Engineering, vol. 36 (6), 2019, pp. 945-956.

[110]. Yingyue Zhou, Hongbin Zang, Su Xu et al., "An iterative speckle filtering algorithm for ultrasound images based on bayesian nonlocal means filter model", Biomedical Signal Processing and Control vol. 48, 2019, pp. 104–117.

[111]. Zadeh L. A.,"Fuzzy sets", Information and Control, 1965, vol. 8, pp. 333-335.

[112]. Zadeh L.A., "Making computers think like people", IEEE. Spectrum 1984, pp. 26-32.

[113]. Zadeh L.A., "Outline of a new approach to the analysis of complex systems and decision processes", IEEE Transactions on Systems, Man, and Cybernetics, vol. 3(1), 1973, pp. 28-44.